https://doi.org/10.15388/vu.thesis.747
https://orcid.org/0000-0001-7730-9573

VILNIUS UNIVERSITY
CENTER FOR PHYSICAL SCIENCES AND TECHNOLOGY

Klemensas Laurinavičius

Vector Optical Bullets in Free Space and Dispersive Medium

DOCTORAL DISSERTATION

Natural Sciences,
Physics (N 002)

Vilnius 2025

This dissertation was written between 2020 and 2024 at State research institute Center for Physical Sciences and Technology.

Academic supervisor:
Dr. Sergejus Orlovas (State research institute Center for Physical Sciences and Technology, Physics – N 002).

Dissertation Defense Panel:

Chairman – Prof. Habil. Dr. Audrius Dubietis (Vilnius University, Natural Sciences, Physics – N 002).

Members:
Dr. Mindaugas Gedvilas (State research institute Center for Physical Sciences and Technology, Materials Engineering – T 008),
Dr. Kęstutis Regelskis (State research institute Center for Physical Sciences and Technology, Physics – N 002),
Prof. Habil. Dr. Kęstutis Staliūnas (Universitat Polit‘ecnica de Catalunya (UPC), Natural Sciences, Physics – N 002),
Assoc. Prof. Dr. Viktorija Tamulienė (Vilnius University, Natural Sciences, Physics – N 002).

The dissertation shall be defended at a public meeting of the Dissertation Defense Panel at 13:00 on 17 April 2025 in Room D401 of the Center for Physical Sciences and Technology.
Address: Saulėtekio av. 3, NFTMC, Room D401, Vilnius, Lithuania.
Tel. +370 645 15550; email: office@ftmc.lt.

The text of this dissertation can be accessed at the Vilnius University Library, as well as on the website of Vilnius University: www.vu.lt/naujienos/ivykiu-kalendorius.

https://doi.org/10.15388/vu.thesis.747
https://orcid.org/0000-0001-7730-9573

VILNIAUS UNIVERSITETAS
FIZINIŲ IR TECHNOLOGIJOS MOKSLŲ CENTRAS

Klemensas Laurinavičius

Vektorinės optinės kulkos laisvoje erdvėje ir dispersinėje terpėje

DAKTARO DISERTACIJA

Gamtos mokslai,
Fizika (N 002)

Vilnius 2025

Disertacija rengta 2020–2024 metais Valstybiniame mokslinių tyrimų institute Fizinių ir technologijos mokslų centre.

Mokslinis vadovas:
dr. Sergejus Orlovas (Fizinių ir technologijos mokslų centras; gamtos mokslai, fizika – N 002).

Gynimo taryba:

Pirmininkas – prof. habil. dr. Audrius Dubietis (Vilniaus universitetas; gamtos mokslai, fizika – N 002).

Nariai:
dr. Mindaugas Gedvilas (Fizinių ir technologijos mokslų centras; technologijos mokslai, medžiagų inžinerija – T 008),
dr. Kęstutis Regelskis (Fizinių ir technologijos mokslų centras; gamtos mokslai, fizika – N 002),
prof. habil. dr. Kęstutis Staliūnas (Katalonijos politechnikos universitetas; gamtos mokslai, fizika – N 002),
doc. dr. Viktorija Tamulienė (Vilniaus universitetas; gamtos mokslai, fizika – N 002).

Disertacija ginama viešame Gynimo tarybos posėdyje 2025 m. balandžio mėn. 17 d. 13:00 val. Nacionalinio fizinių ir technologijos mokslų centro D401 auditorijoje. Adresas: Saulėtekio al. 3, NFTMC, D401 aud., Vilnius, Lietuva.
Tel. +370 645 15550; el. paštas: office@ftmc.lt.

Disertaciją galima peržiūrėti Vilniaus universiteto bibliotekoje ir VU interneto svetainėje adresu: www.vu.lt/naujienos/ivykiu-kalendorius.

ACKNOWLEDGEMENTS

First of all, I want to thank my supervisor Sergej Orlov for optimism and ability to refresh my motivation to pursue my career in science.

I would also like to express my gratitude to my colleague and dear friend, Justas Berškys, for his invaluable advice and support along the way.

I am also grateful to my other colleagues, especially Vytautas Jukna, for their constructive criticism, insightful discussions, and willingness to challenge my ideas. Their feedback and collaboration have been instrumental in refining this work and pushing me to think more critically.

To my friends, your support, camaraderie, sleepless nights, and moments of laughter have been invaluable throughout this journey.

To my family, thank you for your encouragement and belief in me.

A special thanks to my dancing community, whose energy, joy, and passion kept me grounded and offered the perfect escape.

Finally, I acknowledge the broader scientific community whose dedication has guided and inspired my work.

CONTENTS

LIST OF ABBREVIATIONS

FWM	Focus Wave Modes
TE	Transverse Electric
TM	Transverse Magnetic
FWHM	Full Width Half Maximum
GVD	Group Velocity Dispersion
LG	Laguerre-Gaussian
SPP	Spiral Phase Plate

INTRODUCTION

Aim of the thesis

Theoretical studies in electromagnetics for generation of nondiffracting and nondispersive light pulses, which are crucial for various applications, are on the rise nowadays. Current technologies allow for the creation of short-duration, high-power pulses. To achieve better beam shaping control of non-diffracting and non-dispersive pulses, highly focused vector pulses are investigated. For this investigation different simulation methods were used for analyzing vector pulsed light beams with different polarization structures (linear, azimuthal, and radial) and comparing them to scalar models. The effects of superluminal, subluminal, and negative group velocities on vector focus wave modes in both vacuum and dielectric materials were analyzed. Additionally, the properties of optical vorticity and radial/azimuthal polarization are explored, with their impact on the Bessel-X pulse duration considered. The study focuses on highly nonparaxial vector Bessel-X pulses [1], presenting analytical expressions and uncovering novel properties arising from inhomogeneous polarization. The investigation then moves on to another type of optical bullets – vector focus wave modes [2], which are generalizations of the X-waves and Bessel-X pulses inside a dielectric dispersive medium. For this purpose, one of the glass materials was selected and the dispersion relation of the spatiotemporal spectra was analyzed [3]. The general expression of the spatiotemporal spectra describes the cone angles of forward propagating Bessel beams that result in the pulsed signal propagating in the Bessel zone with controllable velocity V, which can be superluminal [4,5], subluminal [6], or even negative (i.e. propagate backward) [7]. These conditions may require high cone angles of superposed Bessel beams, so a valid vector description is required. In this work, the vector description is introduced for optical bullets, and the electromagnetic structure of the resulting pulsed fields in a glass is studied, relating the duration to the transverse size of the beam, central frequency, and propagation velocity of the optical bullet, to investigate the generation and behavior of vector optical bullets within a dielectric medium. For experimental application of nondiffracting and nondispersive light pulses a proper mathematical description of highly focused vector pulses is required. Using mathematical model presented in this work, it is possible to investigate the properties of the beam in dielectric media with group velocities that can be superluminal, subluminal, or even negative. The results allow us to understand the relations between transverse size of the beam, the intensities of each component (paying special attention to the z component of the electric field) depending on the central frequency, polarizations, different group velocity V and integration constant γ values.

Tasks of this work

The main task of this work, is to investigate vector optical bullets (nondiffracting and nondispersing pulsed beams) in vacuum and in dielectric materials and their behaviour with different topologies defined in this work:

- Investigate Bessel-X beam spatial structure, its vectorial properties for different cone angles and topological charges.
- Investigate Bessel-X beam temporal duration, its vectorial properties for different cone angles and topological charges.
- Investigate vector focus wave modes with superluminal, subluminal and negative group velocities and their properties.
- Investigate subcycle vector focus wave modes in vacuum and dispersive medium.

Novelty and relevance

- In this work we present analytical model of pulsed, invariant to propagation, fields with both optical vorticity and radial/azimuthal polarization.
- The temporal FWHM durations have been investigated for vector Bessel-X pulses, for linear, azimuthal and radial polarizations.
- It was shown that in BK7 glass it is possible to simulate both X and O shaped beams using focus wave modes within the optical range.

- We have simulated superluminal, subluminal and negative group velocity focus wave modes in BK7 glass.

- We have simulated subcycle pulses in free space and in BK7 glass using focus wave modes.

Statements to be defended

- The vectorial structure of linearly, radially, and azimuthally polarized Bessel-X pulses significantly influences their duration, particularly in the non-paraxial regime when the cone angle is more than 45 degrees. The dependence of pulse duration on the angle shows non-trivial variation and is different for linear, radial, and azimuthal polarizations.

- For a fixed Bessel-X cone angle θ, the Bessel-X pulse duration depends non linearly on temporal spectral width when it reaches durations below tens of femtosecond, deviating from the usual linear trend observed in beams without angular dispersion. This behavior holds for the analyzed linear, radial, and azimuthal polarization Bessel-X pulses, as well as for their different topological charges.

- The chromatic dispersion of BK7 glass enables the calculation of angular dispersion curves necessary for generating superluminal, subluminal, and even negative group velocity Bessel-X beams.

- When group velocity $V/c = 0.63685$ and propagation constant $\gamma = -0.628\ \mu\text{m}^{-1}$, the angular dispersion curve of BK7, representing angle vs frequency, exhibits both positive and negative slopes. The negative slope generates an O-shaped intensity distribution of Bessel-X beams, while the positive slope leads to an X-shaped spatiotemporal Bessel-X intensity distribution.

- Subcycle Bessel-X pulses can be generated in free space and BK7 glass. The shortest subcycle Bessel-X pulse in vacuum corresponds to 0.56 of its central frequency cycle, while in BK7 glass, it is 0.67 of its central frequency cycle.

Contribution of the author

The author performed all simulations, processed and analyzed the obtained data. The author also contributed to preparation and participated in discussions of all manuscripts.

[A1] Author wrote code for the software to perform all the required Bessel-X numerical simulations, analysed and described the results and prepared illustrations.

[A2] Author wrote code for the software to perform all the required optical bullet numerical simulations, analysed and described the results and prepared illustrations.

[A3] Author wrote code for the software to perform all the required subcycle pulse numerical simulations, analysed and described the results and prepared illustrations.

[A4] Author wrote code for the software to perform the required numerical simulations, analysed the results and prepared some of the illustrations. The experimental part was done with help of colleagues.

LIST OF PUBLICATIONS

On the dissertation topic

[A1] **Klemensas Laurinavičius**, Sergej Orlov, and Ada Gajauskaitė. "Azimuthally and Radially polarized pulsed Bessel-X vortices." Optik 270 (2022): 169998.

[A2] **Klemensas Laurinavičius**, Sergej Orlov, and Ada Gajauskaitė. "Vector Optical Bullets in Dielectric Media: Polarization Structures and Group-Velocity Effects." Applied Sciences 14.10 (2024): 3984.

[A3] **Klemensas Laurinavičius**, Sergej Orlov. "Localized Vector Optical Nondiffracting Subcycle Pulses." Applied Sciences 14.24 (2024): 11538.

Other publications

[A4] Vosylius, Ž., Novičkovas, A., **Laurinavičius, K.**, Tamošiūnas, V. (2022). Rational design of scalable solar simulators with arrays of light-emitting diodes and double reflectors. IEEE journal of photovoltaics, 12(2), 512-520.

Conference proceedings

[B1] **Klemensas Laurinavičius**, Justas Berškys, Sergej Orlov. Tailoring response of a cluster of nanoparticles on a substrate and its application for design of geometrical phase elements. SPIE OPTO, 2020, San Francisco, California, United States.

[B2] Sergej Orlov, Justas Berškys, **Klemensas Laurinavičius**. Closed-form analytical Mie theory of vector complex source vortices. SPIE OPTO, 2020, San Francisco, California, United States.

[B3] **Klemensas Laurinavičius**, Sergej Orlov, and Gytis Braždžiūnas. Investigation of Electron Acceleration using Chirped Radially Polarized Pulsed Bessel-X Beams. The European Conference on Lasers and Electro-Optics(CLEO) 2021, Munich, Germany.

[C1] **Klemensas Laurinavičius**, Sergej Orlov, Gytis Braždžiūnas. „Investigation of Electron Acceleration using Chirped Radially Polarized Pulsed Bessel-X Beams“. CLEO/Europe-EQEC 2021, June 21-25, 2021.

[C2] **Klemensas Laurinavičius**, Justas Berškys, Sergej Orlov. „Investigation of sub-wavelength meta-atoms for development of multi-layered photonic elements“. E-MRS 2021, May 31-June 4, 2021.

[C3] **Klemensas Laurinavičius**, Sergejus Orlovas, Pavel Gotovski. „Electron Acceleration using Chirped Radially Polarized Superluminar Bessel-X Beams“ CERN CBC 2021, Jun 28 – 30, 2021, University of Tartu.

[C4] Sergejus Orlovas, **Klemensas Laurinavičius**, Justas Berškys. „Elektronų greitinimas čirpuotais radialinės poliarizacijos impulsiniais šviesos pluoštais“. LNFK44 2021

[C5] **Klemensas Laurinavičius**, Sergejus Orlovas. „Azimutinės ir radialinės poliarizacijos Bessel-X vektoriniai sūkuriniai impulsai”. Conference of PhD Students and Young Researchers FizTech2022, 2022 October 19-20, Vilnius, Lithuania.

[C6] **Klemensas Laurinavičius**, Sergej Orlov. „Influence of the chirp in the direct-field Electron Acceleration in a Radially Polarized Pulsed beam“. E-MRS 2022, May 30-June 3, 2022.

[C7] Karolis Mundrys, Sergejus Orlovas, **Klemensas Laurinavičius**. „Optinių Airy pluoštų erdvinio valdymo metodai pasitelkus fazinius elementus”. Conference of PhD Students and Young Researchers FizTech2021, 2021 October 20-21, Vilnius, Lithuania.

[C8] **Klemensas Laurinavičius**, Sergejus Orlovas. „Vektorinių sufokusuotų židinio modų sklidimo dielektrinėje terpėje tyrimas”. Conference of PhD Students and Young Researchers FizTech2023, 2023 October 18-19, Vilnius, Lithuania.

[C9] **Klemensas Laurinavičius**, Sergej Orlov. „Azimutinės ir radialinės poliarizacijos vektorinių Beselio X impulsų tyrimas“. LNFK45, October 25-27, 2023, Vilnius, Lithuania.

[C10] **Klemensas Laurinavičius**, Sergej Orlov. „Sub-cycle nondiffracting and nondispersing vector optical pulsed bullets: polarization structures and group velocity effects“. SPIE Photonics West, 25 - 30 January 2025, San Francisco, California, United States.

1. LITERATURE OVERVIEW

Engineering of structured light is on the rise nowadays due to the wide range of possible applications and benefits not only within optics, but also within physics in general [8]. This interest is caused by a large degree of controllable phenomena such as optical traction [9, 10], optical spinning [11], self-healing [12], imaging [13] and nondiffractive nondispersive propagation [14].

The diffraction of light beams is one of the obstacles for applications, such as laser communication, information transfer, and long-distance laser interactions. As the beam propagates, its spatial components experience dephasing due to diffraction, resulting in spatial profile distortion: the size of the beam increases and the intensity drops [15–17]. The nondiffracting beam is a beam that circumvents diffraction spreading through constructive interference in a zone called the Bessel zone, in the case of the most well-known example – the Bessel beam [18, 19]. However, other beams are also known- the elliptical Mathieu [20], the parabolic Weber [21], or the Airy beam [22], see Figure 1.1. These examples ideally propagate infinitely large distances and possess infinite energy, however, giving them a Gaussian envelope results in finite energy optical beams resisting diffractive spreading over finite distances [23].

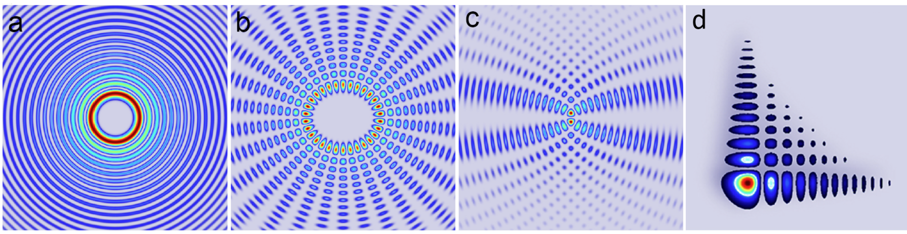

Figure 1.1: Typical examples of nondiffracting beams: transverse field distributions of selected (a) Bessel, (b) Mathieu, (c) Weber, (d) Airy beams. Adapted from [24].

Moving to pulsed beams [25], yet another obstacle appears for long-distance laser applications. Due to the dispersion of the material, the phase velocities of different temporal components with different wavelengths are not the same [15]. For this reason, they propagate differently [26], so the pulse experiences dispersive broadening and other shape distortions [27]. This was found to be overcome using the non-monochromatic superposition of nondiffracting beams with a predefined spatiotemporal dispersion within the pulse [3, 28]. Joint dispersion and diffraction resistance of such pulsed fields has allowed to call them optical bullets. Among such examples of pulsed nondiffracting and nondispersing beams are pulsed Bessel beams [29], focus wave modes(FWM) [30], and X-waves [7, 31, 32] and spatio temporal light sheets [33, 34], which can be extended to the elliptical and parabolical X-waves [35] and to the nonlinear optics [36, 37].

Yet another degree of freedom, which becomes more noticeable within the field of structured light, is the polarization of the electromagnetic field. This advance is constantly increasing since the realization that inhomogeneous polarization allows for a sharper focus of light [38, 39], which can be conveniently understood using a multipolar description of light [40, 41], also valid for pulsed fields [42]. As the numerical aperture increases, the scalar description of the optical field becomes invalid [43–46]. Even for linearly polarized light, a noticeable longitudinal component appears and even detectable cross-polarization is observed [47]. The longitudinal component is especially noticeable in radially polarized light [48], which is created using polarization controllable optical elements [49, 50]. Anisotropic crystals have another interesting characteristic - birefringence. Birefringent materials have different refractive indices for different polarization directions. For even more control over birefringence, we could use liquid crystals which can be controlled with external fields. By controlling polarization and amplitude spatially, it is possible to enhance optical encryption, and fine-tune vectorial holography [51]. Birefringence adds to the complexity of the problem, especially since anisotropic medium leads to polarization mixing between TE and TM polarizations [52] due to Imbert-Fedorov shift [53, 54].

The concept of an inhomogeneously polarized nondiffracting beam was successfully introduced by Bouchal [55], although some insight into the topic was already present in the book by Stratton [56] and the method of construction of such polarized structures is discussed in great detail by Morse [57]. The extension of the concept of nondiffracting X-waves from the scalar domain to the vector domain was introduced [58] and extended to vortical properties with an arbitrary frequency spectrum [59]. Vector light sheets of nondiffracting light were also recently studied [60, 61]. Moreover, vector parabolical, elliptical optical bullets were considered [62,63]. These advances are especially interesting, given the applications of pulsed beams polarized radially and azimuthally for material processing [64,65], together with the applications of nondiffracting beams [66, 67].

In this work highly nonparaxial vector Bessel-X pulses [1] are investigated, introducing analytical expressions and revealing novel properties introduced by inhomogeneous polarization. We also move on to the investigation of another type of optical bullets - vector focus wave modes, which are generalizations of the X-waves and Bessel-X pulses inside a dielectric dispersive medium. For this purpose, we select one of the glass materials and analyze the dispersion relation of the spatiotemporal spectra [3]. The general expression of the spatiotemporal spectra describes the cone angles of forward propagating Bessel beams that result in the pulsed signal propagating in the Bessel zone with controllable velocity V, which can be superluminal [4,5], subluminal [6], or even negative (i.e. propagate backward) [7]. These conditions may require high cone angles of superposed Bessel beams, so a valid vector description is required. We introduce to the optical bullets this vector description and study electromagnetic structure of resulting pulsed fields in a dielectric material, relating the duration to the transverse size of the beam, central frequency and propagation velocity of the optical bullet, for the purpose of investigating the generation and behavior of vector optical bullets within dielectric medium. For experimental application of nondiffracting and nondispersive light pulses we need a proper mathematical description of highly focused vector pulses. By using our mathematical model we are able to investigate the properties of the beam in a dielectric media, with group velocities that can be superluminal, subluminal, or even negative. The results allow us to understand the relations between transverse size of the beam, the intensities of each component (paying special attention to the z component of the electric field) depending on the central frequency, polarizations, different group velocity V and integration constant γ values.

Illustration on one of the generation methods for Bessel beams is depicted in Figure 1.2, where we use an optical element called axicon, which has a conical surface. Due to the superposition of the incident

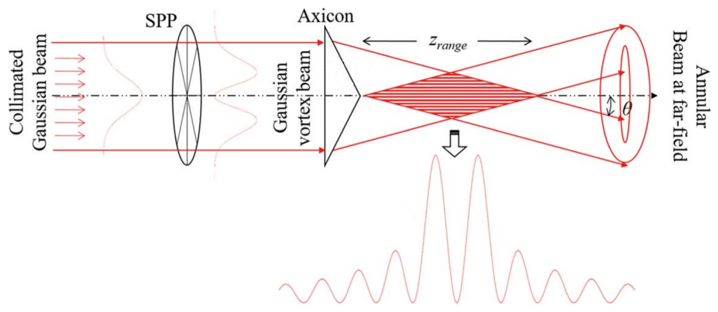

Figure 1.2: Ray diagram of arbitrary Bessel beam generation in the presence of axicon and spiral phase plate. Adapted from [68].

beam in the Bessel zone marked as z_{range}, we get a Bessel beam. Furthermore, with the addition of another diffractive optical element we can produce higher order Bessel beams. For example, the incident beam can be passed through a parallel aligned spiral phase plate (SPP) and axicon to produce higher order Bessel beams. The spiral phase plate represents the topological charge m.

The scalar wave equation in vacuum in the Cartesian (Descartes) coordinate system [69] is written as follows:

$$\left(\frac{\partial^2}{\partial x^2}+\frac{\partial^2}{\partial y^2}+\frac{\partial^2}{\partial z^2}-\frac{1}{c^2}\frac{\partial^2}{\partial t^2}\right)E(\mathbf{r},t)=0, \tag{1.1}$$

where $\mathbf{r}=\{x,y,z\}$ is the radius vector, t is time, c is the speed of light in vacuum. The simplest solution to this differential equation is a plane monochromatic wave of frequency ω:

$$E(\mathbf{r},t)=E_0\exp\left[i\left(\mathbf{k}\cdot\mathbf{r}-\omega t\right)\right], \tag{1.2}$$

which is propagating in the direction of the wave vector $|\mathbf{k}|=\omega/c$, E_0 is the wave amplitude. Different boundary conditions lead to different solutions of the wave equation written in the Cartesian system, which can be expressed as the superposition of plane waves with specific wave vector $\mathbf{k}$ and frequency ω. This wave does not change in space and time, hence it can be called a non-diffracting wave. The energy of such a beam is infinite, therefore these solutions are not physical, and would only be possible in a limited space.

Spherical non-diffracting wave solutions can be obtained similarly by writing the scalar wave equation in the spherical coordinate system $\mathbf{r} = \{r, \theta, \phi\}$

$$\left[\frac{1}{r^2}\frac{\partial}{\partial r}\left(r^2\frac{\partial}{\partial r}\right) + \frac{1}{r^2\sin\theta}\frac{\partial}{\partial\theta}\left(\sin\theta\frac{\partial}{\partial\theta}\right) + \frac{1}{r^2\sin^2\theta}\frac{\partial^2}{\partial\phi^2} - \frac{1}{c^2}\frac{\partial^2}{\partial t^2}\right] \times E(r, \theta, \phi, t) = 0. \tag{1.3}$$

Unlike the plane wave – the spherical wave's amplitude decreases with distance from the source, but the energy in each layer of thickness dr remains constant, thus this wave would also require infinite energy and describes not a physical situation. Far enough from the source, a spherical wave can be approximated as a plane wave.

Writing the wave equation in cylindrical coordinates

$$\left(\frac{\partial^2}{\partial r^2} + \frac{1}{r}\frac{\partial}{\partial r} + \frac{1}{r^2}\frac{\partial^2}{\partial\phi^2} + \frac{\partial^2}{\partial z^2} - \frac{1}{c^2}\frac{\partial^2}{\partial t^2}\right) E(r, \phi, z, t) = 0, \tag{1.4}$$

we get another solution of the wave equation – a cylindrical wave

$$E(r, \phi, z, t) = E_0 H_m^{(1,2)}(k_r r) \exp\left[i\left(k_z z - \omega t\right)\right], \tag{1.5}$$

where $H_m^{(1,2)}(k_r r)$ are the first and second kind m-th order Hankel functions. For large r values, the plane wave front has the asymptotic form $\exp(\pm i k_r r)$, while near the axis it is described as $\sim 1/r^m$, where $(m > 0)$ and $\approx \ln(r)$, when $(m = 0)$. Cylindrical Hankel functions can be expressed through Bessel or Neumann functions $H_m^{(1,2)} = J_m \pm i N_m$, which are also known as cylindrical cosine and sine functions. The Neumann function takes infinite values at the axis and is used to describe infinite power light absorbing or emitting cylindrical filaments. The Bessel function is used to describe situations where there is no emission absorption at the axis. When $k_z = 0$, such a wave source is an infinite filament or cylinder, and its wave front replicates the source's symmetry or one of its coordinate surfaces. When $k_z \neq 0$, the wave front or cone corresponds to the radiation of an infinitely long cylindrical source. The standing wave in the transverse plane is described by the Bessel function $J_m(k_r r)$. When such a wave has the z axis propagating term $\exp(ik_z z)$, we obtain the classical non-diffracting Bessel beam [18, 70]. The cylindrical nature of the Bessel beam emphasizes its ability to bypass obstacles—this is possible when the obstacle's transverse dimensions are smaller than the dimensions of the cylindrical source [71, 72].

Besides the mentioned coordinate systems, it is possible to create non-diffracting beams in cylindrical coordinates—by adding the z coordinate to two dimensional coordinates, or in spherical -by rotating the two-dimensional solutions about one of the axes. For data transfer it is more convenient to use cylindrical coordinates, where the information is traveling along the z axis. Optical solutions like the elliptic or parabolic cylinder coordinate systems also exist as non-diffracting solutions [20, 73].

1.1.1. Vortices in Non-diffracting beams

A. Ashkin observed during his experiment that an unfocused light beam attracts particles with a high refractive index towards the axis of the beam and pushes them in the direction of the beam's propagation. When the beam propagates from below, the axial pushing force can compensate for the gravitational force, and this resulting phenomenon is called optical levitation [74]. By using two intersecting beams or a single strongly focused beam [75], it is possible to capture small dielectric particles in three coordinates. This technique enabled the lifting or transferring of objects with visible light radiation, and thus it was named optical tweezers. This tool is associated with numerous applications in science, atomic physics, quantum optics, and microbiology. It has been observed that higher-order laser modes – optical vortices – capture specific objects better: reflective [76], absorbing [77], and those with low refractive indices [78, 79].

Optical vortices are helical dislocations of the light field, where the wavefront shape is a helical (helicoidal) surface. The main characteristic of such fields is points of undefined phase, first described by Nye and Berry [80]. At these points of the optical field, the wave amplitude is close to zero, resulting in dark spots in the wave intensity distribution. A vortex can be mathematically imagined as a zero of the complex amplitude of the optical field E. The phase $e^{im\varphi}$ and amplitude r^m of the field around the complex zero depend on the order m of the zero, which is also referred to as the topological charge of the light vortex.

According to the phase $e^{im\varphi}$, vortices in the vicinity of the vortex center changing in a right-handed or left-handed manner are divided into positive and negative ones. The number m indicates how many times the phase changes its value over 2π [81].

The optical vortex of linear polarization has angular momentum. The angular momentum $\mathbf{M}$ of the transverse electromagnetic wave is

$$\mathbf{M} = \epsilon \mathbf{r} \times (\mathbf{E} \times \mathbf{B}), \tag{1.6}$$

where $\mathbf{E}$ is the electric field strength, $\mathbf{B}$ is the magnetic field induction vector. The total angular momentum is calculated by the formula:

$$\mathbf{J} = \epsilon \int \mathbf{r} \times (\mathbf{E} \times \mathbf{B})\, d\mathbf{r}. \tag{1.7}$$

From the linear polarization of the Bessel beam's electromagnetic field, we can easily find the radial and azimuthal polarization components of the Bessel beam's angular momentum. As the analysis shows, the angular momentum vector of these polarizations has only the azimuthal component, which, when integrated over the entire space, due to azimuthal symmetry, we obtain that the total angular momentum is zero. For linearly polarized and circularly polarized [82] Bessel beams with non-zero angular momentum, all three components of the angular momentum vector are non-zero, and by averaging over the entire space, the impact is only on the z-component

$$M_z \propto \left[m J_m^2 - \frac{1}{2} \sigma r \frac{d}{dr} J_m^2 \right], \tag{1.8}$$

where $\sigma = \pm 1$ for circular left-handed or right-handed polarization and $\sigma = 0$ for linear polarization. After averaging the angular momentum over the entire space, we find that the angular momentum and energy ratio for the Bessel beam is

$$\frac{J}{cP} = \frac{m + \sigma}{\omega}, \tag{1.9}$$

thus, the angular momentum of the Bessel beam is proportional to the integer or topological charge m. FWM waves are also characterized by angular momentum, which is proportional to the topological charge m

of the Bessel beam they consist of [83].

Light beams carrying optical vortices (vortex beams) are distinguished by their properties. Adding even a vanishingly small coherence background to a vortex beam of higher than unit topological charge, a vortex hole of charge $|m|$ forms at the single topological charge vortex [84]. The result of the superposition of light vortices differs from classical interference results. In the case of the common Laguerre-Gaussian (LG) vortex superposition, vortices arise in the complicated beam whose count changes during propagation depending on the beam's dimensions and amplitude [85]. The combined LG vortex beam exhibits a more complex topological structure than would be expected from the elementary arithmetic of individual beam charges [86, 87]. Complex topological structures can exist in light fields - vortex trajectories with annihilation points form nodes, manifesting other high-topology structures [88–91]. Femtosecond pulse vortex propagation is conditioned by filamentation in air [92]. In birefringent crystals, even under weak polarization anisotropy, interesting topological structures are formed [93, 94]. The vortex Mathieu beams also exhibit properties analogous to the Bessel beam vortex [95].

Complex topologically structured vortex fields are important in interferometry [96], micromanipulation, such as optical particle tweezers [97], microengine propulsion forces [98], microflow generators, asymmetric particle manipulators [99], Bose-Einstein condensate manipulators [100] due to their non-diffracting nature, can transport objects over long distances compared to LG vortices [101, 102].

The field of nonlinear optics of light vortices is also developing fairly rapidly, as light vortices propagating in a nonlinear medium lead to the emergence of new phenomena. During second harmonic generation, it was shown that the topological charge of the light vortex doubles [103, 104]. Also during three-wave mixing, the phenomenon of topological charge addition and subtraction occurs [105]. Three-wave mixing, in cases of beam carrying, leads to the appearance of various light vortex interaction effects [106–108]. Intense light beams carrying vortices split into a set of solitons due to self-interaction [107], vortex collapse occurs [109]. Beam diffraction and beam carrying effects lead to the spontaneous appearance of multiple optical vortex pairs [110]. The interference pattern of vortex waves and the superposition of vortex wavefronts create magnetic structures [111]. The superposition of Bessel vortices during harmonic generation has been explored [112,113]. It has been shown that in the second harmonic beam, an additional vortex of topological charge emerges and strengthens in the vortex field during the generation of the second harmonic [114]. Quantum noise parameter amplification in the vortex field has also been explored [115]. The appearance of the Bessel vortex due to quantum noise amplified in the parametric generation of the Gaussian beam has been demonstrated [116]. Spatial solitons have also been demonstrated [117]. Transverse patterns in nonlinear optical resonators have been investigated [118].

1.2. Scalar Bessel-X waves

The scalar Bessel-X wave is a pulsed scalar non-diffracting electromagnetic field which is composed of monochromatic Bessel beams of different frequencies ω with individual amplitudes defined by the spectral function $S(\omega)$ and by the temporal-spatial dispersion law $k_\rho = k(\omega)\sin\theta(\omega)$, where k_ρ is the transverse wavevector component. In general, spatial dispersion is defined by phase matching of longitudinal components of the wave vector, so that each spatial component propagates at the phase velocity matched with other components. In one specific case, the cone angle and individual Bessel angle phase velocity on the propagation axis has a clear dependence $k_z = k\cos\theta$ [3]. Thus, with this knowledge, it is possible to construct wavepackets that mitigate or even cancel the material dispersion and consequently eliminate the pulse shape change. In this case, the resulting scalar electromagnetic field is given by

$$E(\rho,\varphi,z,t) = \int_0^\infty S(\omega) J_m\left(k_\rho \rho\right) \mathrm{e}^{\mathrm{i}m\varphi} \mathrm{e}^{\mathrm{i}(k_z z-\omega t)} d\omega, \tag{1.10}$$

where J_m is the Bessel function of m-th order, m is the topological charge, $k_z = k\cos\theta$, where $\theta(\omega)$ is a single frequency cone angle, and $\mathbf{r} = (\rho,\varphi,z)$ is the spatial and t is time coordinates, respectively. In the specific case of Bessel-X waves [29,119], the spectral amplitude $S(\omega)$ (see Figure 1.3) is given by

$$S(\omega) = \frac{\alpha}{\sqrt{2\pi}}\sqrt{\frac{\omega}{\omega_0}} \exp\left[-\frac{\alpha^2\left(\omega-\omega_0\right)^2}{2}\right], \tag{1.11}$$

where ω_0 is the carrier frequency, α is inversely proportional to the

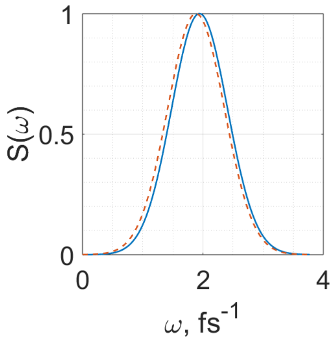

Figure 1.3: The spectral distribution of Equation (1.11) (blue) $S(\omega)$ compared to a Gaussian spectral distribution (red dashed).

spectral bandwidth of the signal. In our case, analysis of the beam propagation is done in a vacuum, the angular dispersion is adjusted so that the cone angle θ is constant and the group velocity is $c/\cos\theta$.

In this case equation (1.10), can be approximated as [29, 119]

$$\begin{aligned} E(\mathbf{r},t) = \sqrt{Z(d)}\exp\left[-\frac{\rho^2\sin^2\theta + d^2}{2c^2\alpha^2} + \mathrm{i}\,(m\varphi + \omega_0 d)\right] \\ \times J_m\left[\frac{Z(d)\rho\omega_0\sin\theta}{c}\right], \end{aligned} \tag{1.12}$$

where $Z(d) = 1 + \mathrm{i}d/(\omega_0\alpha^2)$ and $d = (z/c)\cos\theta - t$, c is the speed of light and θ is the cone angle of the Bessel-X wave.

By using the scalar wave equation (1.12) we can demonstrate the scalar Bessel beams with different topological charges, see Figure 1.4.

1.3. Vector Bessel-X waves

Vectorial solutions of the Maxwells equations can be constructed from solutions of scalar wave equations using the technique described in Reference [56, 57]:

$$\mathbf{M}(\mathbf{r},t) = \nabla\times\mathbf{a}E(\mathbf{r},t), \quad \mathbf{N}(\mathbf{r},t) = \frac{1}{k}\nabla\times\mathbf{M}(\mathbf{r},t), \tag{1.13}$$

where $\mathbf{M}(\mathbf{r},t)$, $\mathbf{N}(\mathbf{r},t)$ are transverse electric (TE) and transverse magnetic (TM) vector field modes, ∇ is a nabla operator and $\mathbf{a}$ is a predefined

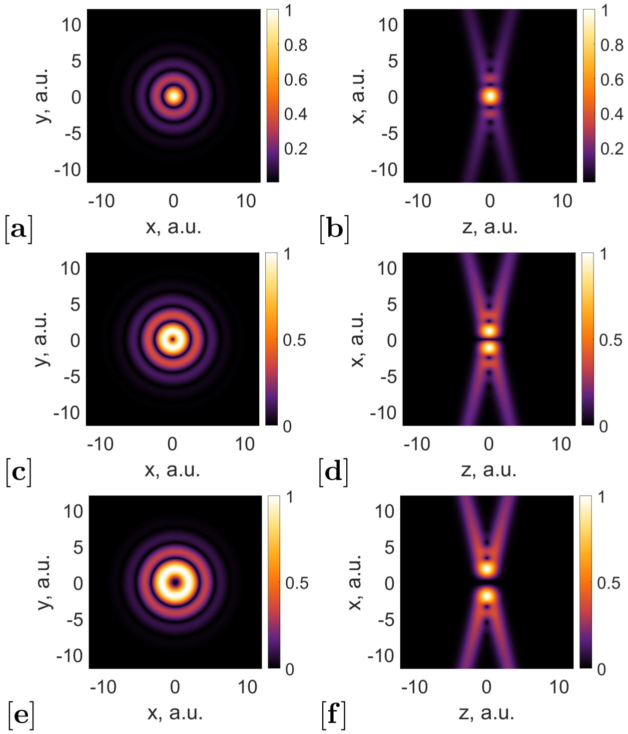

Figure 1.4: Intensity distributions of scalar Bessel beam, when $m = 0$ (a, b), $m = 1$ (c, d), $m = 2$ (e, f).

vector [57]. Applying this operation to Equation (1.10) leads to

$$\mathbf{M}(\mathbf{r}, t) = \int_0^\infty S(\omega)\mathbf{M}_0(\mathbf{r}; \omega)\mathrm{e}^{-\mathrm{i}\omega t} d\omega,$$
$$\mathbf{N}(\mathbf{r}, t) = \int_0^\infty S(\omega)\mathbf{N}_0(\mathbf{r}; \omega)\mathrm{e}^{-\mathrm{i}\omega t} d\omega, \tag{1.14}$$

where $\mathbf{M}_0$ and $\mathbf{N}_0$ are vectorial Bessel functions, their expressions can be found in the literature [55] or obtained directly from Equation (1.13).

Some properties of vectorial solutions $\mathbf{M}(\mathbf{r}, t)$, $\mathbf{N}(\mathbf{r}, t)$ can be deduced from situations similar to those previously discussed in the literature [120]. Electric and magnetic field components that are solutions to Maxwell's equations are expressable in terms of 2 independent functions $g_1(\mathbf{r})$ (x polarized) and $g_2(\mathbf{r})$ (y polarized) of the paraxial wave equation.

In this case, the individual electric field components are

$$
\begin{aligned}
E_x &= g_1(\mathbf{r}) + \frac{1}{4k^2}\left[\frac{\partial^2 g_1(\mathbf{r})}{\partial x^2} + \frac{\partial^2 g_1(\mathbf{r})}{\partial y^2}\right] + \frac{1}{2k^2}\frac{\partial^2 g_2(\mathbf{r})}{\partial x \partial y},\\
E_y &= g_2(\mathbf{r}) - \frac{1}{4k^2}\left[\frac{\partial^2 g_2(\mathbf{r})}{\partial x^2} + \frac{\partial^2 g_2(\mathbf{r})}{\partial y^2}\right] + \frac{1}{2k^2}\frac{\partial^2 g_1(\mathbf{r})}{\partial x \partial y},\\
E_z &= \frac{\mathrm{i}}{k}\left[\frac{\partial g_1(\mathbf{r})}{\partial x} + \frac{\partial g_2(\mathbf{r})}{\partial y}\right].
\end{aligned}
\tag{1.15}
$$

In order to apply these formulae to our case we assume $g_1(\mathbf{r}) = 0$ for TE mode, and $g_2(\mathbf{r}) = 0$ for TM mode. In conclusion defined in [55], we expect an appearance of the z component with an amplitude proportional to $k \sin\theta$ and an appearance of the cross-component with an amplitude proportional to $k^2 \sin^2\theta$.

1.3.1. Linearly polarized Bessel-X waves

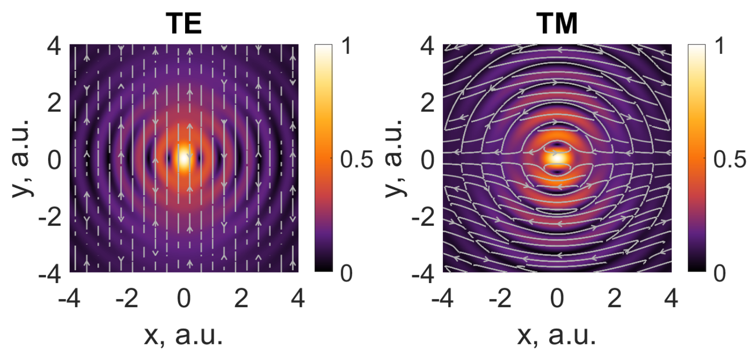

Figure 1.5: Linear transverse electric (TE) and transverse magnetic (TM) polarizations transverse intensity distributions for a Bessel-X beam. The white arrows represent the polarization direction.

To construct a linearly polarized Bessel-X wave (Figure 1.5), we select $\mathbf{a} = \mathbf{e_x}$, where $\mathbf{e_x}$ is a unitary vector oriented along the x-axis. We now substitute equation (1.12) into equation (1.13) and obtain the following expressions for the linearly polarized transverse electric and transverse magnetic Bessel-X waves. The transverse electric Bessel-X wave is given by

$$
\begin{aligned}
M_x &= 0,\\
M_y &= \sqrt{Z(d)}\mathrm{e}^{-\frac{\rho^2\sin^2\theta+d^2}{2\alpha^2c^2}}\left[J_m(A)\cos\theta\left(-\frac{z\cos\theta}{c^4\alpha^2}+\frac{\mathrm{i}\omega_0}{c}+\frac{\mathrm{i}}{2\omega_0\alpha^2cZ(d)}\right)\right.\\
&\qquad \left.+J_m'(A)_z\right]\mathrm{e}^{\mathrm{i}m\varphi+\mathrm{i}\omega_0 d},\\
M_z &= -\sqrt{Z(d)}\mathrm{e}^{-\frac{\rho^2\sin^2\theta+d^2}{2\alpha^2c^2}}\left[J_m(A)\left(-\frac{\rho\sin^2\theta}{\alpha^2c^2}\sin\varphi+\frac{\mathrm{i}m}{\rho}\cos\varphi\right)\right.\\
&\qquad \left.+J_m'(A)_\rho\right]\mathrm{e}^{\mathrm{i}m\varphi+\mathrm{i}\omega_0 d},
\end{aligned}
\tag{1.16}
$$

where $A = Z(d)\rho\omega_0\sin\theta/c$. We note that the M_x component is absent and the vortical term $\mathrm{e}^{\mathrm{i}m\varphi}$ is present in the M_y and M_z components so the transverse electric Bessel-X beam is a linearly polarized vortical structure. The absence of the M_x component can be explained by the difference in the derivation of Equation (1.15) and Equation (1.13). Linear polarization affects the z component by splitting its intensity profile into two parts: near the axis, the dependency is modulated by $\cos\varphi$, while further away from the axis, it is modulated by $\sin\varphi$.

The transverse magnetic Bessel-X wave has a more complex expression, which is given by

$$
\begin{aligned}
N_x &= \frac{\mathrm{e}^{im\varphi}}{k}\left[(f''_{1zz}f_2+2f'_{1z}f'_2+f_1f''_2+f'_{1\rho}f_2-\frac{m^2}{\rho^2}f_1f_2)\cos^2\varphi\right.\\
&\qquad \left.-(f''_{1zz}f_2+2f'_{1z}f'_2+f_1f''_2+f''_{1\rho\rho}f_2)\sin\varphi\cos\varphi\right],\\
N_y &= \frac{\mathrm{e}^{im\varphi}}{k}\left[\frac{\mathrm{i}m}{\rho^2}(f_1f_2+\rho f'_{1\rho}f_2)\right.\\
&\quad \left.+\,(2f''_{1zz}f_2+4f'_{1z}f'_2+2f_1f''_2+f''_{1\rho\rho}f_2+f'_{1\rho}f_2-\frac{m^2}{\rho^2}f_1f_2)\sin\varphi\cos\varphi\right],\\
N_z &= \frac{\mathrm{e}^{im\varphi}}{k}\left[\left(f''_{1z\rho}f_2+f'_{1\rho}f_2\right)\cos\varphi-\frac{\mathrm{i}m}{\rho}\left(f'_{1z}f_2+f_1f'_2\right)\sin\varphi\right].
\end{aligned}
\tag{1.17}
$$

Here, for the sake of convenience, we have introduced two shorthand notations:

$$
\begin{aligned}
f_1(\rho,z) &= \mathrm{e}^{-\frac{\rho^2\sin^2\theta+d^2}{2\alpha^2c^2}}J_m\left[\frac{Z(d)\rho\omega_0\sin\theta}{c}\right],\\
f_2(z) &= \sqrt{Z(d)}\mathrm{e}^{\mathrm{i}\omega_0 d}.
\end{aligned}
\tag{1.18}
$$

As expected from Equation (1.15) the cross-polarized component N_y appears. Although the expression is now more complex, the vortical nature is represented by the term $\mathrm{e}^{im\varphi}$ the leading component is N_y as the field is linearly polarized in the y direction. The z component N_z rotates by 90 degrees compared to the previous case.

1.3.2. Radially and azimuthally polarized Bessel-X waves

Radially and azimuthally polarized Bessel-X waves (see Figure 1.6) are constructed from the scalar solution; see Equation (1.12), by replacing the vector $\mathbf{a} = \mathbf{e_x}$ in Equation (1.13) with vector $\mathbf{e_z}$. The results of this operation for the transverse electric(azimuthally polarized) Bessel-X beam are given by

$$\begin{gathered} M_\rho = \frac{im}{\rho}\sqrt{Z(d)}\mathrm{e}^{-\frac{\rho^2\sin^2\theta+d^2}{2\alpha^2c^2}} J_m\left[Z(d)\frac{\rho\omega_0\sin\theta}{c}\right]\mathrm{e}^{\mathrm{i}m\varphi+\mathrm{i}\omega_0 d}, \\ M_\varphi = \sqrt{Z(d)}\mathrm{e}^{-\frac{\rho^2\sin^2\theta+d^2}{2\alpha^2c^2}}\left(J_m\left[Z(d)\frac{\rho\omega_0\sin\theta}{c}\right]\frac{\rho\sin^2\theta}{\alpha^2c^2}-\right. \\ \left.\left\{J_{m-1}\left[Z(d)\frac{\rho\omega_0\sin\theta}{c}\right]-J_{m+1}\left[Z(d)\frac{\rho\omega_0\sin\theta}{c}\right]\right\}\frac{Z(d)\omega_0\sin\theta}{2c}\right)\mathrm{e}^{\mathrm{i}m\varphi+\mathrm{i}\omega_0 d}, \\ M_z = 0. \end{gathered} \tag{1.19}$$

First, we note the absence of the longitudinally polarized component $M_z = 0$. Next, we note that the radial component $M_\rho = 0$ if the topological charge $m = 0$, thus the field is purely azimuthal. However, the radial component does appear if the topological charge $m \neq 0$. Both components have the optical vortex term $\mathrm{e}^{im\varphi}$, so they can be referred to as azimuthally or radially polarized vortices located at the core of a Bessel-X wave.

The transverse magnetic(radially polarized) Bessel-X wave is expressed by

$$\begin{aligned} N_\rho &= \frac{\mathrm{e}^{im\varphi}}{k}\left(f''_{1\rho z}f_2 + f'_{1\rho}f'_2\right), \\ N_\varphi &= \frac{im\mathrm{e}^{im\varphi}}{k\rho}\left(f'_{1z}f_2 + f_1f'_2\right), \\ N_z &= -\frac{f_2\mathrm{e}^{im\varphi}}{k\rho}\left(\rho f''_{1\rho\rho} + f'_{1\rho} - \frac{m^2}{\rho}f_1\right). \end{aligned} \tag{1.20}$$

In this case, when $m = 0$ the azimuthal component $N_\varphi = 0$, so the radial and longitudinal components are present, similarly to the cases

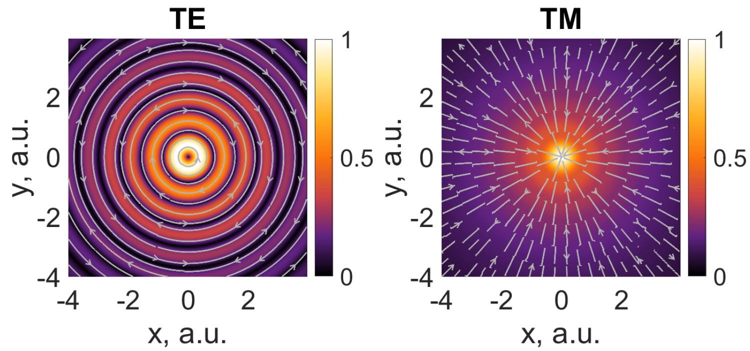

Figure 1.6: Azimuthal (TE) and radial (TM) polarizations transverse intensity distributions for a Bessel-X beam. The white arrows represent the polarization direction.

of radially polarized light which are already known. However, when the topological charge $m \neq 0$, all 3 field components are present and their phase portraits display distinct vortical structures.

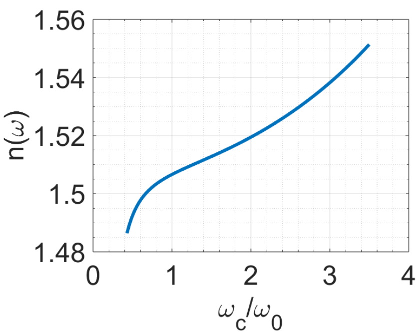

Figure 1.7: Refractive index curve for BK7 glass, as obtained from Sellmeiers equation for BK7 glass [121].

A non-diffracting wave packet is obtained when individual waves of different frequencies of a Bessel beam are combined in such a way that their longitudinal wave vectors form a linear dependency on the frequency. In this way, a non-diffracting wave packet is characterized by the angular dispersion dependence of its constituent components $\theta = f(\omega)$, which in a linear dispersive medium is written as follows:

$$k(\omega)\cos\theta = \frac{\omega}{V} + \gamma \tag{1.21}$$

Here $k(\omega) = \omega n(\omega)/c$ and θ is the cone angle of the monochromatic frequency ω of the Bessel beam's wave vector. The $n(\omega)$ is the refractive index of the medium, obtained using refractive index data provided in the literature [121]. The V is the group velocity of the focus wave mode, and γ is the propagation constant, which can be attributed to the integration constant [30], which represents the phase period of a resulting plane wave traveling at zero propagation angle ($\theta_0 = 0$). The constant V physically represents the propagation speed of the non-diffracting pulse beam. It should be noted that the angular dispersion curve $\theta = f(\omega)$ always changes the intensity profile of the pulse beam in the spatial region, and is a crucial factor in creating localized pulse beams during the experiment. The frequency ω is normalized to the frequency ω_0, corresponding to the zero of group velocity dispersion (GVD) in BK7 glass ($\lambda_0 = 1.356\ \mu m$).

1.5. Focus wave modes

For the investigation of the optical bullets (focus wave modes), we have selected one of the most common materials used for laser applications - the BK7 glass. The dielectric constants of BK7 glass are well known, the Sellmeier equations are easily accessible, and well researched. The feasibility of using BK7 glass for experiments is high due to its widespread use, availability, excellent optical properties, and cost effectiveness. Angular dispersion curves of BK7 glass allow us to represent the O- and X-shaped focus wave modes within the optical wavelength range, with available Light Conversion, PHAROS laser (wavelength of 1030 nm) and harmonics available at 515 nm, 343 nm, 258 nm, and 206 nm. We should take into account the maximum angle at the interface between the air and the glass, which limits the maximum feasible angle to 0.73 radians. At higher angles, we see the required incident angles become complex, which shows that evanescent waves would be required.

Nondiffracting and nondispersive wave packets usually are introduced within the frame of the cylindrical coordinate system and are perceived as a coherent superposition of monochromatic solutions of the respective cylindrical coordinate system. For such a coherent superposition to have nondiffracting and nondispersive properties, the wave vectors and frequencies within the wave packet have to correlate with each other. This requirement results in a wide range of different wave packets that are resistant to diffraction and dispersion. In this work, our aim is to investigate the so-called optical bullets, which are characterized by the following relation [3]:

$$k_z(\omega) = \frac{\omega}{c} n(\omega) \cos\theta = \frac{\omega}{V} + \gamma, \tag{1.22}$$

where k_z is the z component of the wave vector $\mathbf{k} = (k_\rho, 0, k_z)$, k_ρ is the transverse component of the wave vector, ω is the wave frequency, c is the speed of light, n is the refractive index of the material, θ is the angle between the z axis and the $\mathbf{k}$ vector, V is the group velocity of the focus wave mode, and γ is the propagation constant [3]. Sometimes, it can be attributed to the integration constant [30], which represents the phase period of a resulting plane wave traveling at zero propagation angle ($\theta_0 = 0$). This dependency (1.22) introduces the spatial-temporal relationship between the wave vector and the wave frequency. It can be visually perceived as the angular dispersion law for different frequencies:

$$\theta(\omega) = \arccos\left[\frac{c}{Vn(\omega)} + \frac{\gamma c}{\omega n(\omega)}\right]. \tag{1.23}$$

Substituting the relation between the vector k and the frequency of the wave into the general expression of the superposition of monochromatic waves results in the following integral expression:

$$E(\rho, \varphi, z, t) = \mathrm{e}^{\mathrm{i}\gamma z} \int_0^\infty S(\omega) J_m\left(k_\rho \rho\right) \mathrm{e}^{\mathrm{i}m\varphi} \mathrm{e}^{-\mathrm{i}\omega\tau} d\omega \tag{1.24}$$

where $\tau = t - z/V$ and m is the topological charge of the focus wave mode, (ρ, φ, z) are cylindrical coordinates.

The scalar focus wave modes are well known and have been studied. Our aim here is to construct their vector counterparts. Vectorial solutions of the Maxwell equations are constructed from solutions of scalar wave equations using the method given in Reference [56, 57], presented in Equation (1.13). Applying this operation to Equation (1.24) leads to the following expressions for transverse electric (TE) optical bullets:

$$\boldsymbol{M}(\boldsymbol{r}, t) = \mathrm{e}^{\mathrm{i}\gamma z} \int_0^\infty S(\omega) \boldsymbol{M}_0(\boldsymbol{r}; \omega) \mathrm{e}^{-\mathrm{i}\omega\tau} d\omega, \tag{1.25}$$

and transverse magnetic (TM) optical bullets:

$$\boldsymbol{N}(\boldsymbol{r},t) = \mathrm{e}^{\mathrm{i}\gamma z}\int_0^\infty S(\omega)\boldsymbol{N}_0(\boldsymbol{r};\omega)\mathrm{e}^{-\mathrm{i}\omega\tau}d\omega. \tag{1.26}$$

Vector functions $\boldsymbol{M}_0(\boldsymbol{r},\omega)$ and $\boldsymbol{N}_0(\boldsymbol{r},\omega)$ are basis vector functions of cylindrical coordinate systems obtained from Equation (1.13). Their exact expressions and physical interpretations depend on the choice of the vector **a**. We note here that, for anisotropic material, one has to determine basis vector functions separately. Given the birefringence, it has been reported on the deformations of Bessel beams traveling in anisotropic materials [122], so the question of whether the basis functions will still be described using cylindrical functions is open.

When $\mathbf{a} = \mathbf{e}_z$, the expressions resulting for $\boldsymbol{M}_0(\boldsymbol{r},\omega)$ and $\boldsymbol{N}_0(\boldsymbol{r},\omega)$ are

$$\boldsymbol{M}_0(\boldsymbol{r},\omega) = \left[\mathrm{i}\frac{m}{\rho}J_m\left(k_\rho\rho\right)\hat{\boldsymbol{e}}_\rho - J'_m\left(k_\rho\rho\right)\hat{\boldsymbol{e}}_\varphi\right]\mathrm{e}^{\mathrm{i}k_z z+\mathrm{i}m\varphi}, \tag{1.27}$$

where J'_m is the first derivative of the Bessel function of the m-th order. This expression describes an azimuthally polarized Bessel vortex beam.

$$\boldsymbol{N}_0(\boldsymbol{r},\omega) = \left[\mathrm{i}\frac{k_z}{k}J'_m\left(k_\rho\rho\right)\hat{\boldsymbol{e}}_\rho - \frac{mk_z}{k\rho}J_m\left(k_\rho\rho\right)\hat{\boldsymbol{e}}_\varphi + \frac{k_\rho^2}{k}J_m\left(k_\rho\rho\right)\hat{\boldsymbol{e}}_z\right] \times\mathrm{e}^{\mathrm{i}k_z z+\mathrm{i}m\varphi} \tag{1.28}$$

This expression describes a radially polarized Bessel vortex beam [55].

In the context of inhomogeneously polarized vector beams, the index m in Equations (1.27) and (1.28) can be assigned to the so-called polarization order p, see Reference [123].

When $\mathbf{a} = \mathbf{e}_x$, the resulting expressions for $\boldsymbol{M}_0(\boldsymbol{r},\omega)$ and $\boldsymbol{N}_0(\boldsymbol{r},\omega)$ are

$$\boldsymbol{M}_0(\boldsymbol{r},\omega) = \left\{\mathrm{i}k_z J_m\left(k_\rho\rho\right)\hat{\boldsymbol{e}}_y - \left[\sin\varphi J'_m\left(k_\rho\rho\right) + \mathrm{i}m\cos\varphi\frac{J_m\left(k_\rho\rho\right)}{\rho}\right]\hat{\boldsymbol{e}}_z\right\} \times\mathrm{e}^{\mathrm{i}k_z z+\mathrm{i}m\varphi} \tag{1.29}$$

where $\boldsymbol{e}_y$ is the unit vector of the Cartesian coordinate system. This expression describes a linearly polarized (in the y-direction) Bessel vortex beam.

$$
\begin{aligned}
\boldsymbol{N}_0(\boldsymbol{r},\omega) = \frac{1}{k}\Bigg(\Bigg\{ &- \frac{J'_m(k_\rho\rho)}{\rho}(\cos\varphi + \mathrm{i}m\sin\varphi) \\
&+ J_m(k_\rho\rho)\left[\frac{\mathrm{i}m}{\rho^2}(\sin\varphi - im\cos\varphi) + k_z^2\cos\varphi\right]\Bigg\}\hat{\boldsymbol{e}}_\rho \\
+ \Bigg[& J''_m(k_\rho\rho)\sin\varphi + \frac{J'_m(k_\rho\rho)}{\rho}\mathrm{i}m\cos\varphi \\
&- J_m(k_\rho\rho)\left(\frac{\mathrm{i}m}{\rho^2}\cos\varphi + k_z^2\sin\varphi\right)\Bigg]\hat{\boldsymbol{e}}_\varphi \\
+ \Bigg[& J'_m(k_\rho\rho)\,\mathrm{i}k_z\cos\varphi + \frac{J_m(k_\rho\rho)}{\rho}k_z m\sin\varphi\Bigg]\hat{\boldsymbol{e}}_z\Bigg)\mathrm{e}^{\mathrm{i}k_z z + \mathrm{i}m\varphi},
\end{aligned}
\tag{1.30}
$$

where J''_m is the second order derivative of the Bessel function of the m-th order. This expression describes a linearly polarized (in the x direction) Bessel vortex beam; see Reference [55] for a slightly different definition. We note here that these basis functions describe vector beams which are optical vortices with predominantly linearly polarized components.

Substitution of these four different basis functions into Equations (1.25, 1.26) gives integral expressions for vector optical bullets inside a dielectric material. The selection of the vector $\mathbf{a} = \mathbf{e}_z$ gives us azimuthally and radially polarized optical bullets, and the selection of the vector $\mathbf{a} = \mathbf{e}_x$ gives us linearly polarized (in the y and x directions) optical bullets. In general, these expressions cannot be analytically integrated, but integration can be performed under some strict conditions. For example, in the vacuum, when $\gamma = 0\ \mu m^{-1}$ and the spectral envelope $S(\omega)$ has a particular expression

$$
S(\omega) = \exp\left[-\Delta t^2 (\omega - \omega_c)^2 /4\right], \tag{1.31}
$$

then the integrals from Equations (1.25, 1.26) can be analytically evaluated to azimuthally and radially polarized pulsed Bessel-X vortices [1].

SIMULATIONS

This chapter describes the simulation methods and results, with discussions and conclusions of this work. The results have been published in [A1], [A2] and [A3] articles.

2. AZIMUTHALLY AND RADIALLY POLARIZED PULSED BESSEL-X VORTICES

2.1. Linearly polarized Bessel-X pulses

In this section, we systematically investigate and present a comparison of linearly polarized Bessel-X wave vortices with their radially/azimuthally polarized counterparts. We start by showcasing two cases (TM and TE modes) of linearly polarized Bessel-X waves with topological charge $m = 0$, see Figure 2.1. First, the choice of the vector used to construct vector solutions has caused the transverse electric mode to be polarized in the y direction, while the transverse magnetic solution is polarized in the x direction. As a consequence, the TE mode has no x component and the TM mode has a small y component. As the numerics reveals, the maximal intensities of the individual component do depend on the cone angle θ. As the angle θ increases, the z-component appears and at some values of the angle θ its intensity becomes equal to the intensity of the main component. For the transverse magnetic mode, we also observe

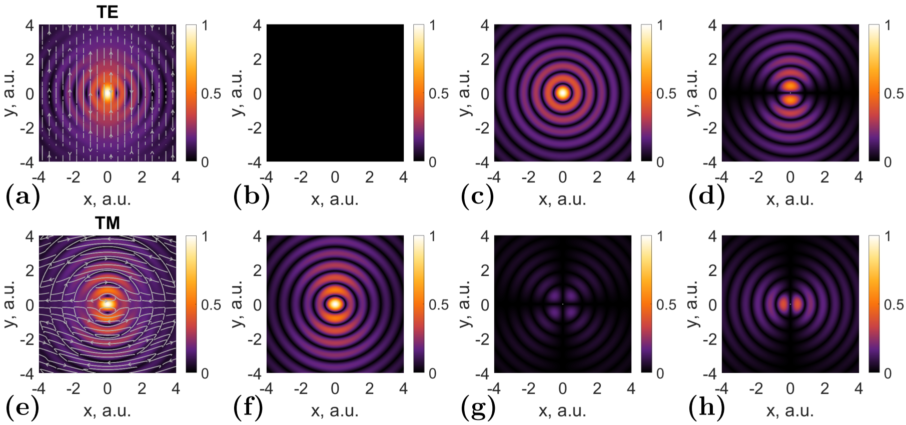

Figure 2.1: Intensity distributions of a linearly polarized Bessel-X pulses(a, e) and its individual components(E_x, (b, f), E_y, (c, g), E_z, (d, h)) in the transverse plane. The transverse electric mode is depicted in (a-d), and the transverse magnetic mode is depicted in (e-h). The white arrows depict the orientation of the electric field. The cone angle $\theta = 45°$, frequency $\omega_0 = 1.885\ fs^{-1}$ ($\lambda_0 = 1\mu m$), $\alpha = 1.06 \times 10^{-14}$ s. Topological charge $m = 0$.

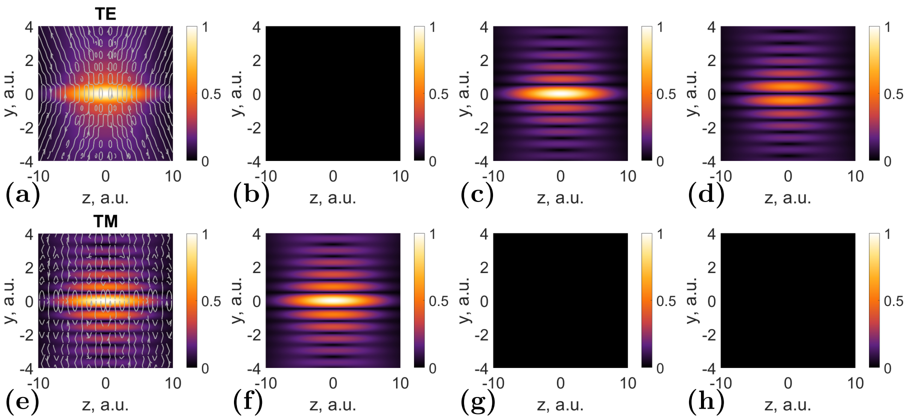

Figure 2.2: Intensity distributions of a linearly polarized Bessel-X pulses(a, e) and its individual components(E_x, (b, f), E_y, (c, g), E_z, (d, h)) in the longitudinal plane. The transverse electric mode is depicted in (a-d), and the transverse magnetic mode is depicted in (e-h). The white arrows depict the orientation of the electric field. The cone angle $\theta = 45°$, frequency $\omega_0 = 1.885\ fs^{-1}$ ($\lambda_0 = 1\ \mu m$), $\alpha = 1.06 \times 10^{-14}$ s. Topological charge $m = 0$.

a non-zero cross-component which becomes more intense as the cone angle increases. Although it always remains the smallest and weakest field component, it can become noticeable; see Figure 2.1 (g). Both modes have similar-looking z components that are rotated by 90 degrees when compared to one another. In both cases, the dominant component has a Bessel-like structure with the main lobe surrounded by a number of rings with decreasing amplitudes.

Next, we plot intensity distributions in the longitudinal plane see Figure 2.2. As the cone angle θ is relatively large, we observe the differences between the TE and TM modes. As the numerics reveal, for angles $\theta \approx 20°$ small differences are observed between TE and TM modes due to the non-zero z component in the TE mode. In this case, we have selected $\theta = 45°$, so the intensity of the z component is noticeable, and because of this we observe noticeable differences in the transverse profiles. As expected, the x component is absent in the TE mode, as is the y component in the TM mode due to the choice of the cross-section. The z component of the TM mode is 0 in this cross-section. We note that in both cases the distinct X-letter shape is clearly pronounced in the intensity distributions, see Figure 2.2 (a) and (e). This shape is

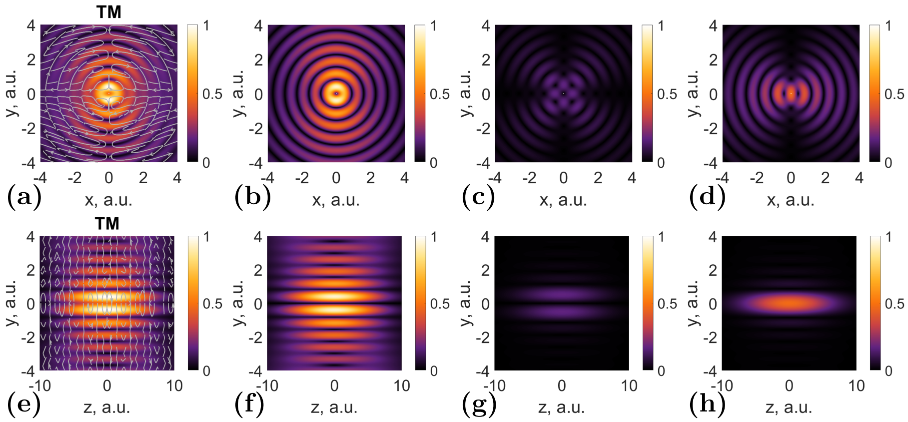

Figure 2.3: Intensity distributions of a linearly polarized transverse magnetic (TM) Bessel-X pulses(a, e) and its individual components(E_x, (b, f), E_y, (c, g), E_z, (d, h)) in the transverse(a-d) and longitudinal(e-h) planes. The white arrows depict the orientation of the electric field. The cone angle $\theta = 45°$, frequency $\omega_0 = 1.885\ fs^{-1}$ ($\lambda_0 = 1\ \mu m$), $\alpha = 1.06 \times 10^{-14}$ s. Topological charge $m = 1$.

preserved during diffraction(propagation) of the pulse in the free space.

Thus, the vectorization of the Bessel-X pulses for the case of linear polarization has resulted in the appearance of either a y- or x-polarized main component, a z-polarized component, and a cross-polarized component for the TM mode. As a next step, we look into the linearly polarized Bessel-X wave with an optical vortex of topological charge $m = 1$. In this case, we investigate only the transverse magnetic mode as it has a richer topology than the TE mode.

For the selected cone angle of $\theta = 45°$, all three field components are observed in the transverse plane. Their maximal intensities obey the considerations of Equation (1.15). The dominating component is the x component followed by the z component; the y component is observable, but has the smallest intensity of all three field components. Moreover, the beam has a topological structure in the center of the beam: an optical vortex in the x component and the appearance of opposite charge vortices in the z component. The y component has a rich four-lobe structure caused by the superposition of 2 vortices causing the splitting of the resulting field into a ring-like repeating structure with 4 single charged vortices on each ring [124].

The intensity distribution of a linearly polarized Bessel-X pulse vortex in the longitudinal plane is depicted in Figure 2.3(e-h). We observe a rather complex topological structure with the polarization state changing across the cross-section. This behavior is caused by the interaction of the x and z polarized components. As expected the x component is still the largest one, however, at the core of the vortex the z component dominates. The y component is present, but it has practically no influence on the total resulting field.

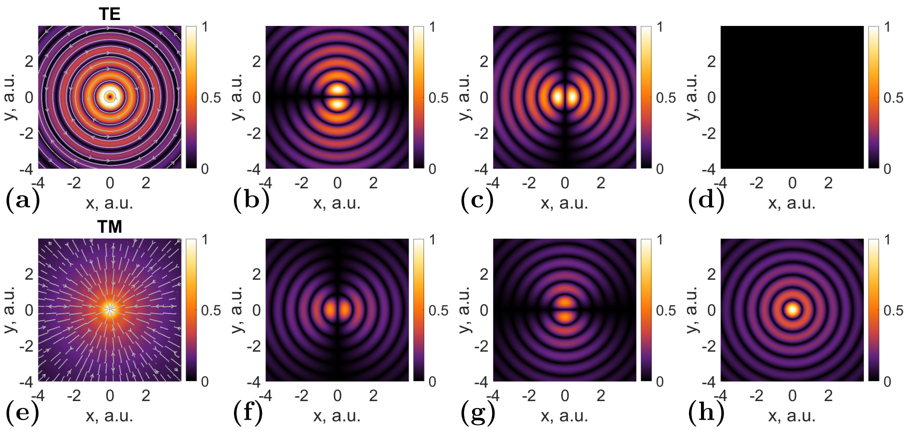

Figure 2.4: Intensity distributions of a azimuthally(a-d) and radially(e-h) polarized Bessel-X pulses(a, e) and their individual components(E_x, (b, f), E_y, (c, g), E_z, (d, h)) in the transverse plane. The white arrows depict the orientation of the electric field. The cone angle $\theta = 45°$, frequency $\omega_0 = 1.885\ fs^{-1}$ ($\lambda_0 = 1\ \mu m$), $\alpha = 1.06 \times 10^{-14}$ s. Topological charge $m = 0$.

Now we move on to the presentation of the numerical simulation of radially and azimuthally polarized Bessel-X pulse vortices. For the start, we choose $m = 0$ and consider fundamental radially and azimuthally polarized modes. As we are interested in the effects caused by nonparaxiality, the choice of the cone angle remains the same.

The intensity distributions of azimuthally polarized Bessel-X pulse and its individual components in the transverse plane are depicted in Figures 2.4(a-d). Here, we note the inhomogeneous polarization structure characteristic of the azimuthally polarized state of light: the orientation of the electric field depends on the azimuthal value, and the electric field experiences clockwise and counterclockwise rotation depending on the radius in the transverse plane. As a result, the field consists of 2 dominating components with equal intensities and are rotated by 90 degrees in respect to one another. As expected, no z component is present, though we could expect it to appear by looking at Equation (1.15). This happens because the magnitude of derivatives in Equation (1.15) are opposite, so they cancel out, and as a result, no z-component is present.

The case of the radially polarized Bessel-X pulse is presented in Figure 2.4(e-h). We observe a clearly distinguishable polarization structure characteristic of the radially polarized state of light. Two dominating linearly polarized field components are present, and they are also rotated by 90 degrees in respect to one another. Due to the non-paraxiality, the dominating linearly polarized components of the TM mode slightly differ from the dominating components of the TE mode. The main difference is the appearance of the z polarized field components, see Figure 2.4(h). Most importantly, the total intensity of the z component is larger than the maximal intensity of the linearly polarized components. This outcome is in line with previous studies and is a manifestation of the fact that the radially polarized field can be focused to a sharper spot than the linearly polarized pulsed beam [38, 125].

The non-diffracting properties of the Bessel-X pulses define their intensity distributions in the longitudinal plane. Next, we look at how the polarization properties interact with non-diffracting properties by plotting the intensity distributions of TE and TM modes in the longitudinal plane, see Figure 2.5. First, because the azimuthally polarized (TE mode) is purely transverse, we did not observe the orientation of the electric field in the xz plane. Due to the choice of the cross-sectional plane, we observe a single-field component. It has a distinct X-letter shape, modified by the presence of a polarization singularity on the axis of propagation. The radially polarized (TM mode) Bessel-X pulse has a complex observable polarization pattern caused by the interplay of the x and y components. In the center of the beam where the x component has a polarization singularity, the total field is predominantly z polarized. At points where the z component is small, we observe a field oriented along the x direction. As a result, the polarization state in the longitudinal plane rotates around the points located between the zeros

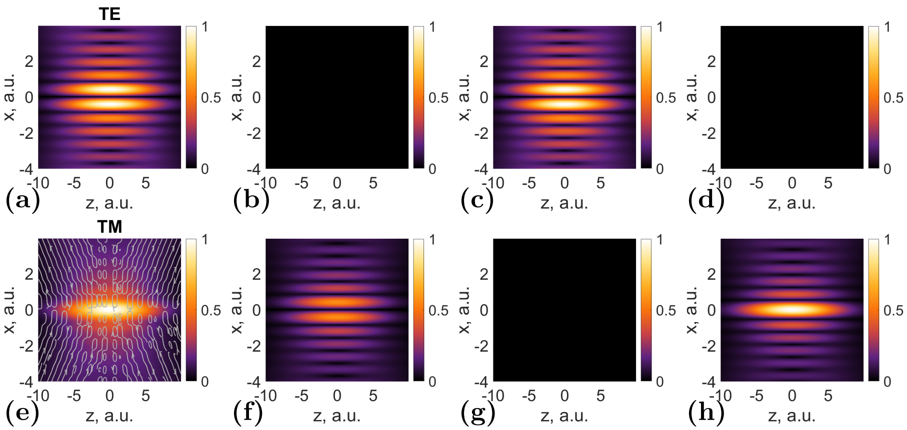

Figure 2.5: Intensity distributions of a azimuthally(a-d) and radially(e-h) polarized Bessel-X pulses(a, e) and their individual components(E_x, (b, f), E_y, (c, g), E_z, (d, h)) in the longitudinal plane. The white arrows depict the orientation of the electric field. The cone angle $\theta = 45°$, frequency $\omega_0 = 1.885\ fs^{-1}$ ($\lambda_0 = 1\ \mu m$), $\alpha = 1.06 \times 10^{-14}$ s. Topological charge $m = 0$.

of the x and z components. The polarization state in the lobes of the X letter is oriented along the lobes; see Figure 2.5(e).

We come forward to include in simulations of radial and azimuthal Bessel-X pulses yet another parameter - the topological charge m. The interplay of vorticity and inhomogeneous polarization is known to result in vector vortices and polarization singularities with rather complex structures. In this numerical experimentation, we keep the cone angle θ the same and start by presenting intensity distributions of the azimuthally polarized Bessel-X vortex, see Figure 2.6(a-d). As the polarization map reveals, see Figure 2.6(a), the beam consists of two parts- on the right-hand side the azimuthal polarization rotates in opposite direction to the polarization on the left-hand side. This is a distinct manifestation of the inhomogeneously polarized vortex state. The separating line rotates when time dependence is introduced. Yet another interesting property of the beam is the central part of the beam, where the polarization is circularly polarized and the beam is focused tighter than its linearly polarized counterpart. Similar behavior is already known in the so-called complex source vortices [44]. The individual linearly polarized constituencies are symmetric and rotated by 90 degrees with respect to one another. Both components appear as substitutes for single

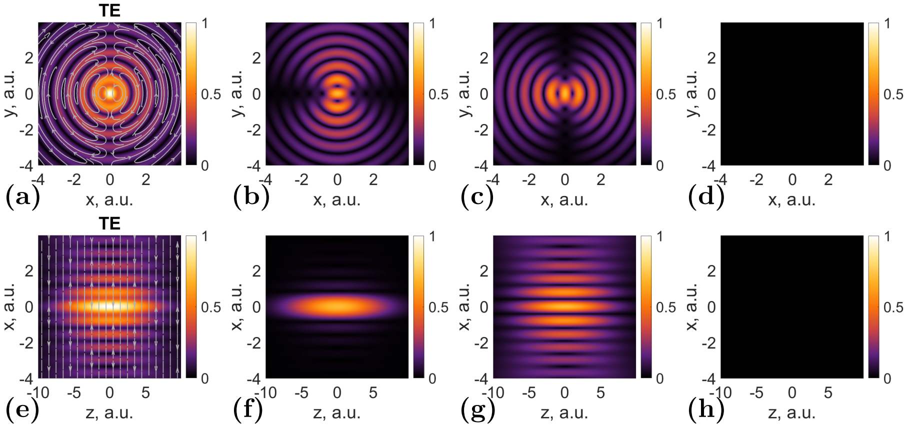

Figure 2.6: Intensity distributions of an azimuthally polarized transverse electric(TE) Bessel-X pulses(a, e) and their individual components (E_x, (b, f), E_y, (c, g), E_z, (d, h)) in the transverse(a-d) and longitudinal(e-h) planes. The cone angle $\theta = 45°$, frequency $\omega_0 = 1.885\ fs^{-1}$ ($\lambda_0 = 1\ \mu m$), $\alpha = 1.06 \times 10^{-14}$ s. Topological charge $m = 1$.

charged vortices of opposite signs; see Figure 2.6(b, c). The propagation dynamics are given in Figure 2.6(e, h). Because of the absence of the z component, the electric field is polarized in the transverse direction. Most notably the cross-sections of the x and y components are different with the y component having a distinct X letter shape which is hardly distinguishable in the x component.

The radially polarized Bessel-X vortex has all three field components present and the vorticity of the radially polarized mode is also observed see Figure 2.7. However, in this case, the separating line coincides with the x-axis. For this reason, in the upper part of the picture, the orientation of the electric field is a reflection of the lower part of the picture. Moreover, the presence of the z component makes the focal spot not so small as it was in the previous case. The on-axis polarization is a mix of circular and longitudinal. In the center, the field has circular polarization rotating in the opposite direction to the previous cases, but as we move to the local maxima of the z component it becomes longitudinally polarized. These points form a ring-shaped structure around the focal spot; see Figure 2.7(a). The situation in the longitudinal plane is somewhat similar to the case discussed previously of the azimuthally polarized Bessel-X vortex. First, because of the presence of all three components, we observe a collection of regions where polarization ro-

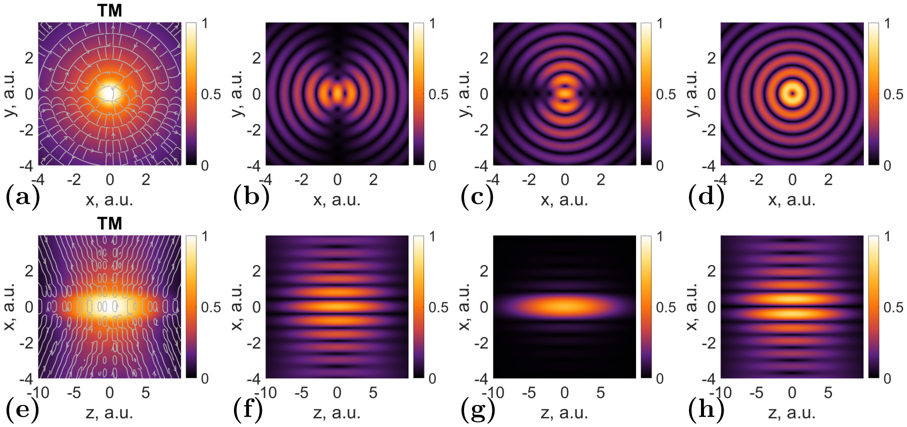

Figure 2.7: Intensity distributions of an radially polarized transverse magnetic(TM) Bessel-X pulses(a, e) and their individual components(E_x, (b, f), E_y, (c, g), E_z, (d, h)) in the transverse(a-d) and longitudinal(e-h) planes. The cone angle $\theta = 45°$, frequency $\omega_0 = 1.885\ fs^{-1}$ ($\lambda_0 = 1\ \mu m$), $\alpha = 1.06 \times 10^{-14}$ s. Topological charge $m = 1$.

tates in the xz plane. These regions are located mainly on the x-axis. The polarization on the lobes of the X letter is oriented along the X letter. The X letter is easily distinguishable in the x and z components but is hardly pronounced in the y component.

Here, we note that we have used a scalar Bessel-X wave with topological charge $m = 1$ and an optical vortex with a screw-like phase front at its core for the derivation of inhomogeneously polarized vector vortices. However, the end result is circularly polarized on the axis. This might be referred to as the conversion of the orbital angular momentum to spin angular momentum of light and was reported in Ref. [44]. For this reason, we are interested in situations with topological charges greater than one ($m > 1$). Due to this reasoning, we numerically simulate intensity distributions of azimuthally polarized Bessel-X vortex of topological charge $m = 2$, see Figure 2.8. Once again, in the transverse plane, we observe four regions where the rotation of the electric field experiences changes. These regions are built by diagonal lines ($y = x, y = -x$). As the z-component is absent, the field is dominated by two equally strong linearly polarized components. However, in this case, a single charged vortex is present in the center of each individual component with two opposite-sign vortices located a bit farther from the center of the com-

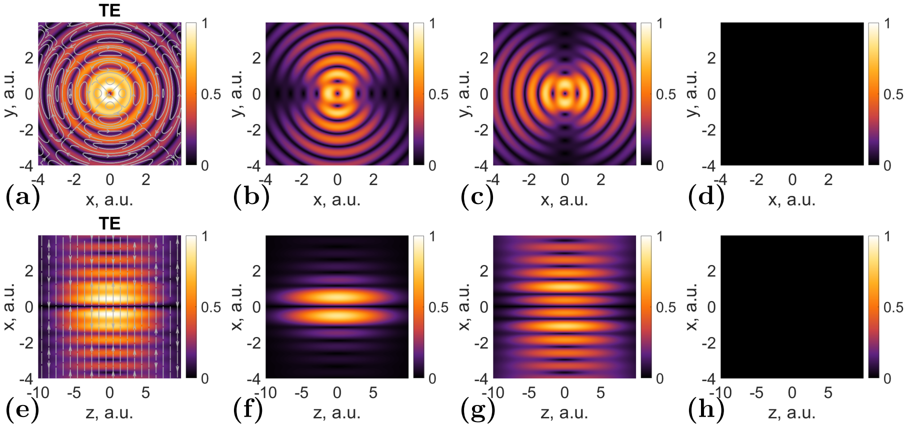

Figure 2.8: Intensity distributions of an azimuthally polarized transverse electric(TE) Bessel-X pulses(a, e) and their individual components(E_x, (b, f), E_y, (c, g), E_z, (d, h)) in the transverse(a-d) and longitudinal(e-h) planes. The cone angle $\theta = 45°$, frequency $\omega_0 = 1.885\ fs^{-1}$ ($\lambda_0 = 1\ \mu m$), $\alpha = 1.06 \times 10^{-14}$ s. Topological charge $m = 2$.

ponent. Intensity distributions are rotated by 90 degrees, with respect to one another.

The situation in the longitudinal plane is similar to the previous case, however, there is no intensity on the axis of propagation due to the presence of the singularity. Most notably, the X letter is more recognizable in the y component than in the x component due to the choice of the cross-section plane.

2.3. Vector Bessel-X pulse components

To summarise we now investigate the behavior of individual electric field components for different values of the cone angle θ, see Figure 2.9. As expected for relatively small angles of the Bessel-X pulse cone, the linearly polarized component dominates the fields in all cases. However, this situation changes as the angles greater than 20 degrees are approached. For the linearly polarized TE mode, the z components start to appear and depending on the topological charge become equal to the transverse component at approximately 50-60 degrees. The situation is repeated for the linearly polarized TM mode, though we additionally observe an appearance of the cross-component x. For the radially polarized Bessel-

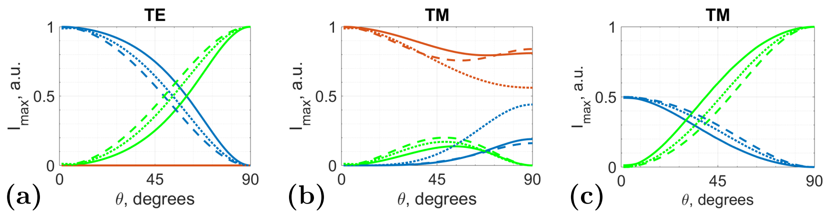

Figure 2.9: Normalized intensities of individual components of vector Bessel-X pulses for various cone angles θ for linearly polarized TE mode (a), linear TM mode (b), and radially polarized mode (c). Topological charges are $m = 0$(solid line), $m = 1$(dashed line), $m = 2$(dotted line). The E_x component is in red, E_y is in blue and E_z is in green. In (c), the E_x and E_y components overlap.

X pulse the dominating role of the longitudinal component is manifested at small values of the cone angle θ, see Figure 2.9(c). In this case, the increasing topological charge m decreases the importance of the longitudinal component. The cause for that is the fact that in the case of radial polarization the field structure for $m = 0$ contains no optical vortices and the z component is sharply focused. When the topological charge increases, the z component contains topological structures, so its maximal value is smaller.

2.4. Temporal parameters

Lastly, we ask ourselves whether the vectorial structure of the Bessel-X waves influences its temporal parameters. In the case of a scalar Bessel-X wave, see Equation (1.12) parameter α is directly proportional to the duration of the pulse and the temporal shape resembles a Gaussian one. However, as we introduce vector properties, two additional electric field components appear, see Equation (1.16, 1.17, 1.19, 1.20). An inspection of these components reveals not only changes in the temporal profile, but also angle-dependent relative amplitudes. For this reason, we expect the durations τ of the vector Bessel-X waves to depend on the cone angle; see Figure 2.10 (a, c). We select a particular value of the parameter α and three different topological charges m. For the linearly polarized Bessel-X wave, we see a distinct effect caused by the non-paraxiality. For small angles θ, the FWHM durations τ of all pulses are more or less similar. As the angle increases, durations of vortices are becoming

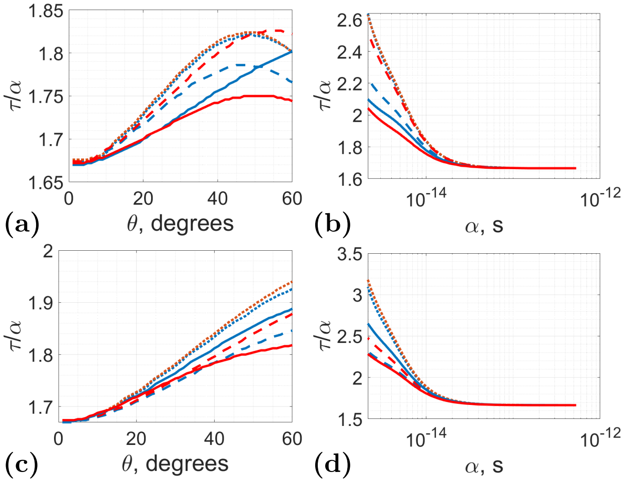

Figure 2.10: Dependencies of FWHM durations of vector Bessel-X pulses (a, c) on cone angles θ and (b, d) on the parameter α for the cases of (a, b) linear polarizations(blue curves-TE, and red curves-TM) and (c, d) azimuthal and radial polarizations(blue curves-radial, and red curves-azimuthal). Topological charges are $m = 0$(solid line), $m = 1$(dashed line), $m = 2$(dotted line). The frequency is $\omega_0 = 1.885\ fs^{-1}$ ($\lambda_0 = 1\ \mu m$) and parameter $\alpha = 1.06 \times 10^{-14}$ s (a, c) and $\theta = 45°$ (b, d).

larger and we note different durations for TE and TM modes. This effect is expected because the presence of the optical vortex results in larger dimensions in all 3 dimensions of the optical Bessel-X bullet. As the angle further increases, we observe a drop in durations caused by the temporal reshaping of the wave packet - the temporal dependency of the resulting pulse is not Gaussian anymore, which makes an estimation of the FWHM duration τ complicated. Moving on to the radially and azimuthally polarized Bessel-X pulses, we observe a similar behavior. Small cone angles θ do not influence the durations of vector Bessel-X pulses with different topological charges, see Figure 2.10(c). We first observe the separation of the FWHM durations τ according to the topological charge, followed by the separation of the durations for the TE and TM modes. In particular, the duration of the vortical Bessel-X pulse ($m = 1$) is comparable to the radial or azimuthal polarization Bessel-X pulse. Radially and azimuthally polarized Bessel-X pulses with topological charges larger than ($m = 2$) have durations that increase with increasing topological charge. This conclusion is also valid for linearly polarized Bessel-X vortices.

Next, we fix the cone angle θ to the value of $\theta = 45°$ and investigate how the inverse spectral width α influences the resulting FWHM pulse durations τ. The dependencies of the normalized FWHM duration τ/α dependencies are presented in Figure 2.10 (b, d). As expected, for longer pulses, we do not observe differences between polarizations and topological charges, and the observed duration τ/α remains constant. However, when the pulse durations approach values of tens of femtoseconds, we start to notice differences between topological charges and polarizations. This might be caused by inaccuracies in the approximation in Equation (1.12), furthermore, this might require an additional further investigation using Equation (1.10).

2.5. Summary of the results

We have devised analytical expressions for vector Bessel-X pulses with inhomogeneously polarized vortices for three selected cases: (a) linear polarization, (b) azimuthal polarization, and (c) radial polarization. We have numerically investigated the expressions obtained in a wide range of cone angles θ and parameters α. Whereas the topological structure of the main component of the linearly polarized Bessel-X pulse does contain a topological singularity. The main components of the radially and azimuthally polarized Bessel-X vortices ($m = 1$) demonstrate a transformation of the topological singularity from the phase singularity to the polarization singularity. The polarization structure of radially and azimuthally polarized Bessel-X pulses is rather complicated for higher topological charges; the behavior of the electric field in the focal plane resembles so-called radially and azimuthally polarized vortices [44].

The vectorial structure of linearly and radially/azimuthally polarized Bessel-X pulses changes the FWHM durations. This effect becomes more pronounced as the situation becomes non-paraxial with increasing cone angle θ. The dynamics of this dependency is nontrivial and different for linear and radial-azimuthal polarizations. In the case of radial/azimuthal polarization, the case with topological charge $m = 1$ stands out because the durations are similar to those of the case with pure radial/azimuthal polarization.

For the given cone angle θ the FWHM duration depends linearly on the parameter α. However, as femtosecond durations are reached this behavior is reverted and the analytical model predicts differences between polarizations and topological charges, which might need further studies.

3. VECTOR OPTICAL BULLETS IN DIELECTRIC MEDIA: POLARIZATION STRUCTURES AND GROUP VELOCITY EFFECTS

3.1. Vector optical bullets in dielectric material

In this section, we systematically investigate and present a comparison of linearly polarized optical bullets with their radially/azimuthally polarized counterparts in the dielectric material. These results have been published in my article [2]. We selected a BK7 glass for this investigation, but note that these steps can be easily applied to any other material whose dispersion can be described using a Sellmeier formula [126]. The angular dispersion of the focus wave modes is described by Equation (1.23). The properties of such dispersion curves have already been extensively studied in the literature, see Reference [3], so we shall briefly recall them without diving into the problematics.

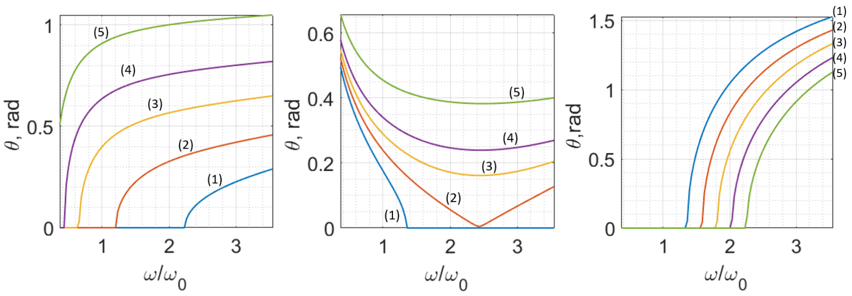

Figure 3.1: (**a**) Angular dispersion of the optical bullet inside the BK7 glass, when $\gamma = 1.25\ \mu m^{-1}$, and V/c: 0.7 (1), 0.75 (2), 0.85 (3), 1 (4), 1.4 (5). (**b**) Angular dispersion of the optical bullet within the BK7 glass, when $\gamma = -0.628\ \mu m^{-1}$, and V/c: 0.629 (1), 0.63685 (2), 0.645 (3), 0.65495 (4), 0.685 (5), (**c**) Angular dispersion of the optical bullet within the BK7 glass, when $V/c = -1.2$, and γ: $6\pi\ \mu m^{-1}$ (1), $7\pi\ \mu m^{-1}$ (2), $8\pi\ \mu m^{-1}$ (3), $9\pi\ \mu m^{-1}$ (4), $10\pi\ \mu m^{-1}$ (5). The frequency is normalized to the value of $\omega_0 = 1.389 fs^{-1}$

An example of angular dispersion curves for BK7 glass is shown in Figure 3.1 for a few selections of group velocities V/c and parameters γ. The central frequency of the beam ω_c is normalized to the frequency

ω_0, corresponding to the zero group-velocity dispersion (GVD) in BK7 glass. In the first case, we select a positive value of $\gamma = 1.25\ \mu m^{-1}$ and change the group velocity values V/c. As a result, we observe the angular dispersion that increases monotonically with frequency. The main feature of these dependencies is that the range of frequencies where the optical bullet exists changes with velocity; see Figure 3.1 (a). In the second case, we select one particular negative value of $\gamma = -0.628\ \mu m^{-1}$ to plot the angular dispersions for 5 different values of the group velocity, see Figure 3.1 (b). This case is especially interesting as a demonstration of the rich and complex dependencies of the angular dispersion. Moreover, for some values, we observe monotonically decreasing angles for single-wave components, which after reaching the inflection point start to increase. At a particular value of the group velocity V/c, the inflection point touches the frequency axis. A further change in the group velocity results in the dispersion curve splitting into two parts; see Figure 3.1 (b). In the last example, we selected a negative group velocity $V/c = -1.2$ to show the possibility of creating a backward propagating optical bullet inside the dielectric material; see Figure 3.1 (c) and plot dispersion curves for a selection of parameters γ.

Before proceeding to the analysis of numerical simulations, we note that the situation depicted in Figure 3.1 (b) is the most interesting and most studied in the literature, as for the scalar optical bullets, the rich dynamics of spatiotemporal profiles is observed. Usually, the optical bullets have a spatial profile that resembles the capital Latin letter X; for this reason, the optical bullets are very often called mistakenly X-waves or Bessel-X pulses, although the latter solutions are obtained as a particular case of the focus wave modes with parameter $\gamma = 0\ \mu m^{-1}$ and very specific and distinct expressions of the spectral envelope S_ω. Yet another example of the transformations in the spatiotemporal profile of the nondiffracting and nondispersive focus wave mode is the change to the capital Latin letter O, caused by specific angular dispersion due to which the peripheral intensities merge together; see References [3, 31, 127].

Motivated by this particular case having great attention in the literature we select one particular angular dispersion curve from the Figure 3.1 (b), when $\gamma = -0.628\ \mu m^{-1}$ and $V/c = 0.63685$, as this is the case with most changes in the spatiotemporal profile of the vector optical bullet. For this study, we introduce the rectangular shape of the spectral envelope $S(\omega) = \Pi(\omega_c - \omega/d\omega)$, where

$$\Pi\left(\frac{\omega}{d\omega}\right) = \begin{cases} 0, & \text{if } |\omega| > \frac{d\omega}{2}, \\ \frac{1}{2}, & \text{if } |\omega| = \frac{d\omega}{2}, \\ 1, & \text{if } |\omega| < \frac{d\omega}{2}, \end{cases} \tag{3.1}$$

where the $d\omega$ is the spectral width of the rectangular spectral envelope, ω_c is the central frequency of the wave packet. For the rectangular spectral envelope, the spectral width $d\omega$ can be related to the temporal duration dt using the expression $d\omega = 5.56/dt$ [128].

In further numerical simulations, we numerically integrate Equations (1.25, 1.26) using the aforementioned expression for the spectral envelope. For our convenience, we select one particular value of the pulse duration $dt = 100$ fs and two particular values of the central frequency, one giving us an example of the so-called X spatiotemporal profile, and another giving us an example of the so-called O spatiotemporal profile.

3.2. X- shaped optical bullets

We start our simulations by choosing $\mathbf{a} = \mathbf{e}_x$, which gives us two linearly polarized optical bullets. The case of the transverse electric optical bullet(the main component is the y component). We present the results in Figure 3.2. The longitudinal intensity profile of the vector optical bullet is depicted in Figure 3.2 (a). We note a distinct cross profile, which is the cause of the most used name for the optical bullets, and a clear resemblance to the capital X letter is observed. In Figure 3.2 (b) we depict the total intensity profile of the transverse electric optical bullet in the $\tau = 0$ plane. The streamlines depict the orientation of the electric field. In Figure 3.2 (c-e), we demonstrate individual electric field components of the vector optical bullet. The component x is absent due to the transversality of the electric field with respect to $\mathbf{a} = \mathbf{e}_x$. The main dominant component is the y component, and the main effect of vectorization of the scalar optical bullet is the appearance of the z component, see Figure 3.2 (e).

In the next numerical simulation, we turn our attention to the transverse magnetic focus wave mode, see Figure 3.3. The intensity distribu-

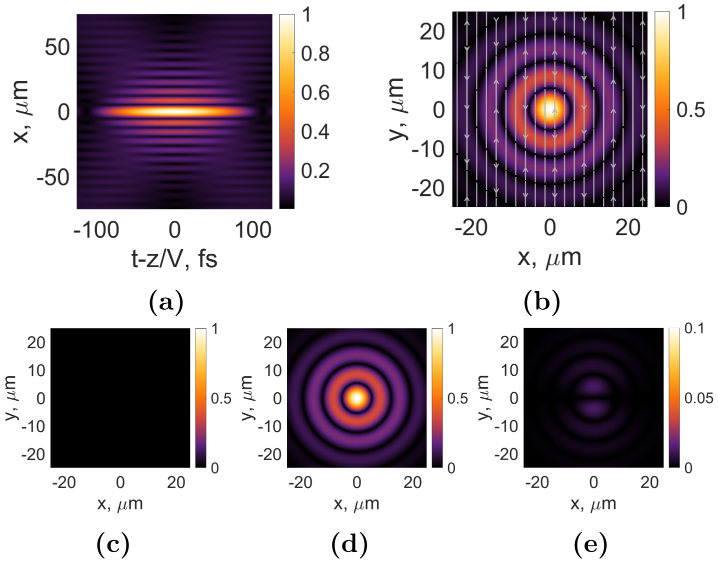

Figure 3.2: Intensity distributions of transverse electric (TE) linearly polarized optical bullets and its individual components(E_x, (**c**), E_y, (**d**), E_z, (**e**)) in the transverse plane. The white arrows represent the orientation of the electric field. The frequency $\omega_c = 4\ fs^{-1}$. Topological charge $m = 0$, pulse duration $dt = 100\ fs$, $V/c = 0.63685$, $\gamma = -0.628\ \mu m^{-1}$.

tion of the transverse magnetic optical bullet in the longitudinal plane is presented in Figure 3.3 (a). Due to the selection of the central carrier frequency ω_c, in both cases we end up with relatively moderate angles of the angular dispersion curve. For this reason, the electric intensity distribution in Figure 3.3 (a) is similar to the one in Figure 3.2 (a). The main difference is revealed in Figure 3.3 (b), where the transverse intensity distribution is depicted together with the streamlines with the electric field. A closer look at the individual electric field components, see Figure 3.3 (c-e), shows that the dominating electric field component is the x component, the z component is present as in the previous case, but it is rotated by 90 degrees. The most notable change is the presence of the cross-polarized (y component), which is diminishingly small due to the rather modest angles of the angular dispersion curve.

We start our investigation of inhomogeneously polarized optical bullets ($\mathbf{a} = \mathbf{e}_z$) by analyzing the case of azimuthally polarized optical pulse. For this purpose we use Equation (1.27) and obtain individual electric field components by integration of Equation (1.25). As in the

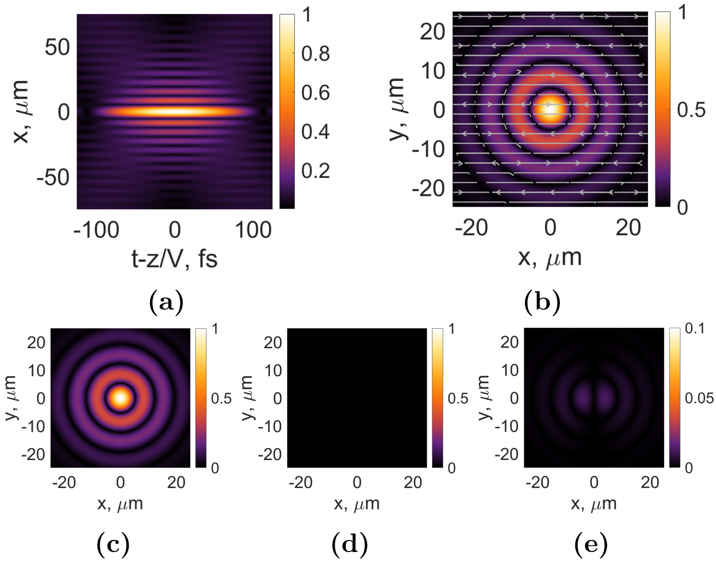

Figure 3.3: Intensity distributions of transverse magnetic (TM) linearly polarized optical bullets and its individual components(E_x, (**c**), E_y, (**d**), E_z, (**e**)). The white arrows represent the orientation of the electric field. Frequency $\omega_c = 4\ fs^{-1}$. Topological charge $m = 0$, pulse duration $dt = 100\ fs$, $V/c = 0.63685$, $\gamma = -0.628\ \mu m^{-1}$.

previous case, we chose the same parameters to obtain an azimuthally polarized optical pulse with the X letter in the longitudinal plane, see Figure 3.4.

First, we note a hollow center of the optical pulse (see Figure 3.4 (a)), which is caused by the presence of a polarization singularity on the optical axis of the optical bullet. In this polarization, the singularity is visualized in Figure 3.4 (b), and is common for azimuthally polarized beams. The presence of this structure results in the x and y components being rotated 90 degrees with respect to each other, see Figure 3.4 (c, d). The intensity structure of the azimuthally polarized optical bullet contains a number of concentric rings with clockwise and counterclockwise pace of the electric field rotation; see Figure 3.4 (b). Changes in the orientation of the azimuthally polarized light are caused by different phases on concentric rings when moving away from the center of the beam. As expected, the longitudinal component is absent in this case, see Figure 3.4 (e).

The next case, which we study, is the radially polarized optical bullet.

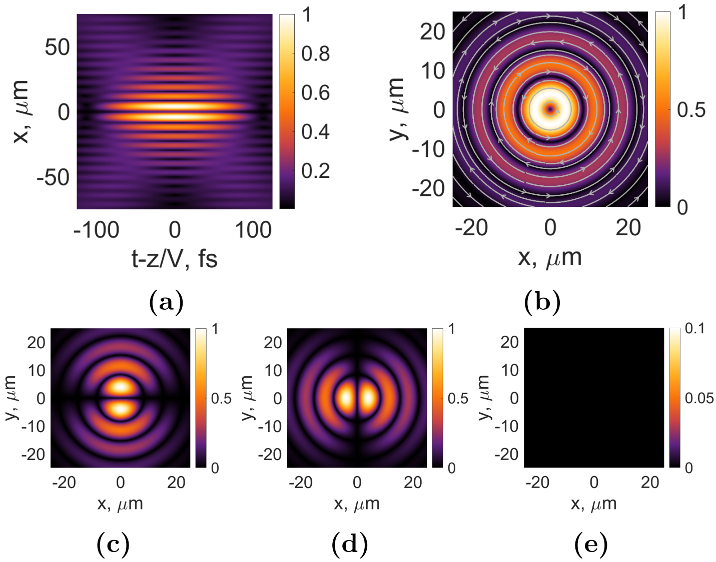

Figure 3.4: Intensity distributions of azimuthally polarized optical bullets and its individual components(E_x, (**c**), E_y, (**d**), E_z, (**e**)) in the transverse plane. The white arrows represent the orientation of the electric field. Frequency $\omega_c = 4\ fs^{-1}$. Topological charge $m = 0$, pulse duration $dt = 100\ fs$, $V/c = 0.63685$, $\gamma = -0.628\ \mu m^{-1}$.

We obtain individual electric field components using Equation (1.28) which we use to integrate Equation (1.26). For consistency, the set of parameters is the same in this integral as in previous cases.

The numerical results are given in Figure 3.5. The longitudinal intensity distribution of the radially polarized optical bullet largely resembles the previous case - we observe the presence of the onaxis intensity minima, though the intensity never reaches zero here, see Figure 3.5 (a). The intensity distribution in the transverse plane together with the depiction of the polarization state is given in Figure 3.5 (b). We observe here the presence of the polarization singularity: the electric field lines are not defined in the very center of the beam and are oriented either away or towards the center of the beam. Oscillations in the orientations are caused by phase changes in the concentric intensity structure of the radially polarized optical bullet. This behavior is well known and expected and is caused by the intensity distributions of the x and y components, see Figure 3.5 (c, d). The x component of the radially polarized optical pulse is rotated 90 degrees compared to the x

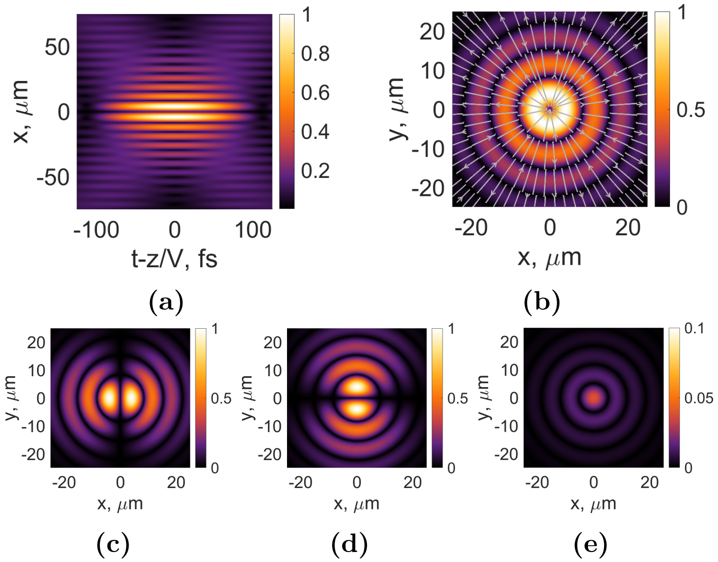

Figure 3.5: Intensity distributions of radially polarized optical bullets and its individual components(E_x, (**c**), E_y, (**d**), E_z, (**e**)) in the transverse plane. The white arrows represent the orientation of the electric field. Frequency $\omega_c = 4\ fs^{-1}$. Topological charge $m = 0$, pulse duration $dt = 100\ fs$, $V/c = 0.63685$, $\gamma = -0.628\ \mu m^{-1}$.

component of the azimuthally polarized pulse; see Figure 3.4 (c). The y component also rotates 90 degrees; see Figure 3.5 (d). Most notably, we observe the appearance of the longitudinally polarized z component; see Figure 3.5 (e). The presence of the nonzero z component causes the region of the on-axis polarization singularity to become somewhat less pronounced. As the maximum value of the z component reaches 10 % of the maximum intensity on the axis.

3.3. O- shaped optical bullets

Our next aim is to investigate the set of parameters for which the longitudinal shape of the optical bullet is expected to change from the capital Latin letter X to the capital Latin letter O. For ease of comparison, the dispersion curve, which we investigate, is the same as previously, see Figure 3.1 (b, curve (2)), but the central frequency has now decreased. This change will lead to larger spatial angles in the optical bullet, and thus we expect vectorial properties to become more pronounced.

We start the verification of this claim by repeating numerical simula-

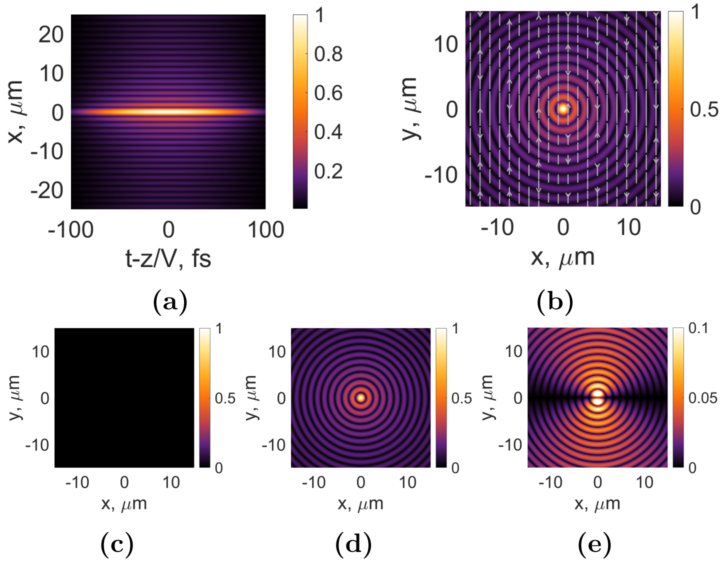

Figure 3.6: Intensity distributions of transverse electric (TE) linearly polarized optical bullets and its individual components(E_x, (**c**), E_y, (**d**), E_z, (**e**)) in the transverse plane. The white arrows represent the orientation of the electric field. The frequency $\omega_c = 1.6\ fs^{-1}$. Topological charge $m = 0$, pulse duration $dt = 100\ fs$, $V/c = 0.63685$, $\gamma = -0.628\ \mu m^{-1}$.

tions of the linearly polarized optical bullet using Equations (1.25, 1.26). The linearly polarized transverse electric optical bullet is presented in Figure 3.6. We immediately notice the changes in the longitudinal intensity distribution; see Figure 3.6 (a). Long-range peripheral arms similar to the X shape are no longer present, compared to Figure 3.2 (a). Although the spatial extent of the central part is smaller now and we observe a large number of needle-like structures when we move away from the center, we can deduce a rhombus-like area with approximately same levels of intensity; see Figure 3.6 (a). This becomes especially obvious when we turn our attention to the intensity levels of approximately 20 % of the normalized value. Although this rhombus shape has sharp corners, it can be seen as a distorted O-shape. Thus, we can conclude that the spatiotemporal shape of the vector optical bullet experiences the same changes as reported for scalar optical pulses [3, 31].

The transverse intensity distribution of the linearly polarized optical bullet is given for this case in Figure 3.6 (b). The electric field lines in this plane are expectedly oriented along the y direction. However, the intensity distribution of the total electric field has some signs of nonuniformity, with the tendency to have higher intensities in the direction of the electric field. In the expected manner for the transverse electric optical bullet, no x component is present, see Figure 3.6 (c). The dominant electric field component is the y component; see Figure 3.6 (d). When we plot the longitudinal electric field component, see Figure 3.6 (e), we recognize the cause of the nonuniformity in the total electric field. The maximum value of the z component reaches 10 % of the intensity of the y component. This increase in the relative strength of the longitudinal component is mainly caused by changes in the central frequency of the optical pulse, compared to Figure 3.2 (e).

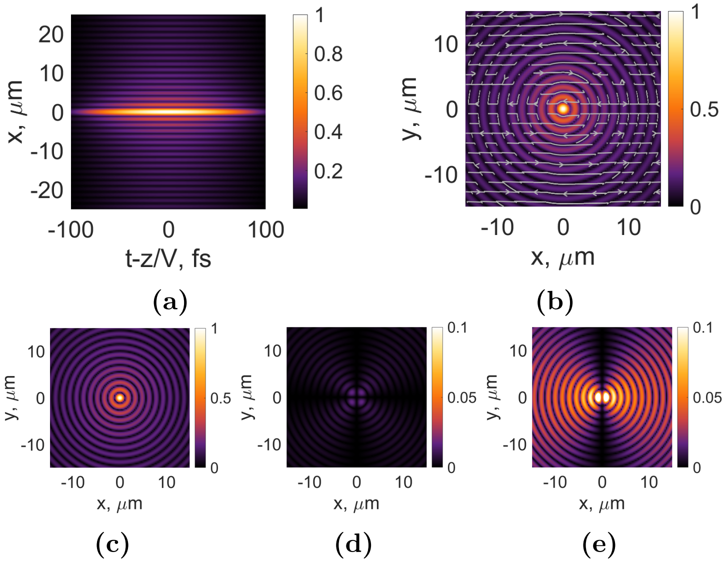

Figure 3.7: Intensity distributions of transverse magnetic (TM) linearly polarized optical bullets and its individual components(E_x, (**c**), E_y, (**d**), E_z, (**e**)) in the transverse plane. The white arrows represent the orientation of the electric field. The frequency $\omega_c = 1.6\ fs^{-1}$. Topological charge $m = 0$, pulse duration $dt = 100\ fs$, $V/c = 0.63685$, $\gamma = -0.628\ \mu m^{-1}$.

In the next set of simulations we move on to investigate the transverse magnetic linearly polarized optical bullet; see Figure 3.7. The longitudinal intensity distribution is given in Figure 3.7 (a). As in the case of the transverse electric optical bullet, in this case, we observe a disappearance of the pronounced X shape in the intensity profile, compared to Figure 3.3 (a). This behavior is expected because of the change in the central frequency of the optical pulse. The transverse intensity distribution is depicted in Figure 3.7 (b) together with the streamlines depicting the orientation of the electric field. We note the appearance of some inhomogeneity in the flow of the electric field, compared to Figure 3.6 (b). There are some particular points in the regions of vanishingly low intensity when the electric field is not oriented along the x-axis anymore. This behavior is expected when one notices the presence of the component y in the Equation (1.30).

The intensity distributions of the individual electric field components are given in Figure 3.7 (c-e). As expected, the x component of the electric field is the strongest; see Figure 3.7 (c). Most notably, we observe the appearance of a vanishingly small y component; see Figure 3.7 (d). Its maximum value reaches the single percent digits compared to the dominant x component. The longitudinal component reaches 10 % of the value of the x component. This behavior is comparable to the case of the transverse electric optical bullet; see Figure 3.6 (e).

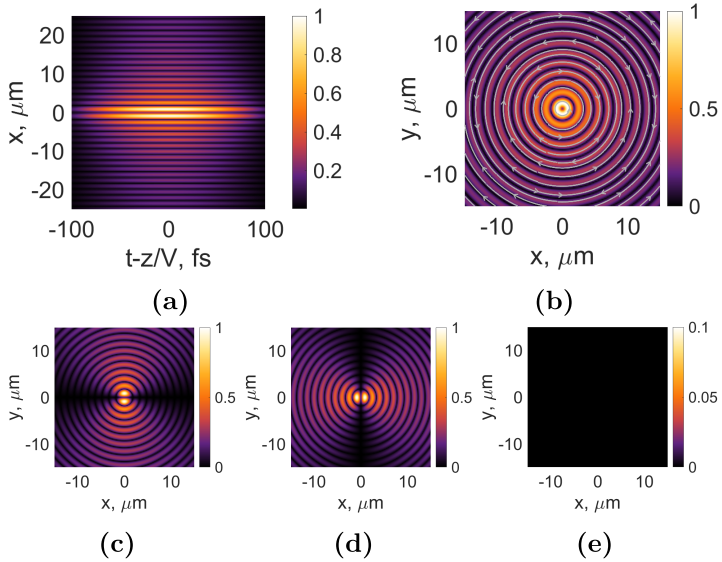

Figure 3.8: Intensity distributions of azimuthally polarized optical bullets and its individual components(E_x, (**c**), E_y, (**d**), E_z, (**e**)) in the transverse plane. The white arrows represent the orientation of the electric field. Frequency $\omega_c = 1.6\ fs^{-1}$. Topological charge $m = 0$, pulse duration $dt = 100\ fs$, $V/c = 0.63685$, $\gamma = -0.628\ \mu m^{-1}$.

We investigate radially and azimuthally polarized optical bullets of the O type using the same set of parameters as we did in the case of linearly polarized FWM. An example of the azimuthally polarized optical bullet for this particular case is given in Figure 3.8. The longitudinal intensity distribution is shown in Figure 3.8 (a). As expected, no z-component is present in the beam; see Equation (1.27), for this reason the optical pulse has a void-like intensity structure with no axial intensity. In particular, the general shape of the transverse intensity distribution is a distinct rhombus-like shape, resembling the capital Latin letter O, compared to Figure 3.4 (a). The transverse intensity distribution now represents a large number of concentric rings with oscillating direction of clockwise and counterclockwise electric field rotation; see Figure 3.8 (b). As the change in the central frequency has resulted in the increase of spatial angles of the individual Bessel beams, creating an optical bullet, the focus wave mode became more spatially confined, see Figure 3.8 (c, d). The individual electric field components are spatially oriented in the same way as in the previous case; see Figure 3.4 (c, d), but a finer structure with larger number of rings has appeared. As expected, no z components are present; see Figure 3.8 (e).

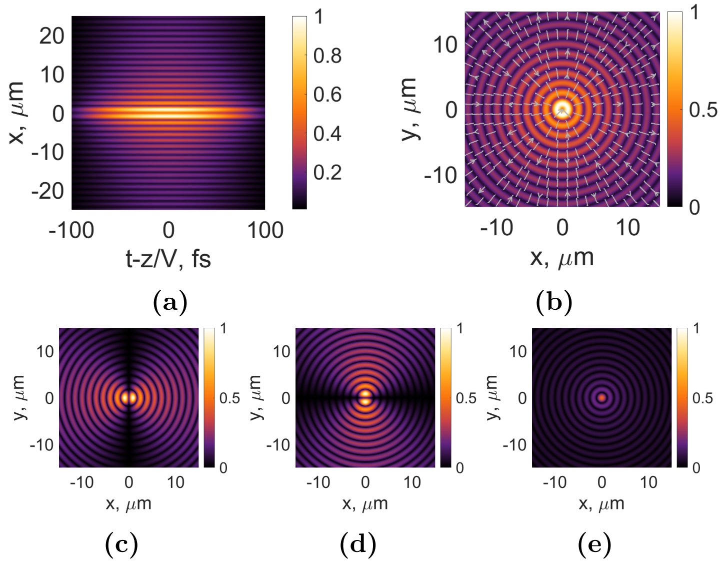

(a) **(b)**

(c) **(d)** **(e)**

Figure 3.9: Intensity distributions of radially polarized optical bullets and its individual components(E_x, (**c**), E_y, (**d**), E_z, (**e**)) in the transverse plane. The white arrows represent the orientation of the electric field. Frequency $\omega_c = 1.6\ fs^{-1}$. Topological charge $m = 0$, pulse duration $dt = 100\ fs$, $V/c = 0.63685$, $\gamma = -0.628\ \mu m^{-1}$.

The situation depicting the radially polarized optical bullet is given in Figure 3.9. The longitudinal intensity distribution, given in Figure 3.9 (a), resembles the intensity distribution of azimuthally polarized FWM; see Figure 3.8 (a), with a noticeable difference. The axial intensity is no longer zero and is on a level comparable to the general pattern of the beam. This can be especially noticed in the transverse intensity distribution of the electric field shown in Figure 3.9 (b). The central part of the beam is not hollow anymore, though we observe a polarization singularity with star-like flow of the electric field streamlines. Due to the phase jumps in the adjacent concentric rings, the orientation of the electric field is changing from inwards to outwards; see Figure 3.9 (b). The individual components of the electric field are shown in Figure 3.9 (c-e). As expected, the two strongest field components are the x and y components; see Figure 3.9 (c, d) and compared to the previous case, in Figure 3.5 (c, d). The longitudinal component became stronger, when compared to the previous case, please note the change in the colorbar values; see Figs. 3.5 (e) and 3.9 (e).

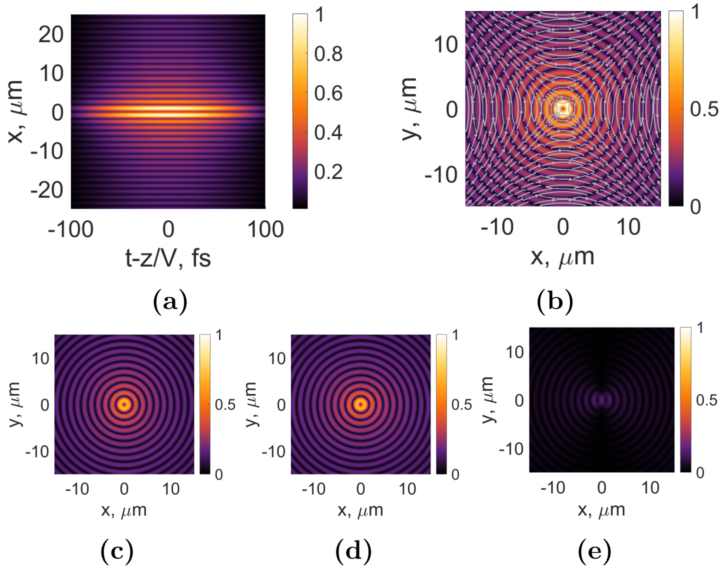

Figure 3.10: Intensity distributions of higher polarization order optical bullets and its individual components(E_x, (**c**), E_y, (**d**), E_z, (**e**)) in the transverse plane. The white arrows represent the orientation of the electric field. The frequency $\omega_c = 1.6\ fs^{-1}$. Topological charge $m = 1$, pulse duration $dt = 100\ fs$, $V/c = 0.63685$, $\gamma = -0.628\ \mu m^{-1}$.

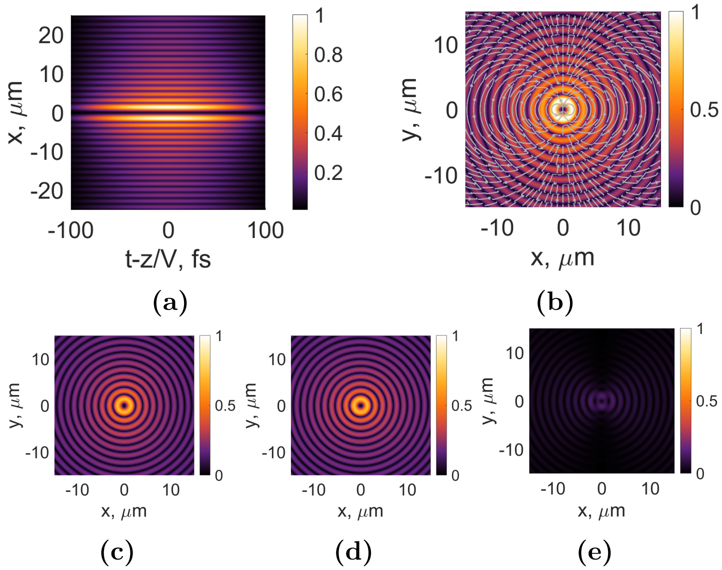

Figure 3.11: Intensity distributions of higher polarization order optical bullets and its individual components(E_x, (**c**), E_y, (**d**), E_z, (**e**)) in the transverse plane. The white arrows represent the orientation of the electric field. The frequency $\omega_c = 1.6\ fs^{-1}$. Topological charge $m = 2$, pulse duration $dt = 100\ fs$, $V/c = 0.63685$, $\gamma = -0.628\ \mu m^{-1}$.

We have also investigated cases of higher polarization order, with topological charge of $m = 1$ (translating to polarization order $p = 2$ [123]) in Figure 3.10 and $m = 2$ (translating to the polarization order $p = 3$ [123]) in Figure 3.11. We can see that in the case of Figure 3.10 there is a minimum intensity in the center of the beam, except for the z component, which has a considerable intensity in the center of the beam. The x and y components are exactly the same in intensity distributions. In Figure 3.11 we notice a total intensity zero in the center of the beam ($m = 2$). The distributions of the components x and y are exactly the same. There is an intensity minimum at the center of the z component, unlike in the previous case.

Lastly, we proceed with the investigation of very specific optical bullets with the spatial dispersion dependence depicted in Figure 3.1 (c). We recall here that these dependencies were obtained from Equation (1.22), when requiring that the longitudinal components of the wave vector k_z remain positive, i.e. describe the forward propagating conical beams, whereas the group velocity V of the optical bullet is negative, thus the result of the superposition of the forward propagating waves is a backward propagating optical pulse. For this study, we chose a particular set of parameters, see Figure 3.1 (c, curve (1)). We note that this specific condition requires rather large spatial angles of the individual components (up to $\pi/2$) and additionally restricts the temporal frequencies ω for which backward propagation of the pulse is possible. Thus, the description of the optical bullets using Equations (1.27) and (1.28) allows us to investigate optical bullets with high polarization orders p [123] or polarization singularities.

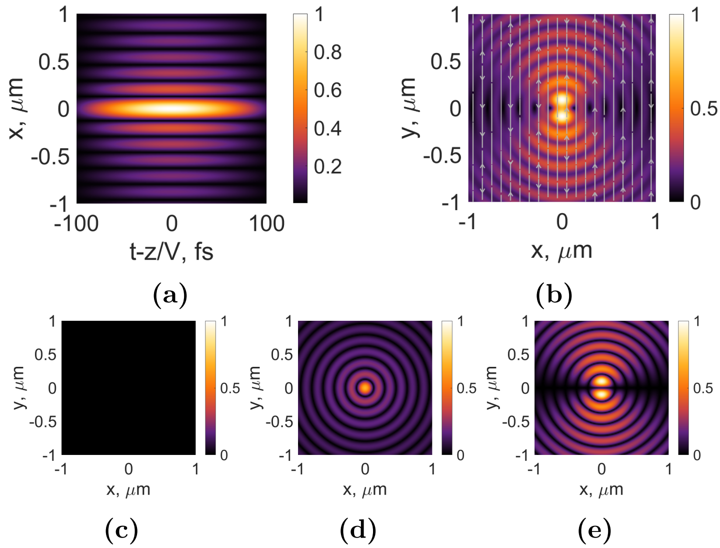

Figure 3.12: Intensity distributions of transverse electric (TE) linearly polarized optical bullets and its individual components(E_x, (**c**), E_y, (**d**), E_z, (**e**)). The white arrows represent the orientation of the electric field. Frequency $\omega_c = 4\ fs^{-1}$. Topological charge $m = 0$, $dt = 100\ fs$, $V/c = -1.2$, $\gamma = 6\pi\ \mu m^{-1}$.

Once again, we use Equation (1.29) to evaluate the linearly polarized transverse electric optical bullets, see Equation (1.25). The results of the numerical simulations are given in Figure 3.12. The longitudinal intensity distribution of the transverse electric optical bullet is given in Figure 3.12 (a). Note that because of the relatively high spatial angles, we had to decrease the transverse scale in all subsequent figures. The general shape of the optical bullet is of the O type. The area of approximately the same intensity level has a distinct rhombus-like shape. However, the most pronounced effect is observed in the transverse intensity distribution; see Figure 3.12 (b). The concentric ring-like structure that was observed in previous cases, see Figure 3.2 (b) and Figure 3.6 (b) is not present anymore. This change can be understood by looking at the intensity patterns of individual electric field components; see Figure 3.12 (c-e). No x component is present, but the longitudinal component of the field is the strongest due to the high spatial angles of the individual plane waves; see Figure 3.1 (c).

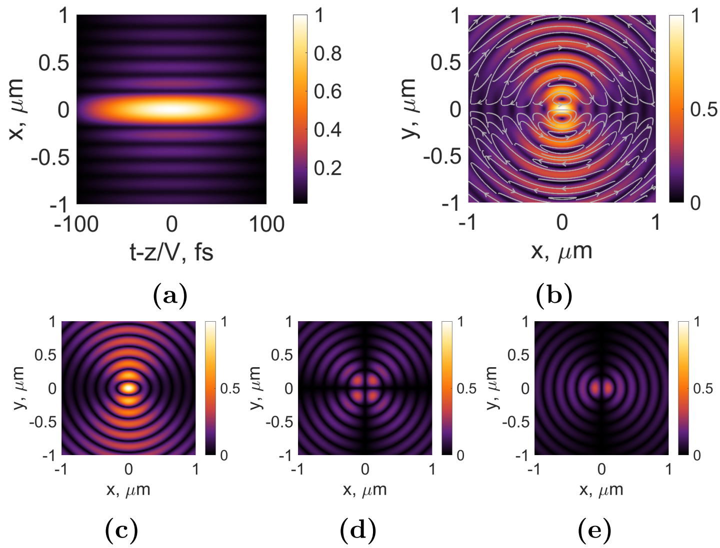

Figure 3.13: Intensity distributions of transverse magnetic (TM) linearly polarized optical bullets and its individual components(E_x, (**c**), E_y, (**d**), E_z, (**e**)). The white arrows represent the orientation of the electric field. Frequency $\omega_c = 4\ fs^{-1}$. Topological charge $m = 0$, $dt = 100\ fs$, $V/c = -1.2$, $\gamma = 6\pi\ \mu m^{-1}$.

The linearly polarized transverse magnetic optical bullet for this particular case is evaluated and presented in Figure 3.13. The most noticeable difference for the backward propagating TM mode compared to the TE mode can be seen in Figure 3.13 (a). The transverse beam size is considerably larger in this case, but the longitudinal dimension is the same. The changes are even more pronounced in the transverse pattern of the optical bullet at its center; see Figure 3.13 (b). The streamlines representing the electric field are not oriented along the x-axis anymore, compared to the previous cases, see Figs. 3.3 (b) and 3.7 (b). The intensity distribution is not symmetrical anymore with respect to the beam center but is elongated along the x-axis. This behavior is a direct manifestation of high spatial frequencies comprising the backward-propagating FWHM. In a similar fashion, linearly polarized light is elongated along the direction of polarization in high numerical aperture systems. Moreover, from the flow of the electric field lines, we conclude that the notable cross-polarized component is present, see Figure 3.13 (b). The individual components of the electric field are given in Figure 3.13 (c-e). The x-polarized component is no longer symmetric, though the concentric rings system is observable in the beam profile. For this particular case, we observe the strongest cross-polarized y component from all the considered cases; see Figure 3.13 (d). Its maximum value is even comparable to that longitudinally polarized in Figure 3.13 (e). The general shapes of these individual components are in line with expectations. We see that the longitudinal component is elongated along the direction of polarization and that the cross-polarized component has two perpendicular splits in its concentric ring pattern.

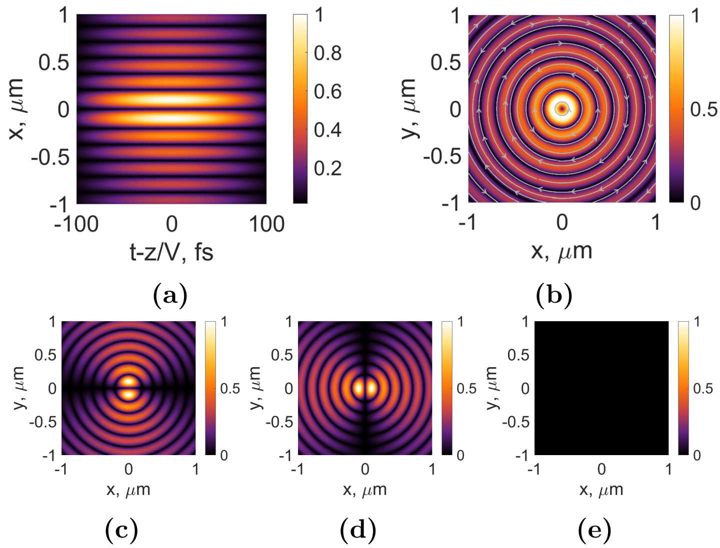

Figure 3.14: Intensity distributions of azimuthally polarized optical bullets and its individual components (E_x, (**c**), E_y, (**d**), E_z, (**e**)). The white arrows represent the orientation of the electric field. Frequency $\omega_c = 4\ fs^{-1}$. Topological charge $m = 0$, $dt = 100\ fs$, $V/c = -1.2$, $\gamma = 6\pi\ \mu m^{-1}$.

We consider the inhomogeneously polarized backwards propagating optical bullets with the case of azimuthal polarization; see Figure 3.14. The longitudinal intensity distribution is given in Figure 3.14 (a). Compared to previously investigated cases, the most distinct effect caused by spatiotemporal dispersion is the change of the transverse sizes and observation of the general shape of O-type; see Figure 3.14 (a). In the transverse plane, we see a large number of concentric rings with clockwise and counterclockwise directions of the electric field flow; see Figure 3.14 (b).

The longitudinal field component for azimuthal polarization is zero, and the x and y components are of the same strength, and intensity distributions with one notable difference being a 90 degree rotation with respect to each other; see Figure 3.14 (c-e).

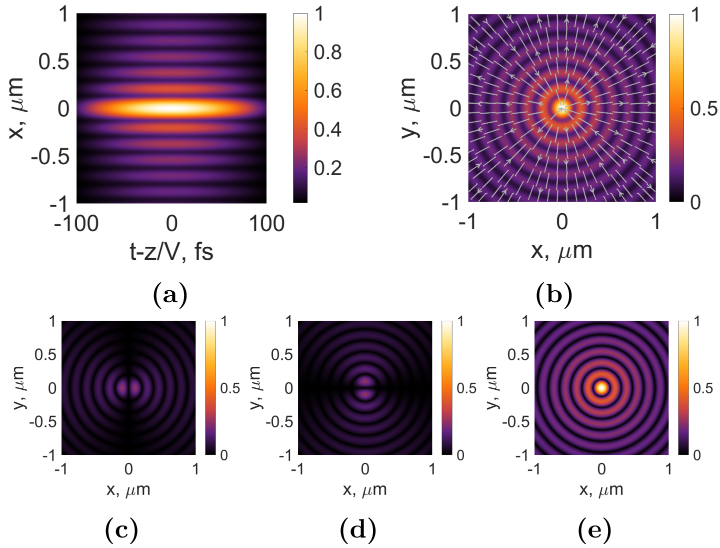

Figure 3.15: Intensity distributions of radially polarized optical bullets and its individual components (E_x, (**c**), E_y, (**d**), E_z, (**e**)). The white arrows represent the orientation of the electric field. Frequency $\omega_c = 4\ fs^{-1}$. Topological charge $m = 0$, $dt = 100\ fs$, $V/c = -1.2$, $\gamma = 6\pi\ \mu m^{-1}$.

The radially polarized backward-propagating optical bullet is depicted in Figure 3.15. Here, we observe a distinct difference from the azimuthally polarized optical bullet and compare Figure 3.14 (a) and Figure 3.15 (a). Whereas the central part of the azimuthally polarized optical bullet is hollow because of the presence of azimuthal phase singularity, the central part of the radially polarized optical bullet is the brightest one. The transverse intensity distribution depicts the same trend - the central part still contains the star-like radial polarization singularity, but the intensity is still highest at its very core; see Figure 3.15 (b). The solution to this riddle is presented in Figure 3.15 (c-e), where the individual electric field components of the optical pulse are given. The components x and y are comparable to each other and rotated by 90 degrees in respect to one another; see Figure 3.15 (c, d). However, opposite to the previous cases, the strongest electric field component is the longitudinal one; see Figure 3.15 (e). This behavior is expected due to the choice of the central frequency in the optical pulse, causing the appearance of high spatial angles θ. Under these conditions, the radial polarization becomes strongly focused, which in return causes the appearance of very tight small spots with longitudinal polarization [38].

We summarize the investigation of these three particular cases by investigating the effects that the choice of group velocities V and the propagation constant γ has on the spatiotemporal parameters of the optical bullets, such as effective beam width in transverse and longitudinal directions. In the case of uniform beam shapes, such as a Gaussian beam or similar modes, the question of the beam width definition is pretty straightforward. The full width at half maximum of the intensity is the most commonly used within the field. However, in our case, the complex vectorial nature together with a rich ring-like structure observed in the variously polarized pulses suggests to look at alternative definitions for the beam width. One of the alternatives that is very efficient at accounting for peripheral parts of the complex optical beams is the so-called second-moment definition.

$$w_{int} = \left(\frac{\int_{-\infty}^{\infty} \rho^2 I(\rho) d\rho}{\int_{-\infty}^{\infty} I(\rho) d\rho} \right)^{1/2} \tag{3.2}$$

where ρ is the radial coordinate in the plane under consideration and $I(\rho)$ is the total intensity of the electric field.

3.4. Beam widths

As we have concluded from three cases investigated in the previous part, the spatiotemporal dependence between frequencies, individual cone angles (see Figure 3.1) strongly affects intensity distributions both of individual electric field components and total electric field for vector optical bullets. Therefore, it is natural to ask ourselves whether these effects can be qualified using standard metrics, such as beam length. In this numerical experiment, we keep the same duration ($dt = 100fs$) for all cases and change the central frequency ω_c of the pulse. We consider linearly polarized TE and TM optical bullets along with radially and azimuthally polarized ones. The transverse beam width is evaluated together with the longitudinal extent of the optical pulse using two different definitions: FWHM and second moment.

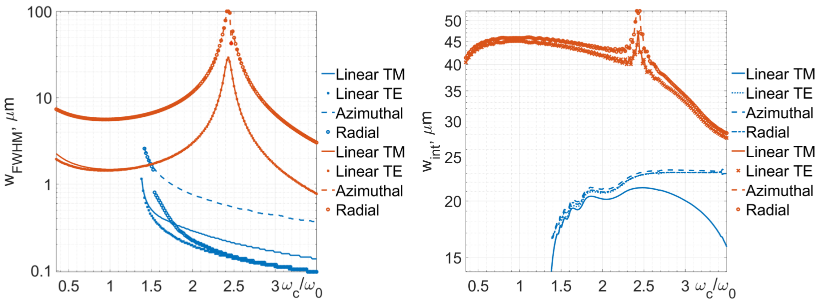

(a) **(b)**

Figure 3.16: Dependencies of FWHM (a) and second-moment (b) pulsed beam widths in BK7 glass for different values of frequency ω_c for linear, azimuthal and radial polarizations. The red color represents $V/c = 0.63685$ $\gamma = -0.628$ μm^{-1}, and the blue color $V/c = -1.2$ $\gamma = 6\pi$ μm^{-1}. Topological charge $m = 0$, $dt = 100$ fs.

The beam widths of the optical pulses using the FWHM definition are given in Figure 3.16 (a). First, we note that for particular parameters $V/c = 0.63685$ and $\gamma = -0.628$ μm^{-1} the FWHM beam width behaves very distinctly: the beam width first decreases, up to central frequencies of $\omega_c/\omega_0 \approx 1$, then increases to the maximum value of 100 μm at frequency $\omega_c/\omega_0 \approx 2.4$. A further increase in the carrier frequency ω_c results in a monotonically decreasing beam size. This behavior can be understood by looking at Figure 3.1 (b, curve (2)). The spike in FWHM dependency occurs at the same frequency when the spatial angles are rather small. When the spatial angles increase, we obtain optical pulses with small transverse sizes. Most notably, the linearly polarized modes have, for this case, indistinguishable beam width; see Figure 3.16 (a, red curves). The same applies to the radially and azimuthally polarized beams, though they are larger than the linearly polarized optical bullets.

For this particular case, the spatial angles θ are rather modest, so the difference between the azimuthal and radial polarizations is vanishingly small, as is the case between the linearly polarized TM and TE optical bullets.

We also investigate the beam sizes of the backward propagating focus wave modes, where $V/c = -1.2$ and $\gamma = 6\pi\ \mu m^{-1}$, see Figure 3.16 (a, blue curves). In our previous investigation, we observed the most notable differences between polarizations in this case. As a result, we observe that the FWHM beam-width dependencies are separate for all different cases of vector FWMs. Most notably, the radial polarization becomes comparable in the beam sizes to the linearly polarized TE FWM, as the frequency increases. This is an expected outcome because it is well known that radial polarization could even result in a tighter focal spot than linear polarization [38]. Radial polarization has beam sizes smaller than those of the linearly polarized TM mode; see Figure 3.16 (a). The largest beam sizes are observed for the azimuthally polarized FWM.

The next metric is the definition of the second moment of the beam width. This metric usually has the characteristic of artificially increasing importance of peripheral parts of the beam. It represents the radial distance weighted intensity; therefore, if the intensity drops moving away from the center of the beam slower than the square of the radial distance, it might result in larger beam sizes than those obtained using the FWHM definition. The result of the numerical estimate of this beam width for the same set of parameters is given in Figure 3.16 (b). We immediately notice differences in the general trend of the beam-width dependencies of the carrier frequency. Whereas the FWHM beam width was monotonically decreasing for four cases out of eight, the second-moment beam width depends on the carrier frequency non-monotonically. For small carrier frequencies, it starts to increase to some particular value and then drops. In this case, the linear polarization has the largest beam width. These subtle differences that occur at smaller carrier frequencies ω_c are observable for the four cases considered here. Moving to the case of backward propagating FWM, see Figure 3.16 (b, blue curves), we note yet another tendency: the beam widths defined using the second order moment of the beam behave differently than those defined using the FWHM definition; compare to Figure 3.16 (a). This means that even though the beam is above the 50 percent level is larger, the total intensity in the beam drops a lot faster than the radial coordinate for smaller carrier frequencies. The fact that the second-moment beamwidth increases with increasing central frequency indicates that significant side lobes become present in the vector FWMs.

The longitudinal beam size has also been investigated. The result did not show any change in that size across all investigated frequencies, and for the sake of brevity, figures covering this claim are not provided. In the case of $V/c = 0.63685$ and $\gamma = -0.628\ \mu m^{-1}$, the longitudinal beam size remains constant at 26.01 μm using the FWHM definition for all polarizations investigated. For the case of $V/c = -1.2$ and $\gamma = 6\pi\ \mu m^{-1}$, the longitudinal beam size remains constant at 49.05 μm for all the investigated scenarios. Using the definition of second-moment beam size, we have determined the following constant longitudinal beam lengths: 44.35 μm for $V/c = 0.63685$ and $\gamma = -0.628\ \mu m^{-1}$, and 47.24 μm for $V/c = -1.2$ and $\gamma = 6\pi\ \mu m^{-1}$.

3.5. Individual components

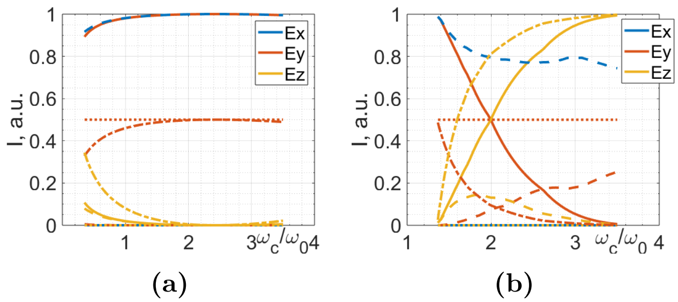

Figure 3.17: Normalized intensities of individual components of FWM pulses (E_x - blue, E_y - red, E_z - green). Topological charge $m = 0$, pulse duration $dt = 100\ fs$. For the cases: (a) $V/c = 0.63685$, $\gamma = -0.628\ \mu m^{-1}$, (b) $V/c = -1.2$, $\gamma = 6\pi\ \mu m^{-1}$. The solid line represents the linear polarization of TE, the dashed line represents the linear polarization of TM, the dotted line represents the azimuthal polarization, and the dashed-dotted line represents the radial polarization.

Another key point of interest in this investigation is the relative strengths of the intensity of individual electric field components for different frequencies. In Figure 3.17 (a), we give the dependencies for $V/c = 0.63685$ and $\gamma = -0.628\ \mu m^{-1}$. The solid lines represent the linear TE polarization and the dashed line represents the linear TM polarization. For linear polarization, with lower frequency values, we can see that the z component has an intensity of up to 10%. With increasing frequency, the z component of the electric field decreases and, around the value of $\omega_c/\omega_0 \approx 1$, the z component approaches 0. For the TE polarization, the y component is nonexistent; for the TM polarization, the x component is nonexistent. The azimuthal polarization has constant x- and y-components of equal proportions at all frequencies tested, without a z component of the electric field. Radial polarization has the z component for low frequencies, which decreases rapidly with increasing frequency, see Figure 3.17 (a).

In the case where the vector FWM propagates backwards, that is, $V/c = -1.2$ and $\gamma = 6\pi\ \mu m^{-1}$, the dependencies of the normalized intensities of the individual components are more pronounced, see Figure 3.17 (b). The linear TE optical bullet and radially polarized FWM have strong z-components of the electric fields that increase with increasing frequency. On the other hand, the linear TM polarization has a strong x component of the electric field, but with increasing frequency, the maximal intensities of the y and z electric field components start to dominate, see Figure 3.17 (b). From the frequencies of $\omega_c/\omega_0 \approx 1.8$, the intensity of the z component of the electric field slowly decreases, resulting in the increase of the y component. The azimuthally polarized FWM shows steady and equally strong x and y components at all tested frequencies, as expected. The radially polarized FWM has the strongest z electric field component, which increases rapidly with increasing frequency, see Figure 3.17 (b).

3.6. Summary of the results

We have introduced the vector formalism to the concept of nondiffracting and nondispersing optical bullets within a dielectric material. Vector optical bullets for different polarizations were introduced: linear polarization, azimuthal polarization, and radial polarization. Two different propagation velocities V were chosen to showcase the wide variety of spatiotemporal dispersions of vector optical bullets, one positive and one negative (i.e. backward propagating). The first value of the group velocity V was chosen because it enforces a particularly interesting dispersion, with cone angles that extend from small paraxial (i.e. scalar description is valid) to larger values, which require now a proper vector treatment of the electric field.

For this particular velocity, we selected two different values of central frequencies, showcasing two possible situations: one giving the so-called X spatiotemporal profile and another giving the so-called O spatiotemporal profile. We can conclude that the spatiotemporal shape of the vector optical bullet experiences the same changes as reported for scalar optical pulses with differences arising from nonzero longitudinal and cross-polarization components. In the expected manner, high cone angles result in a vector description of the vector FWM, also demonstrating distinct differences between polarizations.

For the second case, when the forward propagating superposition of Bessel beams creates within the Bessel zone a backward propagating pulse of negative velocity V, we observed the most notable differences in the properties of vector optical bullets within the dielectric material. Due to the highly nonparaxial nature of such exotic waves, the longitudinal component is quite noticeable in the TE and TM polarized optical bullets, most notable is the appearance of relatively large cross-polarized component in the linearly polarized TM mode. As expected no differences did appear in the azimuthally polarized optical bullet, but the radially polarized wave was most affected - the longitudinal electric field component dominates the intensity pattern.

Lastly, we have studied how polarization and spatio-temporal dispersion influence the beam size of the optical bullets in the focal plane. For this we have used two distinct metrics - the full width half maximum and the second-order moment of the beam. As expected, the FWHM beam size gradually increases, where the central frequency and the group velocity allow the angular dispersion curve to touch the frequency axis. This has been shown using two different methods to calculate the beam size: the full width at half maximum and the method of the second moment. For the optical bullets with negative group velocity the FWHM beam sizes monotonically increase as we move along the dispersion curve to higher cone angles of the spatial components. The second metric is well known for its sensitivity to the side lobe energy, so this parameter has revealed a complex dynamics within the optical bullets showcasing a competition between the main spike of the signal and the side lobes.

We also investigated the normalized maximal intensities of each component for the linear, radial, and azimuthal polarizations of the TE and TM for the negative and positive group velocity values. The behaviors are found to be very different for these aforementioned cases. The most notable difference was caused by rather high spatial angles in the backwards propagating optical bullets, as we investigate various carrier frequencies.

4. LOCALIZED VECTOR OPTICAL NONDIFFRACTING SUBCYCLE PULSES

4.1. Vector optical bullets

Nondiffracting and nondispersive pulsed beams are typically introduced within a cylindrical symmetry, where they are understood as a coherent superposition of monochromatic solutions of the cylindrical coordinate framework. These results have been published in my article [129]. To achieve nondiffracting and nondispersive characteristics, the wave vectors k and frequencies ω within the pulsed beam must be related. This condition leads to a variety of pulsed beams that resist both diffraction and dispersion. The scalar focus wave modes are well known, and here we construct their vector counterparts. Vectorial solutions of the Maxwell equations are constructed from solutions of scalar wave equations using the method given in References [56, 57], and defined previously in Equations (1.22 - 1.30). For the integration of Equations (1.26) and (1.27) we use the Matlab 2023a procedure 'quadgk', with both relative and absolute tolerances set to 10^{-8}.

4.2. Vector subcycle pulses

Subcycle duration pulses are common nowadays [130]; however, the main question of this study is whether the subcycle duration can be combined with the nondiffracting and nondispersing properties of the focus wave modes described by Equation (1.22).

In this study, we introduce the rectangular spectral envelope $S(\omega) = \Pi(\omega_c - \omega/\Delta\omega)$, where

$$\Pi\left(\frac{\omega}{\Delta\omega}\right) = \begin{cases} 0, & \text{if } |\omega| > \frac{\Delta\omega}{2}, \\ \frac{1}{2}, & \text{if } |\omega| = \frac{\Delta\omega}{2}, \\ 1, & \text{if } |\omega| < \frac{\Delta\omega}{2}, \end{cases} \tag{4.1}$$

and where $\Delta\omega$ is the spectral width of the rectangular spectral envelope, and ω_c is the central frequency of the wave packet. For the rectangular spectral envelope, the spectral width $d\omega$ can be related to the temporal duration dt using the expression $d\omega = 5.56/dt$ [128].

To quantify the resulting pulses as the subcycle we introduce the following parameter:

$$\frac{\Delta\omega}{\omega_c} = \frac{T_c}{\Delta t},$$
$$\lim_{\Delta\omega\to\infty} \frac{\Delta\omega}{\omega_c} \to 2,$$
$$\lim_{\Delta\omega\to\infty} \frac{\Delta t}{T_c} \to \frac{1}{2}, \tag{4.2}$$

where T_c is the cycle duration of the central frequency ω_c. Obviously, the limit of the shortest pulse is half the cycle of the central frequency, leading to the spectral width being twice the frequency. We now combine the spatiotemporal dispersion of the optical bullets with this definition and investigate the dependency of the parameter $\Delta\omega/\omega_c$ on the group velocity V/c and the parameter γ. The results are depicted in Figure 4.1 (a) for vacuum conditions.

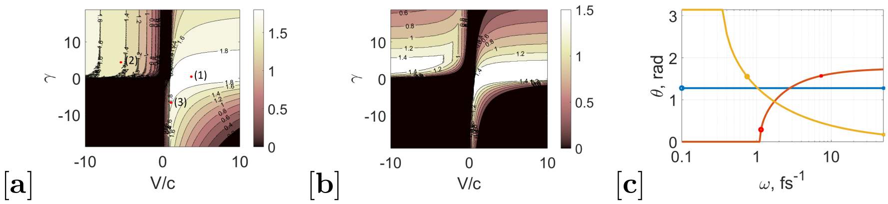

Figure 4.1: (**a**) Dependency of the parameter $\Delta\omega/\omega_c$ for focus wave modes on the parameters γ and V/c in vacuum; (**b**) dependency of the parameter $\Delta\omega/\omega_c$ for focus wave modes on the parameters γ and V/c in BK7 glass. (**c**) Angular dispersion curves of focus wave modes in vacuum for parameters: (**1**) blue curve $V/c = 3.45, \gamma = 0$ μm^{-1}; (**2**) red curve $V/c = -5.65, \gamma = 4.35$ μm^{-1}; (**3**) orange curve $V/c = 1, \gamma = -2.45$ μm^{-1}.

In general, it was observed that values of $\Delta\omega/\omega_c$ are very close to 2. Most strikingly, it is possible to create subcycle optical bullets that propagate backward. On the other hand, for positive group velocities, the spatiotemporal dispersion restricts the shortest possible duration of the nondiffracting pulsed beam; see Figure 4.1 (a).

Here we note that the duration of the subcycle optical bullet in a dispersive medium is larger than in vacuum; see Figure 4.1 (b). The cause of this is the presence of absorption lines which restrict the resulting bandwidth, showing Equation (1.22) is valid in those regions.

In further numerical simulations three distinct examples of spatiotemporal dispersion have been selected; see Figure 4.1 (c) and numerically integrate Equations (1.26) and (1.27) using the expression mentioned above for the spectral envelope.

We start our investigation by selecting point (**1**) from Figure 4.1 (a). Here, the group velocity of the focus wave mode is $V/c = 3.45$ and the parameter $\gamma = 0\ \mu\text{m}^{-1}$, which is a particular case that is referred to as X-waves in the literature. We investigated the following four polarization cases: linear TE (transverse electric), linear TM (transverse magnetic), radial, and azimuthal polarizations; see Equations (1.26) and (1.27).

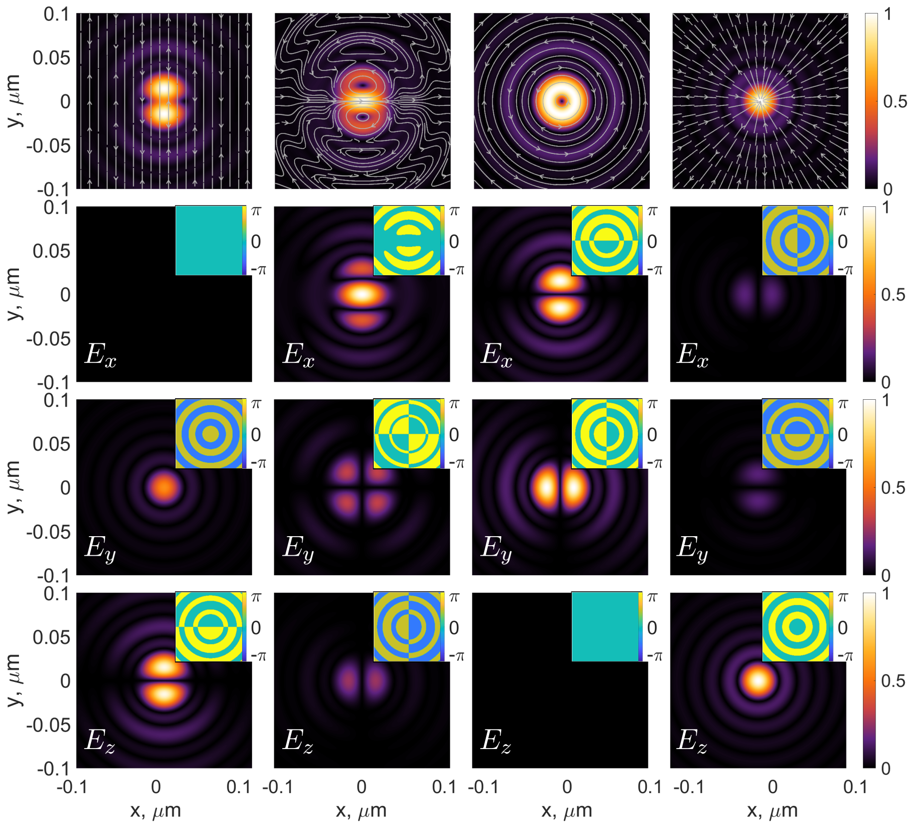

Figure 4.2: Intensity distributions of subcycle pulses in vacuum and their individual components E_x (second row), E_y (third row), E_z (fourth row) in the transverse plane for linear TE (first column), TM (second column), azimuthal (third column), and radial (fourth column) polarizations when $V/c = 3.45, \gamma = 0\ \mu\text{m}^{-1}$. The white arrows in first row represent the orientation of the electric field. The insets represent the phase distributions of the individual components.

First we plotted the intensity distributions of these subcycle pulsed beams in the transverse plane; see Figure 4.2, first row. The linearly polarized TE mode is elongated along the polarization direction, as expected from the literature, and this occurs due to the strong longitudinal component; see Figure 4.2, last row. In addition, we present the individual components of the pulsed beam together with their phases, which resemble the behavior of the tightly focused, linearly polarized, monochromatic beam [43]. However, the linearly polarized TM mode does not follow this trend, as it occupies a larger area in the direction perpendicular to the polarization, though the central spike is elongated along the direction of the polarization. A careful look at the individual components reveals the cause of that. The x component is no longer symmetric and has two additional spikes further away from the central part; see Figure 4.2, second column. Moreover, besides the appearance of the z component, we observe a cross-polarized non-zero y component. Individual spikes in the x components have the same phases; see the corresponding inset in Figure 4.2, while the remaining two individual components have spikes with alternating phases. The FWHM sizes are $\Delta x_{TE} = 0.0332$ µm, $\Delta y_{TE} = 0.0533$ µm, and $\Delta x_{TM} = 0.0392$ µm, $\Delta y_{TM} = 0.0211$ µm in the transverse plane.

An azimuthally polarized subcycle X-wave behaves in an expected manner—it has only two transverse components, see Figure 4.2, third column. However, the radially polarized X-wave demonstrates a rather interesting feature in the subcycle mode—its z component is the strongest due to rather tight focusing conditions; see Figure 4.2, last column. The FWHM sizes are $\Delta x_{azi} = 0.0533$ µm, $\Delta y_{azi} = 0.0533$ µm and $\Delta x_{rad} = 0.0392$ µm, $\Delta y_{rad} = 0.0271$ µm in the transverse plane.

After analyzing the spatial structure of the vector X-waves for this particular case in the transverse plane, we examined their behavior in the longitudinal plane, where the temporal duration influenced the longitudinal shape of the vector pulsed beams; see Figure 4.3. This figure shows the total and individual intensity distributions in a specific longitudinal plane. First, we noted the distinct difference in the shape of the linearly polarized TE and TM optical bullets; see Figure 4.3. The cross-shaped peripheral part is more pronounced for the TE mode; compare the first and second columns. For the TM polarization, the profile is less pronounced, but the overall shape looks smoother. The most

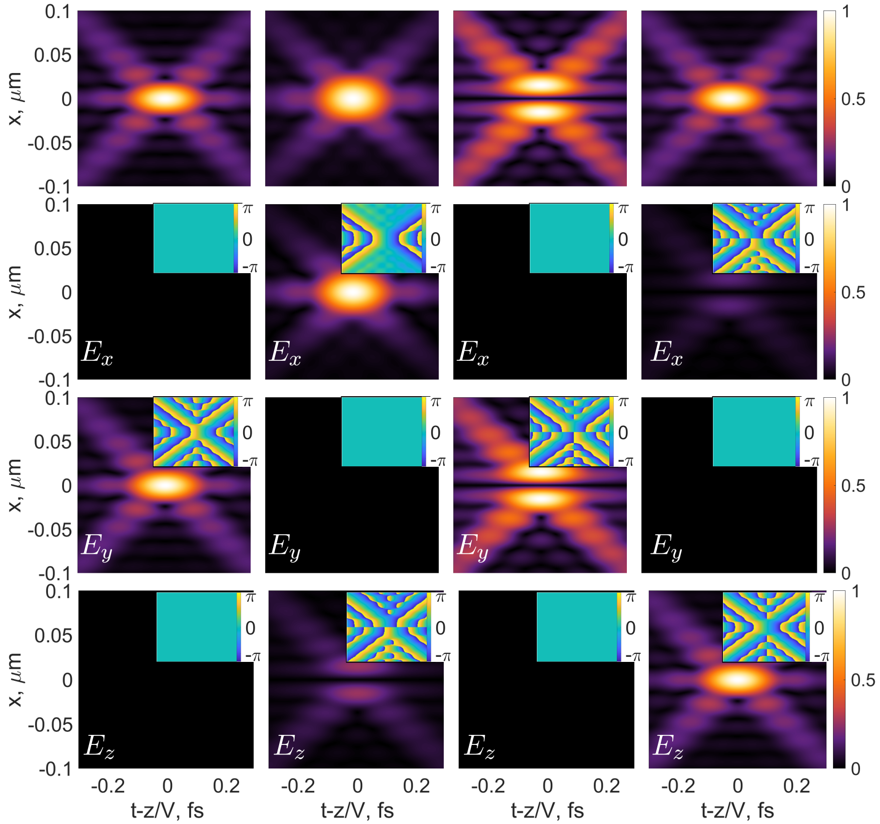

Figure 4.3: Intensity distributions of subcycle pulses in vacuum and their individual components (E_x (second row), E_y (third row), E_z (fourth row)) in the longitudinal plane for linear TE (first column), TM (second column), azimuthal (third column), and radial (fourth column) polarizations when $V/c = 3.45, \gamma = 0\ \mu\text{m}^{-1}$. The insets represent the phase distribution for each individual component.

important thing is the appearance of axial secondary maxima before and after the central part, giving the intensity profile the resemblance of a rotated Cyrillic letter 'Ж'. Due to the choice of the longitudinal plane, the TE mode has a single non-zero component. The phase of the component reveals that the structure of the wave front had a conical nature. The phase gradient is related to the direction of the energy flow. This can be seen from the phase distribution in the figures, which contains moving parts inward and outward, as previously observed in the literature [58, 131]. The situation is similar in the case of linear TM polarization, though it has two electric field components in this particular longitudinal plane, the x and z components. The intensity profile of the x component is identical to that of a rotated Cyrillic letter 'ж'. However, the z component still resembles a general X-shape with an axial void due to the zero line. The phase distributions are typical for that type of conical beam, and the energy flow for each component is as expected. The FWHM sizes are $\Delta z_{TE} = 0.1899$ fs and $\Delta z_{TM} = 0.1899$ fs in longitudinal directions.

Moving on to the cases of azimuthal and radial polarizations, the third and fourth columns in Figure 4.3, we draw attention to the very pronounced peripheral part of the beam for the azimuthal polarization. Only a single component is present for this pulsed beam in this particular plane. The phase distribution shows the conical energy flow with a phase jump on the z axis due to the polarization singularity on the axis [38, 39]. The radially polarized mode has a dominant z component and a weaker x component with the characteristic shape of the letter X. The FWHM sizes are $\Delta z_{azi} = 0.2261$ fs, and $\Delta z_{rad} = 0.1899$ fs in longitudinal directions.

Now we consider point (**2**) in Figure 4.1 (a). Here, the group velocity of the focus wave mode is $V/c = -5.65$, and the parameter $\gamma = 4.35$ μm^{-1}. This case is notable because the superposition of forward-propagating waves results in a negative group velocity, causing the optical bullet to propagate backwards. Here, we investigate the same four polarization cases: linear TE (transverse electric), linear TM (transverse magnetic), radial, and azimuthal polarizations; see Equations (1.26) and (1.27).

We plotted intensity distributions of these subcycle pulsed beams in the transverse plane; see Figure 4.4, first row. The linearly polarized TE mode is elongated along the polarization direction, as expected from the literature, and this occurs due to the strong dominant longitudinal component; see Figure 4.4, last row. We present individual components of the pulsed beam together with their phases, which resemble the behavior of the tightly focused ,linearly polarized, monochromatic beam [43]. However, the linearly polarized TM mode once again does not follow this trend, as it occupies a larger area in the direction perpendicular to the polarization, although the central spike is elongated along the direction of the polarization. A careful look at the individual components reveals the cause of that. The x component is not symmetrical anymore and

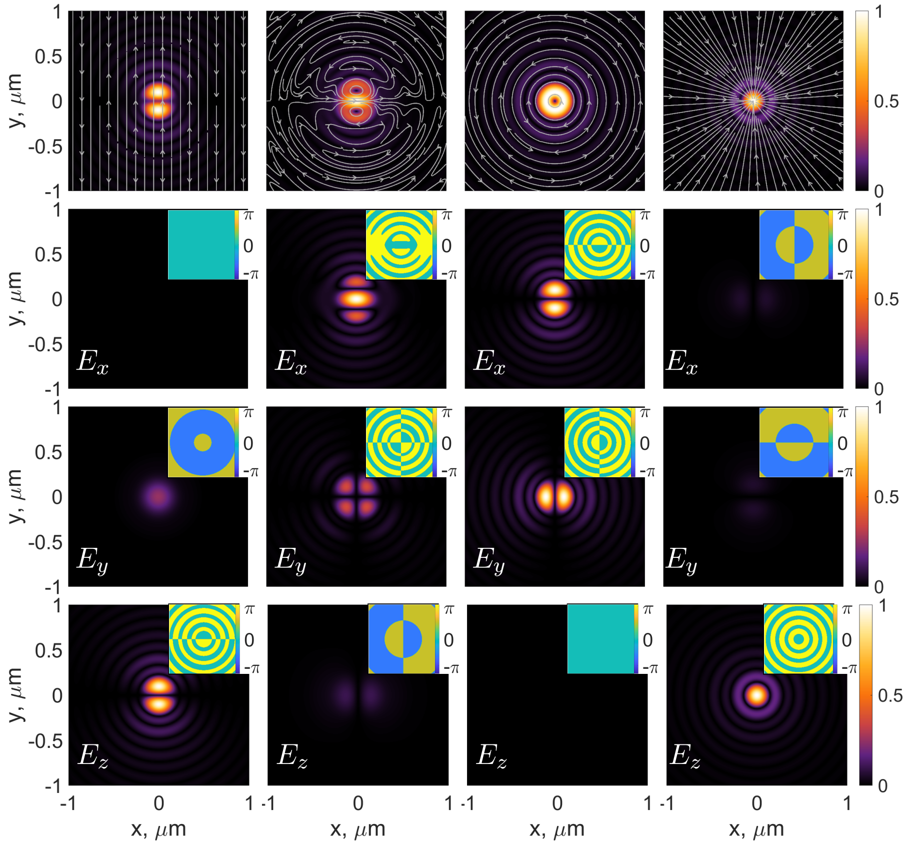

Figure 4.4: Intensity distributions of subcycle pulses in vacuum and their individual components E_x (second row), E_y (third row), E_z (fourth row) in the transverse plane for linear TE (first column), TM (second column), azimuthal (third column), and radial (fourth column) polarizations when $V/c = -5.65, \gamma = 4.35$ µm^{-1}. The white arrows in first row represent the orientation of the electric field. The insets represent the phase distribution.

has two additional spikes further away from the central part; see Figure 4.4, second column. Moreover, besides the appearance of the z component, we observe a non-zero cross-polarized y component. Individual spikes in the x components have the same phases, while the remaining two individual components have spikes with alternating phases; see the corresponding inset in Figure 4.4. The z component is weakest in this case compared to all the polarizations we consider here. The FWHM sizes are $\Delta x_{TE} = 0.2312$ µm, $\Delta y_{TE} = 0.3518$ µm, and $\Delta x_{TM} = 0.2714$ µm, $\Delta y_{TM} = 0.1307$ µm in transverse directions.

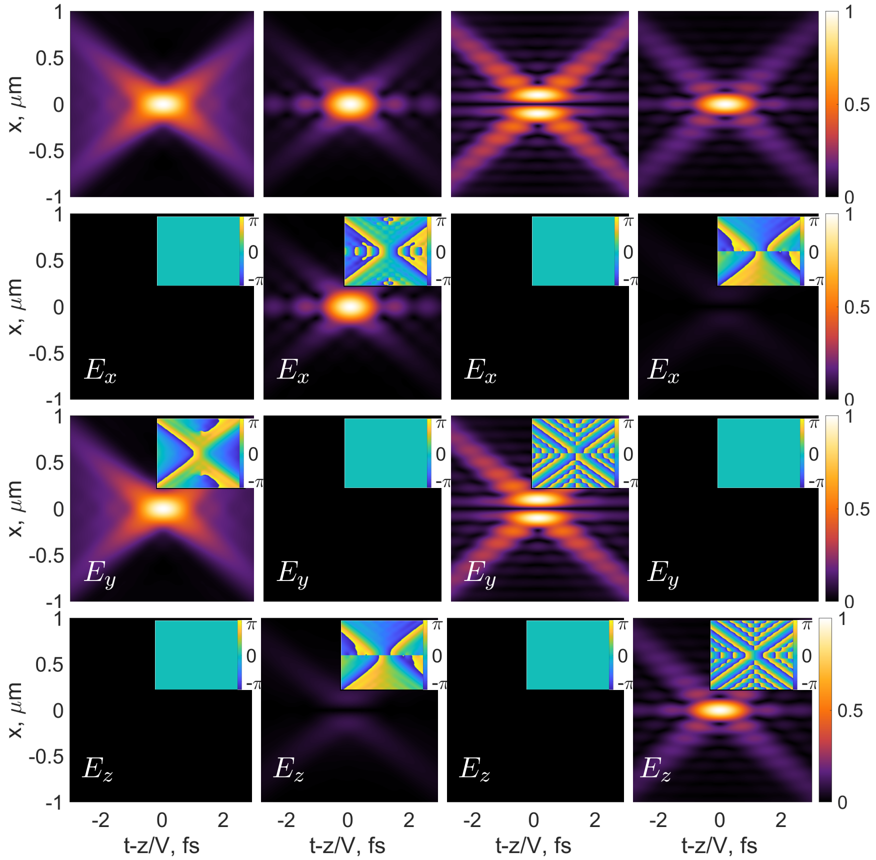

Figure 4.5: Intensity distributions of subcycle pulses in vacuum and their individual components (E_x (second row), E_y (third row), E_z (fourth row)) in the longitudinal plane for linear TE (first column), TM (second column), azimuthal (third column), and radial (fourth column) polarizations when $V/c = -5.65, \gamma = 4.35$ μm^{-1}. The insets represent the phase distribution.

An azimuthally polarized subcycle optical bullet behaves as expected—it has only two transverse components; see Figure 4.4, third column. However, the radially polarized backward propagating bullet demonstrates a rather interesting feature in the subcycle mode—its z component is the strongest due to tight focusing conditions; see Figure 4.4, last column. The FWHM sizes are $\Delta x_{azi} = 0.3518$ μm, $\Delta y_{azi} = 0.3518$ μm and $\Delta x_{rad} = 0.1709$ μm, $\Delta y_{rad} = 0.1709$ μm in transverse directions.

We now proceed to discussing the spatial structure of the vector subcycle optical bullets that propagate backward. For the sake of comparison, we investigated the same particular case of the longitudinal plane; see Figure 4.5.

We plotted the total intensity distributions as well as the individual ones in a specific longitudinal plane. Firstly, we observed a distinct difference in the shapes of linearly polarized TE and TM optical bullets, as shown in Figure 4.5. The cross-shaped peripheral part is very pronounced for the TE mode, as seen in the first and second columns. For the TM polarization, the profile is less pronounced, and the overall shape appears to be more concentrated. In particular, axial secondary maxima appear before and after the central part, giving the general shape a resemblance to a rotated Cyrillic letter 'Ж', whereas the TE mode still resembles the well-known X-shape. Due to the choice of the longitudinal plane, the TE mode has a single non-zero component. The phase of this component reveals a conical wave-front structure. The phase gradient indicates the direction of energy flow, which, as seen in the phase distribution, includes parts moving inward and outward, as previously noted in the literature [58, 131]. Similarly, linear TM polarization exhibits two electric field components in this longitudinal plane, a dominant x component and a very weak z component. The intensity profile of the x component resembles a rotated Cyrillic letter 'Ж', while the z component maintains a general X-shape with an axial void due to the singularity. The phase distributions are typical for this type of conical beam, and the energy flow for each component is as expected. The FWHM sizes are $\Delta z_{TE} = 1.6583$ fs and $\Delta z_{TM} = 1.4171$ fs in longitudinal directions.

Azimuthal and radial polarizations are shown in the third and fourth columns of Figure 4.5. The azimuthal polarization exhibits a very pronounced peripheral part of the beam. This pulsed beam has only one component in this plane. The phase distribution shows conical energy flow with a phase jump on the z axis due to the polarization singularity [38, 39]. The radially polarized mode has a dominant z component and an almost unnoticeable x component. The FWHM sizes are $\Delta z_{azi} = 1.6583$ fs, and $\Delta z_{rad} = 1.5377$ fs in longitudinal directions.

Lastly, we consider point (**3**) in Figure 4.1 (a), where the group velocity of the focus wave mode is $V/c = 1$, and the parameter $\gamma = -2.45\ \mu\mathrm{m}^{-1}$. We compare the same polarizations as follows: linear

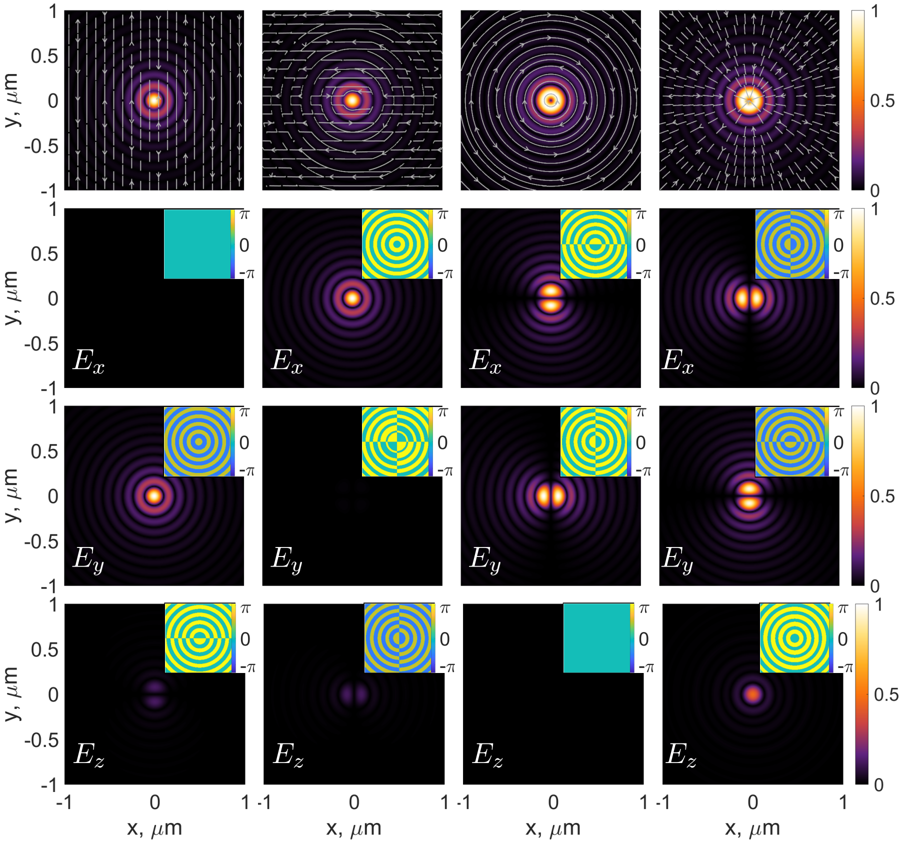

Figure 4.6: Intensity distributions of subcycle pulses in vacuum and their individual components E_x (second row), E_y (third row), E_z (fourth row) in the transverse plane for linear TE (first column), TM (second column), azimuthal (third column), and radial (fourth column) polarizations when $V/c = 1, \gamma = -2.45$ μm^{-1}. The white arrows in first row represent the orientation of the electric field. The insets represent the phase distribution.

TE (transverse electric), linear TM (transverse magnetic), radial, and azimuthal; see Equations (1.26) and (1.27).

In the transverse plane, we illustrate the intensity distributions of these subcycle pulsed beams (refer to Figure 4.6, first row). The linearly polarized TE mode does not stretch along the polarization direction in this case, a behavior well documented in the literature and usually attributed to the dominant longitudinal component (see Figure 4.6, last row). This occurs due to the rather weak z component, which is caused by a rather modest spatiotemporal dispersion; see Figure 4.1 (b). The linearly polarized TM mode does not diverge from this pattern and looks identical to the TE mode. Furthermore, in addition to the emergence of the z-component, a non-zero cross-polarized y-component is absent in this case. The spikes in the x components share the same phases (see the inset in Figure 4.6), while the other two components exhibit spikes with alternating phases. Among all the polarizations considered, the z component is the weakest. The FWHM sizes are $\Delta x_{TE} = 0.1307$ µm, $\Delta y_{TE} = 0.1307$ µm, and $\Delta x_{TM} = 0.2714$ µm, $\Delta y_{TM} = 0.1307$ µm in transverse directions.

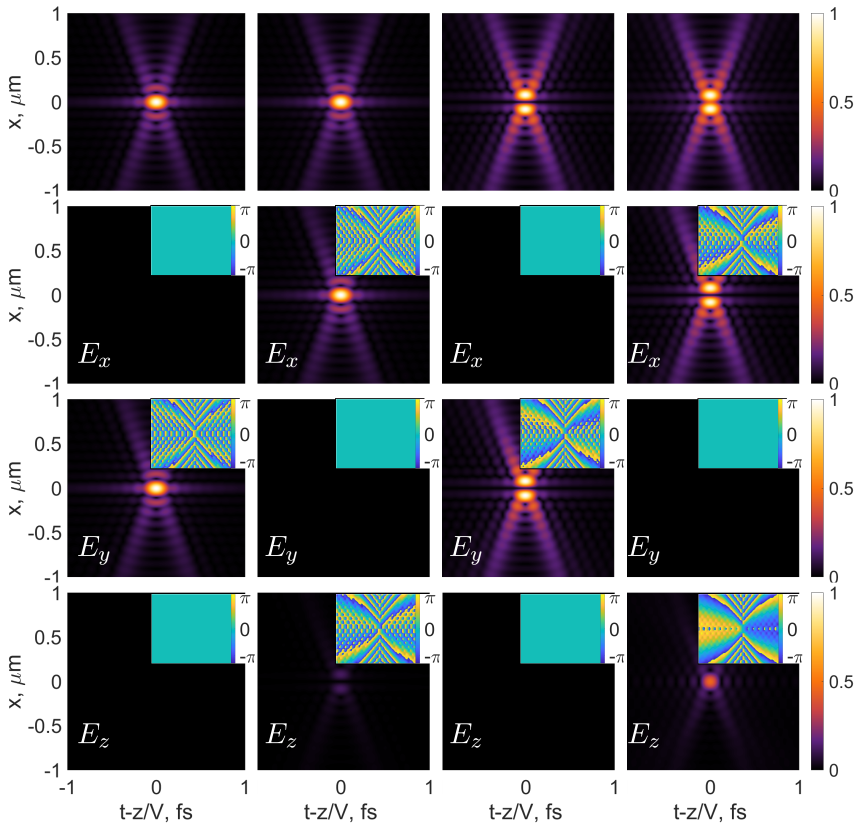

Figure 4.7: Intensity distributions of subcycle pulses in vacuum and their individual components (E_x (second row), E_y (third row), E_z (fourth row)) in the longitudinal plane for linear TE (first column), TM (second column), azimuthal (third column), and radial (fourth column) polarizations when $V/c = 1, \gamma = -2.45$ µm^{-1}. The insets represent the phase distribution.

An azimuthally polarized subcycle optical bullet behaves as expected, having only two transverse components (see Figure 4.6, third column). However, the radially polarized optical bullet exhibits a change in the subcycle mode when compared to the previous two cases; its z component is no longer dominant due to the focusing conditions (see Figure 4.6, last column). The FWHM sizes are $\Delta x_{azi} = 0.2714$ μm, $\Delta y_{azi} = 0.2714$ μm and $\Delta x_{rad} = 0.2714$ μm, $\Delta y_{rad} = 0.2714$ μm in transverse directions.

We now examine the spatial structure of the vector subcycle optical bullets that propagate forward. For comparison, we focus on the longitudinal plane, as illustrated in Figure 4.7.

We plotted the total and individual intensity distributions in this specific plane. In particular, there was no distinct difference between the shapes of linearly polarized TE and TM optical bullets. As shown in Figure 4.7, both the TE and the TM modes exhibit a pronounced cross-shaped peripheral part. The resulting profile resembles a rotated Cyrillic letter 'Ж', with axial intensity lines before and after the central part. In this plane, the TE mode has a single non-zero component, and its phase reveals a conical wave-front structure with energy flow directions indicated by the phase gradient. This includes both inward and outward movements. The TM polarization, with dominant x and weak z components, shows an intensity profile similar to a rotated Cyrillic letter 'Ж' for the x component and an X-shape with an axial singularity for the z component. The phase distributions are typical for conical beams, with the expected energy flow patterns for each component. The FWHM sizes are $\Delta z_{TE} = 0.1910$ fs and $\Delta z_{TM} = 0.1910$ fs in longitudinal directions.

For azimuthal and radial polarizations, depicted in the third and fourth columns of Figure 4.7, the azimuthal polarization shows a pronounced peripheral part with a single component in this plane. Its phase distribution indicates a conical energy flow with a phase jump on the z axis due to the polarization singularity. The radially polarized mode has an observable z component and a dominant x component. The FWHM sizes are $\Delta z_{azi} = 0.1709$ fs and $\Delta z_{rad} = 0.1709$ fs in longitudinal directions.

We introduced vector formalism to the concept of nondiffracting and nondispersive optical bullets, exploring the following different polarizations: linear, azimuthal, and radial. To showcase the variety of spatiotemporal dispersions, we selected three propagation velocities, two positive and one negative (backward propagating). The first two group velocities V were chosen for their intriguing dispersion, one being the dispersion of the X-waves and the second of the FWM with cone angles ranging from small paraxial (valid for scalar descriptions) to larger values that require a vector treatment of the electric field.

For these velocities, we examined such frequencies, resulting in the following two scenarios: one with X-wave spatiotemporal dispersion and profile and another with focus wave mode dispersion. We found that the spatiotemporal shape of the vector-subcycle optical bullet (FWM) mirrors the scalar optical X-pulses, with differences due to the presence of small non-zero longitudinal and cross-polarization components. Polarization-dependent features for these situations are negligible, thus enabling nearly scalar subcycle nondiffracting fields. Nevertheless, for the case of the X-wave, high cone angles can necessitate a vector description of the vector FWM, highlighting the distinct differences between polarizations.

In the second case, a forward-propagating superposition of Bessel beams within the Bessel zone creates a backward-propagating pulse with negative velocity V. This scenario revealed significant differences in the properties of the optical vector bullets within the dielectric material. The highly nonparaxial nature of these waves creates the longitudinal component prominent in TE and TM polarized bullets. Notably, the linearly polarized TM mode exhibits a large cross-polarized component. The azimuthally polarized bullet shows no differences, but the radially polarized wave is greatly affected, with the longitudinal electric field component dominating the intensity pattern.

A quick look into the research field gives the following hints regarding practical realizability: a high-energy subcycle pulse synthesizer based on a mid-infrared optical parametric amplifier was reported [132], subcycle-isolated attosecond pulses were generated by pumping ionizing gating [133], phase-stable subcycle mid-infrared pulses were generated from filamentation in nitrogen [134], etc. A harder task for experimentally realizing nondiffracting and nondispersing optical bullets is organizing a proper spatiotemporal dispersion. A solution to this problem might be the usage of metasurfaces [135].

These results could help improve ultrafast optics, imaging, and material processing by giving us a better understanding of the behavior and characteristics of such subcycle pulses.

CONCLUSIONS

During this work several conclusions were drawn:

1. The vectorial structure of linearly, radially and azimuthally polarized Bessel-X pulses changes the durations of the Bessel-X pulse. This becomes more pronounced as the situation becomes non-paraxial with increasing cone angle θ. This relationship is not trivial and different for linear, radial and azimuthal polarizations.

2. For the given angle θ the Bessel-X beam duration depends linearly on the temporal spectral width. However, as femtosecond durations are reached this behavior is no longer linear and the analytical model predicts differences between different polarizations as well as for different topological charges.

3. Inside a BK7 glass we can generate superluminal, subluminal and negative group velocity beams, by following the angular dispersion curve for different frequencies.

4. When group velocity $V/c = 0.63685$ and propagation constant $\gamma = -0.628\ \mu\mathrm{m}^{-1}$, the angular dispersion curve of BK7, representing angle vs frequency, exhibits both positive and negative slopes. The negative slope generates an O-shaped intensity distribution of Bessel-X beams, while the positive slope leads to an X-shaped spatiotemporal Bessel-X intensity distribution. At the infliction point, the beams transverse dimensions become considerably increased, due to the small angles required.

5. Subcycle Bessel-X pulses can be generated in free space and BK7 glass. The shortest subcycle Bessel-X pulse in vacuum corresponds to 0.56 of its central frequency cycle, while in BK7 glass, it is 0.67 of its central frequency cycle. The limit appears due to the angles required to generate subcycle pulses.

SANTRAUKA LIETUVIŲ KALBA

Įvadas

Teoriniai impulsinių nedifraguojančių pluoštų tyrimai pastaruoju metu sparčiai vystosi. Dabartinės technologijos leidžia generuoti itin trumpus, didelės galios impulsus. Siekiant geriau valdyti dispersijai ir difrakcijai atsparių impulsinių pluoštų formavimą, tiriami aštriai fokusuoti vektoriniai impulsai. Šiam tyrimui buvo naudojamas tiek analitinis, tiek skaitinis modeliavimo metodas, skirtingoms poliarizacijoms (tiesinė, azimutinė ir radialinė) ir topologiniams krūviams tirti. Taip pat analizuojami tiek greitesnių, tiek lėtesnių už šviesos greitį, bei neigiamų grupinių greičių poveikiai vektorinėms fokusuotoms židinio modoms tiek laisvoje erdvėje, tiek dielektrinėse medžiagose.

Taip pat buvo nagrinėjamos vektorinės radialinės bei azimutinės poliarizacijų savybės bei jų įtaka Bessel-X impulso trukmei. Tyrimas orientuojamas į stipriai neparaksialinius vektorinius Bessel-X impulsus [1], pateikiant analitines išraiškas ir ištiriant naujas savybes, atsirandančias dėl poliarizacijų nehomogeniškumo. Toliau tyrimas pereina prie kito tipo optinių kulkų – vektorinių fokusuotų židinio modų [2], kurios yra X-bangų ir Bessel-X impulsų sprendiniai dielektrinėje dispersinėje terpėje. Šiuo tikslu buvo pasirinkta viena dielektrinė medžiaga ir analizuota erdvės-laiko spektrų dispersijos priklausomybė [3]. Bendru atveju erdvės-laiko spektrų išraiška aprašo kūgio kampu sklindančius Bessel pluoštus, kurie Bessel zonoje sklinda fiksuotu grupiniu greičiu V, kuris gali būti tiek greitesnis už šviesos greitį [4, 5], tiek lėtesnis už šviesos greitį [6] ar net neigiamas (t. y. sklindantis atgal) [7]. Prie didelių Bessel pluošto kūgio kampų būtinas tinkamas vektorinis aprašymas. Šiame darbe vektorinis aprašymas pritaikomas optinėms kulkoms ir analizuojama tokių pluoštų struktūra medžiagoje, siejant pluošto trukmę su pluošto skersiniu dydžiu, centriniu dažniu ir optinės kulkos sklidimo greičiu, siekiant ištirti vektorinių optinių kulkų generavimą ir elgesį dielektrinėje terpėje. Eksperimentiniam difrakcijai ir dispersijai atsparių pluoštų taikymui būtinas tinkamas stipriai fokusuotų vektorinių impulsų matematinis aprašymas. Šiame darbe pateikti rezultatai leidžia suprasti ryšius tarp pluošto skersinio dydžio, kiekvieno atskiro komponento intensyvumo (x, y, z) (ypatingą dėmesį skiriant elektrinio lauko z komponentui), priklausomai nuo centrinio dažnio, poliarizacijų, skirtingų grupinio greičio V ir integravimo konstantos γ, siejančios grupinį greitį su faziniu greičiu, reikšmių.

Darbo tikslas ir uždaviniai

Pagrindinis šio darbo uždavinys yra ištirti vektorines optines kulkas (difrakcijai ir dispersijai atsparius impulsinius pluoštus) vakuume ir dielektrinėje medžiagoje bei jų savybes su skirtingomis šiame darbe apibrėžtomis topologijomis:

- Ištirti Bessel-X pluošto erdvinę struktūrą, jo vektorines savybes, esant skirtingiems kūgio kampams ir topologiniams krūviams.
- Ištirti Bessel-X pluošto laikinę trukmę, jo vektorines savybes esant skirtingiems kūgio kampams ir topologiniams krūviams.
- Ištirti vektorines fokusuotas židinio modas tiek greitesnių, tiek lėtesnių už šviesos greitį, bei neigiamų grupinių greičių atvejus bei jų savybes.
- Ištirti subciklines vektorines fokusuotas židinio modas vakuume ir BK7 stikle.

Darbo naujumas ir aktualumas

- Šiame darbe pateikiamas analitinis impulsinių, nedifraguojančių pluoštų modelis su optiniu sūkuringumu ir radialine bei azimutine poliarizacijomis.
- Buvo ištirtos vektorinių Bessel-X impulsų laikinių FWHM trukmių priklausomybės tiesinei, azimutinei ir radialinei poliarizacijoms.
- Parodyta, kad BK7 stikle optinėje bangos ilgių srityje galima sumodeliuoti tiek X, tiek O formos pluoštus naudojant fokusuotas židinio modas.
- BK7 stikle buvo sumodeliuotos tiek greitesnių, tiek lėtesnių už šviesos greitį, bei neigiamų grupinių greičių fokusuotos židinio modos.

Ginamieji teiginiai

- Tiesinės, radialinės ir azimutinės poliarizacijos Bessel-X impulsų vektorinė struktūra keičia jų trukmę, ypač neparaksialiniame režime, kur Bessel-X kūgio kampas yra didesnis už 45 laipsnius. Impulso trukmės priklausomybė nuo kūgio kampo nėra triviali ir skiriasi tiesinei, radialinei ir azimutinei poliarizacijoms.

- Esant fiksuotam Bessel-X kūgio kampui θ, Bessel-X impulso trukmė netiesiškai priklauso nuo laikinio spektrinio pločio, kol trukmės yra mažesnės už dešimtis femtosekundžių. Šis reiškinys nukrypsta nuo įprastos tiesinės priklausomybės pluoštams be kampinės dispersijos. Šis reiškinys buvo stebimas tiek tiesinėms, tiek azimutinei ir radialinei poliarizacijoms, tiek ir skirtingiems topologiniams krūviams.

- Chromatinė dispersija BK7 stikle leidžia paskaičiuoti kampinės dispersijos kreives, su kuriomis galima generuoti tiek greitesnių, tiek lėtesnių už šviesos greitį, bei neigiamų grupinių greičių Bessel-X pluoštus.

- BK7 stikle grupiniam greičiui $V/c = 0{,}63685$ ir parametrui $\gamma = -0{,}628\ \mu\mathrm{m}^{-1}$ kampinės dispersijos kreivės $\theta(\omega)$, turi tiek neigiamą, tiek teigiamą nuolydžius. Neigiamas nuolydis generuoja O formos intensyvumo pasiskirstymus Bessel-X pluoštui, o teigiamas nuolydis formuoja X formos intensyvumo pasiskirstymus Bessel-X pluoštui.

- Subcikliniai Bessel-X impulsai gali būti generuojami tiek laisvoje erdvėje, tiek BK7 stikle. Trumpiausias subciklinis Bessel-X impulsas vakuume yra 0,56 jo centrinio dažnio ciklo, o BK7 stikle – 0,67 jo centrinio dažnio ciklo.

Autoriaus indėlis

Autorius atliko visus modeliavimus, apdorojo ir išanalizavo gautus duomenis. Autorius taip pat prisidėjo prie visų rankraščių parengimo ir diskusijų.

[A1] Autorius parašė kodą visiems reikalingiems Bessel-X modeliavimams atlikti, išanalizavo ir aprašė rezultatus bei parengė iliustracijas.

[A2] Autorius parašė kodą visiems reikalingiems optinių kulkų modeliavimams atlikti, išanalizavo ir aprašė rezultatus bei parengė iliustracijas.

[A3] Autorius parašė kodą visiems reikalingiems subciklinių impulsų modeliavimams atlikti, išanalizavo ir aprašė rezultatus bei parengė iliustracijas.

[A4] Autorius parašė kodą visiems reikalingiems modeliavimams atlikti, išanalizavo ir aprašė rezultatus bei parengė dalį iliustracijų. Eksperimentinė dalis atlikta su kolegų pagalba.

Struktūrizuotų pluoštų inžinerija sparčiai vystosi dėl labai plačių pritaikymo galimybių ne tik optikoje, bet ir fizikoje bendrai. Viena iš kliūčių pluošto valdyme yra difrakcija. Sklindant pluoštui, jo skersiniai matmenys plinta ir intensyvumas silpnėja. Nedifraguojantys pluoštai šios problemos išvengia ribotoje erdvėje, per konstruktyvią interferenciją. Tokių pluoštų pavyzdžiai – Bessel, Weber, Mathieu ir Airy (žr. 1.1 pav.). Idealiu atveju šie pluoštai reikalauja begalinės energijos, tačiau mes nagrinėjame erdvėje ribotus šių pluoštų artinius. Kita problema impulsinių pluoštų panaudojime – dispersija. Skirtingi pluoštų dažniai medžiagoje sklinda skirtingu greičiu, todėl stebimas pluošto išplitimas. Dispersijos galima išvengti naudojant skirtingų dažnių nedifraguojančių pluoštų superpoziciją. Vienas iš tokių metodų yra vadinamas fokusuotų židinio modų metodu, kuriame skirtingų dažnių pluoštai suvedami skirtingais kampais, taip išvengiant dispersijos. Kita svarbi struktūrizuotų pluoštų savybė yra poliarizacija. Aštriai fokusuojant pluoštus, skaliarinis tokių pluoštų aprašymas tampa nepakankamai tikslus, todėl naudojame vektorinį pluošto elektrinio lauko aprašymą. Tai leidžia aprašyti nehomogenines poliarizacijas ir jų sąveiką su medžiaga, kas yra svarbu daugelyje eksperimentų.

Šiame darbe yra nagrinėjami neparaksialiniai vektoriniai Bessel-X impulsai, įvedant analitinį jų aprašymą ir nagrinėjame kartu su nehomogeninėmis poliarizacijomis. Bessel-X impulsų metodo analitinė išraiška gaunama tik kai impulsas sklinda laisvoje erdvėje, todėl eksperimentiškai naudojamas retai. Norint aprašyti nedifraguojančius impulsus medžiagoje, naudojamas skaitmeninis integravimas. Šis metodas yra žinomas kaip X-bangų metodas, kuris aprašo impulsus ir dispersinėje medžiagoje, įvertinant medžiagos lūžio rodiklį $n(\omega)$. Tolesniame darbo etape naudojame optines kulkas – tai fokusuotų židinio modų metodas. Šiuo metodu galime nagrinėti pluoštų sklidimą ne tik laisvoje erdvėje, bet ir dispersinėje medžiagoje. Šiuo metodu galime apsirašyti atsparumą dispersijai suvesdami skirtingus dažnius atitinkamais kampais $\theta(\omega)$. Tokiu būdu gauname dispersijai atsparius impulsus, kurie sklinda erdvėje norimu grupiniu ir faziniu greičiais, o tokie pluoštai vadinami optinėmis kulkomis. Fokusuotų židinio modų metodu galime gauti tiek greitesnius už šviesos greitį, tiek neigiamo grupinio greičio pluoštus. Neigiamas grupinio greičio pluošto gaubtinė juda neigiama išilginės koordinatės kryptimi, nors jį sudarančios plokščios bangos sklinda į priekį. Vienas iš Bessel pluoštų gavimo metodų pavaizduotas 1.2 pav. Čia naudojamas aksikonas, kuris sukuria 2 persiklojančius pluoštus, kur dėl superpozicijos susidaro Bessel pluoštas ribotoje erdvėje. Taip pat pridėję spiralinę fazinę plokštelę, kur m parodo kiek kartų fazinė plokštelė pakeičia fazę per 2π azimuto kampu, gauname aukštesnių eilių Bessel pluoštus. Nedifraguojantys pluoštai turi unikalių savybių, tokių kaip pluošto rekonstrukcija už kliūties. Tokiu atveju, net jei dalis pluošto intensyvumo yra užblokuojama, jo struktūra atstato save už kliūties, įskaitant ir poliarizacijos bei intensyvumo skirstinius. Ši savybė yra itin svarbi taikymams optinėje mikroskopijoje, lazerinėse technologijose ir duomenų perdavimo sistemose, kur būtinas didelis atsparumas aplinkos trikdžiams.

Nedifraguojančių pluoštų sūkuriai

Nedifraguojančių pluoštų sūkuriai yra sraigtinės dislokacijos, o bangos fronto paviršius yra sraigtinis. Sūkurio centre yra neapibrėžtos fazės taškas. Neapibrėžtos fazės taškuose lauko amplitudė yra artima nuliui. Topologinio krūvio ženklas, teigiamas ar neigiamas, nusako į kurią pusę, dešininę ar kairinę, toks sūkurys suksis. Nedifraguojantys pluoštai, turintys optinius sūkurius, išsiskiria iš kitų pluoštų savo savybėmis. Pridėjus prie sūkurinio pluošto net nykstamai mažą koherentinį foną, didesnio nei vienetinio topologinio krūvio sūkurys skyla į $|m|$ vienetinio topologinio krūvio sūkurius. Šviesos sūkurių superpozicijos rezultatas skiriasi nuo klasikinės superpozicijos rezultatų. Bendraašių Lagero Gauso sūkurių superpozicijos atveju, sudėtiniame pluošte atsiranda sūkuriai, kurių skaičius kinta sklidimo metu ir priklauso nuo santykinių pluoštų matmenų bei amplitudžių. Sudėtingi topologiniai dariniai gali susiformuoti šviesos pluoštuose – sūkurių trajektorijos nuo jų susidarymo iki anihiliacijos sudaro sudėtingas mazgų, raiščių ir kitų aukštos topologijos struktūrų konfigūracijas. Femtosekundinės trukmės sūkuriai, sklisdami ore, skatina filamentų formavimąsi. Dvejopo lūžio kristale optiniai sūkuriai lemia poliarizacijos singuliarumo atsiradimą, be to, pastebėtas judesio kiekio perdavimas tarp akustinio ir optinio sūkurio. Fokusuotos židinio modos (optinės kulkos), kurios yra nagrinėjamos šiame darbe, turi judesio kiekio momentą, kuris yra proporcingas jas sudarančių nedifraguojančių pluoštų topologiniam krūviui m. Sudėtingos topologinės sandaros sūkuriniai laukai yra svarbūs interferometrijoje, mikromanipuliavime, kaip valdomi optinių dalelių pincetai, mikrovariklių varomoji jėga, mikrosrovių generatoriai, asimetrinių dalelių manipuliatoriai. Bessel pluoštų sūkuriai dėl savo nedifraguojančios prigimties gali transportuoti objektus didesniais atstumais, lyginant su Lagero Gauso sūkuriais.

Bessel-X pluoštų poliarizacijos

Tiesinės poliarizacijos Bessel-X pluoštų aprašymui, vektorizavimo lygtyje (1.13) pasirenkame ortą $\mathbf{a} = \mathbf{e_x}$. Gauname Dekarto koordinačių sistemoje sprendinius TE (1.16) ir TM (1.17). TE šiuo atveju yra tiesinės poliarizacijos ir neturi vieno iš ortogonalaus skersinio komponento. TM atveju abu skersiniai komponentai egzistuoja. Atvejo su $\mathbf{a} = \mathbf{e_y}$ nėra tikslo nagrinėti, kadangi atitiks $\mathbf{a} = \mathbf{e_x}$ atvejį, tik pasuktą 90 laipsnių kampu. Pasirinkę $\mathbf{a} = \mathbf{e_z}$, gauname TE (1.19) ir TM (1.20) išraiškas, jas apsirašome cilindrinėje koordinačių sistemoje. Šiuo atveju TE poliarizacija atitinka azimutinę poliarizaciją, o TM atitinka radialinę poliarizaciją. Daugelyje taikymų pastebėta, kad efektyvu naudoti cilindrinės simetrijos pluoštus – azimutinę ir radialinę. Azimutinės poliarizacijos elektrinis laukas nukreiptas išilgai e_φ orto, o radialinės išilgai e_ρ orto cilindrinėje koordinačių sistemoje. Šios poliarizacijos atvaizduotos 1.6 pav. Matome, kad azimutinės poliarizacijos atveju išilginio komponento nėra. Kai $m = 0$, turime $M_\rho = 0$, vadinasi tokiu atveju pluoštas yra idealiai azimutinis. Radialinės poliarizacijos atveju, kai $m = 0$, komponentas $N_\varphi = 0$. Tačiau, kai $m \neq 0$, visi 3 komponentai egzistuoja. Eksperimentiškai azimutinės ir radialinės poliarizacijos vektoriniai nedifraguojantys pluoštai gali būti gaunami iš tiesinės poliarizacijos Bessel pluošto, panaudojant erdvines fazines plokšteles.

Rezultatų apžvalga

Azimutinės ir radialinės poliarizacijos impulsiniai Bessel-X sūkuriai

Šiame skyriuje tiriame tiesinės, azimutinės ir radialinės poliarizacijos Bessel-X impulsinius pluoštus. Pluošto spektrą apsirašę per Gauso pasiskirstymo artinį (1.11) ir analitiškai išreiškę skaliarinę elektrinio lauko sklidimo lygtį (1.12), ją vektorizuojame (1.13). Pasirinkdami vektorizavimo orto kryptį a, gauname tiesines arba azimutinę/radialinę poliarizacijas. Gaunamos išraiškos pateiktos (1.16-1.18) tiesinės poliarizacijos atvejams ir (1.18-1.20) radialinės ir azimutinės poliarizacijos atvejais. Atlikę modeliavimus gauname 2.9 pav., kuriame matome atskirų komponentų intensyvumų pasiskirstymus, skirtingiems kūgio kampams θ. Tiek tiesinės TE modos atveju, tiek radialinės poliarizacijos atvejais, visiems skaičiuotiems topologiniams krūviams m matome, kad didinant kampą, visas intensyvumas pereina iš skersinių į išilginį komponentą. Azimutinė poliarizacija išilginio komponento neturi ir jis neatsiranda didinant kampą. Tiesinės poliarizacijos TM modos atveju, didinant kampą θ, išilginė komponentė didėja iki kol pasiekiamas apie 50 laipsnių kampas, tačiau ir toliau didinant θ kampą, išilginis komponentas silpnėja, o intensyvumas pradeda maišytis tarp skersinių komponentų, todėl stebime ortogonalaus skersinio komponento atsiradimą. Šiuo atveju ortogonalusis skersinis komponentas nepralenkia pagrindinio skersinio komponento savo intensyvumu. Šis procesas yra sustiprintas, kai topologinis krūvis $m = 2$. Apibendrinus komponentų pasiskirstymus matome, kad kuo aštriau fokusuojamas pluoštas, tuo didesnė vektorinio lauko aprašymo svarba. Tiriant impulso trukmės priklausomybę nuo kampo θ, matome, kad didinant kampą, didėja impulso trukmė 2.10 (a, c) pav. Keisdami pradinio impulso trukmės parametrą α, matome tiesinę priklausomybę iki kol yra pasiekiamos dešimčių femtosekundžių trukmės. Trumpesniems impulsams matome atsiskyrimą priklausomai nuo poliarizacijos ir topologinių krūvių 2.10 (b, d) pav.

Vektorinės optinės kulkos dielektrinėje medžiagoje

Tolimesniame tyrime buvo įvesta bangos vektoriaus k priklausomybė nuo medžiagos lūžio rodiklio $n(\omega)$ (1.22). Čia apsibrėžiame, kad pluoštas sklinda be dispersijos, vadinasi, jų k_z bangos vektoriai turi būti lygūs. Pasirenkame norimą grupinį greitį V ir integravimo konstantą γ, kuri sieja pluošto fazinį greitį su grupiniu greičiu. Iš šios išraiškos gauname kampinės dispersijos kreivės apibrėžimą (1.23) ir atvaizduojame šias kreives 3.1 pav. Šios kreivės mums parodo, kokiu kampu θ turi būti suleidžiamas ω dažnio Bessel pluoštas, kad pasirinktoje medžiagoje gautume impulsą, kuriam nepasireiškia dispersija. Šiame skyriuje bangos lygtis sprendžiama skaitiškai integruojant (1.26-1.30) išraiškas. Pasirinktas spektras – stačiakampis (3.1). Pasirinkę kreivę 3.1 pav. (b)

(2), matome lūžio tašką, kurios pirmojoje dalyje yra anomalioji kampinė dispersija, o antroje dalyje – normalioji kampinė dispersija. Atvaizdavę šiuos pluoštus matome, kad jų formos skiriasi. Anomaliojoje srityje pasireiškia O formos pluoštas 3.6-3.11 pav., o normaliojoje – X formos pluoštas 3.2-3.5 pav., nepriklausomai nuo pasirinkto topologinio krūvio m ir poliarizacijų. Taip pat buvo pasirinktas ir neigiamas grupinis greitis 3.12–3.15 pav. Tokiu atveju pluoštas juda neigiama išilginės koordinatės kryptimi. Idealiu atveju neigiamo grupinio greičio pluoštai yra begalinės energijos ir sklinda iki pat šaltinio, tačiau ribotos energijos realiu atveju sklistų nuo Bessel zonos pabaigos iki Bessel zonos pradžios, t.y. būtų apribotas Bessel zonoje. Buvo pastebėta, kad artėjant prie jau minėto dispersinės kreivės lūžio taško, pluošto skersiniai matmenys stipriai išsiplečia. Šie rezultatai apibendrinti 3.16 pav. Taip yra todėl, kad ties lūžio tašku Bessel pluoštai suvedami mažais kampais, o kaip jau matėme praeitame skyriuje, mažesnių kampų θ pluoštų skersiniai matmenys yra didesni. Taip pat atvaizduoti atskirų komponentų intensyvumai priklausomai nuo pasirinktos kampinės dispersijos kreivės ir centrinio dažnio padėties 3.17 pav. Matome taip pat prieš tai jau stebėtą tendenciją, kad aštriau fokusuojant kampus θ, stebime išilginio komponento stiprėjimą skersinių komponentų atžvilgiu.

Vektoriniai optiniai nedifraguojantys subcikliniai impulsai

Šiame subciklinių pluoštų tyrime ieškome optimalių parametrų V/c ir γ, siekdami gauti trumpiausius Bessel pluošto impulsus laisvoje erdvėje (4.1 pav. (a)) ir medžiagoje (4.1 pav. (b)). Apsibrėžiame, kad trumpiausias impulsas yra centrinio dažnio ω_c pusė periodo T_c (4.2). Ribojimas dėl trumpiausio impulso, kurį galime sugeneruoti nuo V/c ir γ parametrų medžiagoje, atsiranda dėl reikiamo θ kampo (4.1 pav. (c)). Spektras $S(\omega)$ šiuo atveju yra naudojamas stačiakampis, aprašomas per "boxcar" funkciją (4.1). TE ir TM laukų (1.26-1.30) integravimui naudojame Matlab funkciją "quadgk". Trumpiausi impulsai, kuriuos galime sugeneruoti vakuume, yra $\Delta t = 0.55T_c$, o BK7 stikle $\Delta t = 0.67T_c$. Optimalūs parametrai rasti tiek teigiamų grupinių greičių srityje, tiek neigiamų grupinių greičių srityje. Šiuos pluoštus atvaizdavome visoms šiame darbe tiriamoms poliarizacijoms: tiesinei, azimutinei ir radialinei. Atvaizdavome Bessel pluoštus su teigiamu grupiniu greičiu (4.2-4.3 pav.), kai grupinis greitis lygus šviesos greičiui $V = c$ (4.4-4.5 pav.), ir su neigiamu grupiniu greičiu (4.6-4.7 pav.). Fokusuotų židinio modų impulso matmenys skersine kryptimi priklauso nuo impulso spektro centrinio dažnio padėties kampinės dispersijos kreivėje. Didžiausių skersinių matmenų nedifraguojantys pluoštai gaunami anomalios grupinių greičių dispersijos srityje, kai pluošto sklidimo kampai θ yra maži.

Išvados

Atliekant darbą buvo padarytos šios išvados:

1. Tiesinės, radialinės ir azimutinės poliarizacijos Bessel-X impulsų vektorinė struktūra keičia jų trukmę. Šis poveikis tampa labiau pastebimas, kai kūgio kampas θ didėja, ir situacija tampa neparaksialinė. Impulso trukmės priklausomybė nuo kūgio kampo nėra triviali ir skiriasi tiesinei, radialinei ir azimutinei poliarizacijoms.

2. Pasirinktam kūgio kampui θ, Bessel-X impulso trukmė tiesiškai priklauso nuo laikinio spektrinio pločio. Tačiau, kai pasiekiamos dešimčių femtosekundžių trukmės, šis ryšys nebegalioja, o analitinis modelis aprašo atsiradusius skirtumus skirtingoms poliarizacijoms ir skirtingiems topologiniams krūviams.

3. BK7 stikle galima generuoti tiek greitesnes, tiek lėtesnes už šviesos greitį, bei neigiamas grupinių greičių fokusuotas židinio modas, naudojant paskaičiuotas kampinės dispersijos kreives.

4. BK7 stikle grupiniam greičiui $V/c = 0.63685$ ir parametrui $\gamma = -0{,}628\ \mu\mathrm{m}^{-1}$, gauname normaliąją ir anomaliąją kampinės dispersijos sritis. Anomalioji sritis turi neigiamą kreivės nuolydį, o normalioji teigiamą kreivės nuolydį. Anomaliojoje srityje galime generuoti O formos, o normaliojoje X formos impulsinius Bessel pluoštus optiniame bangos ilgių diapazone. Ties kampinės dispersijos kreivės lūžio tašku pluošto matmenys sparčiai išplinta dėl mažų kampų reikalingų Bessel-X pluoštui sudaryti.

5. Subcikliniai Bessel-X impulsai gali būti generuojami tiek laisvoje erdvėje, tiek BK7 stikle. Trumpiausias subciklinis Bessel-X impulsas vakuume yra 0,56 jo centrinio dažnio ciklo, o BK7 stikle – 0,67 jo centrinio dažnio ciklo. Trumpiausio impulso limitas atsiranda dėl kampų reikalingų tokiam pluoštui sudaryti.

BIBLIOGRAPHY

[1] K. Laurinavičius, S. Orlov, A. Gajauskaitė, Azimuthally and radially polarized pulsed bessel-x vortices, Optik **270**, 169998 (2022).

[2] K. Laurinavičius, S. Orlov, A. Gajauskaitė, Vector optical bullets in dielectric media: Polarization structures and group-velocity effects, Applied Sciences **14**(10), 3984 (2024).

[3] S. Orlov, A. Stabinis, Angular dispersion of diffraction-free optical pulses in dispersive medium, Optics communications **240**(1-3), 1–8 (2004).

[4] M. Zamboni-Rached, E. Recami, H. E. Hernández-Figueroa, New localized superluminal solutions to the wave equations with finite total energies and arbitrary frequencies, The European Physical Journal D-Atomic, Molecular, Optical and Plasma Physics **21**(2), 217–228 (2002).

[5] H. Valtna, K. Reivelt, P. Saari, Methods for generating wideband localized waves of superluminal group velocity, Optics communications **278**(1), 1–7 (2007).

[6] H. E. Kondakci, A. F. Abouraddy, Optical space-time wave packets having arbitrary group velocities in free space, Nature communications **10**(1), 929 (2019).

[7] C. J. Zapata-Rodríguez, M. A. Porras, X-wave bullets with negative group velocity in vacuum, Optics letters **31**(23), 3532–3534 (2006).

[8] H. Rubinsztein-Dunlop, A. Forbes, M. V. Berry, M. R. Dennis, D. L. Andrews, M. Mansuripur, C. Denz, C. Alpmann, P. Banzer, T. Bauer, et al., Roadmap on structured light, Journal of Optics **19**(1), 013001 (2016).

[9] V. Shvedov, A. R. Davoyan, C. Hnatovsky, N. Engheta, W. Krolikowski, A long-range polarization-controlled optical tractor beam, Nature photonics **8**(11), 846–850 (2014).

[10] F. Mitri, R. Li, L. Guo, C. Ding, Optical tractor bessel polarized beams, Journal of Quantitative Spectroscopy and Radiative Transfer **187**, 97–115 (2017).

[11] M. E. Friese, T. A. Nieminen, N. R. Heckenberg, H. Rubinsztein-Dunlop, Optical alignment and spinning of laser-trapped microscopic particles, Nature **394**(6691), 348–350 (1998).

[12] G. Milione, A. Dudley, T. A. Nguyen, O. Chakraborty, E. Karimi, A. Forbes, R. R. Alfano, Measuring the self-healing of the spatially inhomogeneous states of polarization of vector bessel beams, Journal of Optics **17**(3), 035617 (2015).

[13] T. Vettenburg, H. I. Dalgarno, J. Nylk, C. Coll-Lladó, D. E. Ferrier, T. Čižmár, F. J. Gunn-Moore, K. Dholakia, Light-sheet microscopy using an airy beam, Nature methods **11**(5), 541–544 (2014).

[14] Y.-X. Ren, H. He, H. Tang, K. K. Wong, Non-diffracting light wave: Fundamentals and biomedical applications, Frontiers in Physics **9**, 698343 (2021).

[15] S. A. Akhmanov, S. Y. Nikitin, *Physical optics* (Oxford University Press, 1997).

[16] M. N. Vesperinas, *Scattering and diffraction in physical optics* (World Scientific Publishing Company, 2006).

[17] C. A. Bennett, *Principles of physical optics* (John Wiley & Sons, 2022).

[18] J. Durnin, Exact solutions for nondiffracting beams. i. the scalar theory, JOSA A **4**(4), 651–654 (1987).

[19] F. Gori, G. Guattari, C. Padovani, Bessel-gauss beams, Optics communications **64**(6), 491–495 (1987).

[20] J. C. Gutiérrez-Vega, M. Iturbe-Castillo, S. Chávez-Cerda, Alternative formulation for invariant optical fields: Mathieu beams, Optics letters **25**(20), 1493–1495 (2000).

[21] C. López-Mariscal, M. A. Bandres, J. C. Gutiérrez-Vega, S. Chávez-Cerda, Observation of parabolic nondiffracting optical fields, Optics express **13**(7), 2364–2369 (2005).

[22] G. Siviloglou, J. Broky, A. Dogariu, D. Christodoulides, Observation of accelerating airy beams, Physical Review Letters **99**(21), 213901 (2007).

[23] J. C. Gutiérrez-Vega, M. A. Bandres, Helmholtz–gauss waves, JOSA A **22**(2), 289–298 (2005).

[24] B. Bokić, Y. de Coene, M. A. Ferrara, T. Verbiest, Y. Caudano, B. Kolaric, Structured light from classical to quantum perspectives, Symmetry **16**(8), 1053 (2024).

[25] Y. Shen, Q. Zhan, L. G. Wright, D. N. Christodoulides, F. W. Wise, A. E. Willner, K.-h. Zou, Z. Zhao, M. A. Porras, A. Chong, et al., Roadmap on spatiotemporal light fields, Journal of Optics **25**(9), 093001 (2023).

[26] S. Orlov, A. Gajauskaite, A. Juršėnas, Propagation of vector nondiffracting and nondispersive pulsed beams through an air-dielectric planar interface, Procedia CIRP **74**, 585–588 (2018).

[27] J. N. Hodgson, *Optical absorption and dispersion in solids* (Springer Science & Business Media, 2012).

[28] S. Orlov, A. Piskarskas, A. Stabinis, Localized optical subcycle pulses in dispersive media, Optics letters **27**(24), 2167–2169 (2002).

[29] P. Saari, H. Sõnajalg, Pulsed bessel beams, Laser Physics **7**(1), 32–39 (1997).

[30] K. Reivelt, P. Saari, Optical generation of focus wave modes, JOSA A **17**(10), 1785–1790 (2000).

[31] M. A. Porras, G. Valiulis, P. Di Trapani, Unified description of bessel x waves with cone dispersion and tilted pulses, Physical Review E **68**(1), 016613 (2003).

[32] M. A. Salem, H. Bağcı, Reflection and transmission of normally incident full-vector x waves on planar interfaces, JOSA A **29**(1), 139–152 (2012).

[33] H. E. Kondakci, A. F. Abouraddy, Diffraction-free space–time light sheets, Nature Photonics **11**(11), 733–740 (2017).

[34] M. Yessenov, L. A. Hall, K. L. Schepler, A. F. Abouraddy, Space-time wave packets, Advances in Optics and Photonics **14**(3), 455–570 (2022).

[35] J. Davila-Rodriguez, J. C. Gutiérrez-Vega, Helical mathieu and parabolic localized pulses, JOSA A **24**(11), 3449–3455 (2007).

[36] R. Butkus, S. Orlov, A. Piskarskas, V. Smilgevicius, A. Stabinis, Phase matching of optical x-waves in nonlinear crystals, Optics communications **244**(1-6), 411–421 (2005).

[37] S. Orlov, A. Stabinis, V. Smilgevicius, G. Valiulis, A. Piskarskas, Parametric excitation of x-waves by downconversion of bessel beams in nonlinear crystals, Optics letters **32**(1), 68–70 (2007).

[38] R. Dorn, S. Quabis, G. Leuchs, Sharper focus for a radially polarized light beam, Physical review letters **91**(23), 233901 (2003).

[39] R. Dorn, S. Quabis, G. Leuchs, The focus of light—linear polarization breaks the rotational symmetry of the focal spot, Journal of modern optics **50**(12), 1917–1926 (2003).

[40] S. Orlov, U. Peschel, T. Bauer, P. Banzer, Analytical expansion of highly focused vector beams into vector spherical harmonics and its application to mie scattering, Physical Review A **85**(6), 063825 (2012).

[41] S. Orlov, J. Berškys, Vector-spherical-harmonics representation of vector complex source beams carrying vortices, Physical Review A **102**(6), 063532 (2020).

[42] I. Gonoskov, A. Aiello, S. Heugel, G. Leuchs, Dipole pulse theory: Maximizing the field amplitude from 4 π focused laser pulses, Physical Review A **86**(5), 053836 (2012).

[43] S. Orlov, U. Peschel, Complex source beam: A tool to describe highly focused vector beams analytically, Physical Review A **82**(6), 063820 (2010).

[44] S. Orlov, P. Banzer, Vectorial complex-source vortex beams, Physical Review A **90**(2), 023832 (2014).

[45] F. Mitri, Superposition of nonparaxial vectorial complex-source spherically focused beams: Axial poynting singularity and reverse propagation, Physical Review A **94**(2), 023801 (2016).

[46] R. Gutiérrez-Cuevas, N. J. Moore, M. A. Alonso, Lorenz-mie scattering of focused light via complex focus fields: An analytic treatment, Physical Review A **97**(5), 053848 (2018).

[47] T. Bauer, S. Orlov, U. Peschel, P. Banzer, G. Leuchs, Nanointerferometric amplitude and phase reconstruction of tightly focused vector beams, Nature Photonics **8**(1), 23–27 (2014).

[48] R. Oron, S. Blit, N. Davidson, A. A. Friesem, Z. Bomzon, E. Hasman, The formation of laser beams with pure azimuthal or radial polarization, Applied Physics Letters **77**(21), 3322–3324 (2000).

[49] G. Machavariani, Y. Lumer, I. Moshe, A. Meir, S. Jackel, Spatially-variable retardation plate for efficient generation of radially-and azimuthally-polarized beams, Optics Communications **281**(4), 732–738 (2008).

[50] M. Beresna, M. Gecevičius, P. G. Kazansky, T. Gertus, Radially polarized optical vortex converter created by femtosecond laser nanostructuring of glass, Applied Physics Letters **98**(20), 201101 (2011).

[51] Z.-Y. Wang, Z. Zhou, H. Zhang, Y. Wei, H.-G. Yu, W. Hu, W. Chen, H.-T. Dai, L.-L. Ma, C.-W. Qiu, et al., Vectorial liquid-crystal holography, eLight **4**(1), 5 (2024).

[52] M. Mazanov, O. Yermakov, I. Deriy, O. Takayama, A. Bogdanov, A. V. Lavrinenko, Photonic spin hall effect: contribution of polarization mixing caused by anisotropy, Quantum Reports **2**(4), 489–500 (2020).

[53] F. I. Fedorov, K teorii polnogo otrazheniya, Doklady Akademii Nauk SSSR **105**(3), 465–468 (1955).

[54] C. Imbert, Calculation and experimental proof of the transverse shift induced by total internal reflection of a circularly polarized light beam, Physical Review D **5**(4), 787 (1972).

[55] Z. Bouchal, M. Olivík, Non-diffractive vector bessel beams, Journal of Modern Optics **42**(8), 1555–1566 (1995).

[56] J. Stratton, I. Antennas, P. society, electromagnetic theory (2007).

[57] P. Morse, H. Feshbach, Methods of theoretical physics, number 2 tom, International series in pure and applied physics (McGraw-Hill, 1953) (1953).

[58] M. A. Salem, H. Bağcı, Energy flow characteristics of vector x-waves, Optics express **19**(9), 8526–8532 (2011).

[59] M. Ornigotti, C. Conti, A. Szameit, Universal form of the carrier frequency of scalar and vector paraxial x waves with orbital angular momentum and arbitrary frequency spectrum, Physical Review A **92**(4), 043801 (2015).

[60] M. Diouf, M. Harling, M. Yessenov, L. A. Hall, A. F. Abouraddy, K. C. Toussaint, Space-time vector light sheets, Optics Express **29**(23), 37225–37233 (2021).

[61] M. Yessenov, Z. Chen, M. P. Lavery, A. F. Abouraddy, Vector space-time wave packets, Optics Letters **47**(16), 4131–4134 (2022).

[62] P. Gotovski, S. Orlov, Parabolic vector focus wave modes, Journal of Laser Micro Nanoengineering **14**(1), 25–31 (2019).

[63] V. Vosylius, S. Orlov, Vector focus wave modes with elliptic cross-section, Journal of Laser Micro Nanoengineering **14**(1), 74–80 (2019).

[64] M. Meier, V. Romano, T. Feurer, Material processing with pulsed radially and azimuthally polarized laser radiation, Applied Physics A **86**(3), 329–334 (2007).

[65] M. Kraus, M. A. Ahmed, A. Michalowski, A. Voss, R. Weber, T. Graf, Microdrilling in steel using ultrashort pulsed laser beams with radial and azimuthal polarization, Optics express **18**(21), 22305–22313 (2010).

[66] M. Bhuyan, F. Courvoisier, P. Lacourt, M. Jacquot, R. Salut, L. Furfaro, J. Dudley, High aspect ratio nanochannel machining using single shot femtosecond bessel beams, Applied Physics Letters **97**(8), 081102 (2010).

[67] M. Duocastella, C. B. Arnold, Bessel and annular beams for materials processing, Laser & Photonics Reviews **6**(5), 607–621 (2012).

[68] A. S. Rao, A conceptual review on bessel beams, Physica Scripta **99**(6), 062007 (2024).

[69] J. A. Stratton, *Electromagnetic theory*, volume 33 (John Wiley & Sons, 2007).

[70] J. Durnin, J. Miceli Jr, J. H. Eberly, Diffraction-free beams, Physical review letters **58**(15), 1499 (1987).

[71] Z. Bouchal, J. Wagner, M. Chlup, Self-reconstruction of a distorted nondiffracting beam, Optics communications **151**(4-6), 207–211 (1998).

[72] Z. Bouchal, Nondiffracting optical beams: physical properties, experiments, and applications, Czechoslovak journal of physics **53**(7), 537–578 (2003).

[73] M. A. Bandres, J. C. Gutiérrez-Vega, S. Chávez-Cerda, Parabolic nondiffracting optical wave fields, Optics letters **29**(1), 44–46 (2004).

[74] A. Ashkin, J. M. Dziedzic, J. E. Bjorkholm, S. Chu, Observation of a single-beam gradient force optical trap for dielectric particles, Optics letters **11**(5), 288–290 (1986).

[75] W. Wright, G. Sonek, M. Berns, Radiation trapping forces on microspheres with optical tweezers, Applied Physics Letters **63**(6), 715–717 (1993).

[76] A. T O'Neil, M. J. Padgett, Three-dimensional optical confinement of micron-sized metal particles and the decoupling of the spin and orbital angular momentum within an optical spanner, Optics Communications **185**(1-3), 139–143 (2000).

[77] H. Rubinsztein-Dunlop, T. A. Nieminen, M. E. Friese, N. R. Heckenberg, Optical trapping of absorbing particles, in *Advances in quantum chemistry* (Elsevier, 1998), volume 30, 469–492.

[78] K. Gahagan, G. Swartzlander Jr, Trapping of low-index microparticles in an optical vortex, Journal of the Optical Society of America B **15**(2), 524–534 (1998).

[79] K. Gahagan, G. Swartzlander Jr, Simultaneous trapping of low-index and high-index microparticles observed with an optical-vortex trap, Journal of the Optical Society of America B **16**(4), 533–537 (1999).

[80] J. F. Nye, M. V. Berry, Dislocations in wave trains, Proceedings of the Royal Society of London. A. Mathematical and Physical Sciences **336**(1605), 165–190 (1974).

[81] M. Vasnetsov, K. Staliunas, *Optical Vortices*, Horizons in world physics (Nova Science Publishers, 1999).

[82] K. Volke-Sepulveda, V. Garcés-Chávez, S. Chávez-Cerda, J. Arlt, K. Dholakia, Orbital angular momentum of a high-order bessel light beam, Journal of Optics B: Quantum and Semiclassical Optics **4**(2), S82 (2002).

[83] J. Lekner, Angular momentum of electromagnetic pulses, Journal of Optics A: Pure and Applied Optics **6**(3), S128 (2004).

[84] I. Basistiy, V. Y. Bazhenov, M. Soskin, M. V. Vasnetsov, Optics of light beams with screw dislocations, Optics communications **103**(5-6), 422–428 (1993).

[85] M. Soskin, V. Gorshkov, M. Vasnetsov, J. Malos, N. Heckenberg, Topological charge and angular momentum of light beams carrying optical vortices, Physical Review A **56**(5), 4064 (1997).

[86] G. Molina-Terriza, J. Recolons, L. Torner, The curious arithmetic of optical vortices, Optics letters **25**(16), 1135–1137 (2000).

[87] V. Pyragaite, A. Stabinis, Free-space propagation of overlapping light vortex beams, Optics communications **213**(4-6), 187–191 (2002).

[88] M. V. Berry, M. R. Dennis, Knotted and linked phase singularities in monochromatic waves, Proceedings of the Royal Society of London. Series A: Mathematical, Physical and Engineering Sciences **457**(2013), 2251–2263 (2001).

[89] M. Dennis, Braided nodal lines in wave superpositions, New Journal of Physics **5**(1), 134 (2003).

[90] G. Kontenis, D. Gailevičius, N. Jiménez, K. Staliunas, Optical drills by dynamic high-order bessel beam mixing, Physical Review Applied **17**(3), 034059 (2022).

[91] G. Kontenis, D. Gailevičius, V. Jukna, K. Staliūnas, Terahertz rate rotating helical intensity beams, Optics & Laser Technology **182**, 112036 (2025).

[92] A. Vincotte, L. Bergé, Femtosecond optical vortices in air, Physical review letters **95**(19), 193901 (2005).

[93] F. Flossmann, U. T. Schwarz, M. Maier, M. R. Dennis, Stokes parameters in the unfolding of an optical vortex through a birefringent crystal, Optics Express **14**(23), 11402–11411 (2006).

[94] D. PZ, F. Alhassen, Observation of orbital angular momentum transfer between acoustic and optical vortices in optical fiber, Topologica **1**(1), 015–015 (2008).

[95] C. Lóxpez-Mariscal, J. C. Gutiérrez-Vega, G. Milne, K. Dholakia, Orbital angular momentum transfer in helical mathieu beams, Optics express **14**(9), 4182–4187 (2006).

[96] J. Masajada, A. Popiołek-Masajada, D. M. Wieliczka, The interferometric system using optical vortices as phase markers, Optics Communications **207**(1-6), 85–93 (2002).

[97] A. Ohta, Y. Kawata, Analyses of radiation force and torque on a spherical particle near a substrate illuminated by a focused laguerre–gaussian beam, Optics communications **274**(2), 269–273 (2007).

[98] M. Friese, H. Rubinsztein-Dunlop, J. Gold, P. Hagberg, D. Hanstorp, Optically driven micromachine elements, Applied Physics Letters **78**(4), 547–549 (2001).

[99] L. Paterson, M. P. MacDonald, J. Arlt, W. Sibbett, P. E. Bryant, K. Dholakia, Controlled rotation of optically trapped microscopic particles, Science **292**(5518), 912–914 (2001).

[100] T. Gustavson, A. Chikkatur, A. Leanhardt, A. Görlitz, S. Gupta, D. Pritchard, W. Ketterle, Transport of bose-einstein condensates with optical tweezers, Physical Review Letters **88**(2), 020401 (2001).

[101] J. Arlt, V. Garcés-Chávez, W. Sibbett, K. Dholakia, Optical micromanipulation using a bessel light beam, Optics communications **197**(4-6), 239–245 (2001).

[102] V. Garcés-Chávez, D. McGloin, H. Melville, W. Sibbett, K. Dholakia, Simultaneous micromanipulation in multiple planes using a self-reconstructing light beam, Nature **419**(6903), 145–147 (2002).

[103] K. Dholakia, N. Simpson, M. Padgett, L. Allen, Second-harmonic generation and the orbital angular momentum of light, Physical Review A **54**(5), R3742 (1996).

[104] J. Courtial, K. Dholakia, L. Allen, M. Padgett, Second-harmonic generation and the conservation of orbital angular momentum with high-order laguerre-gaussian modes, Physical Review A **56**(5), 4193 (1997).

[105] A. Berzanskis, A. Matijosius, A. Piskarskas, V. Smilgevicius, A. Stabinis, Conversion of topological charge of optical vortices in a parametric frequency converter, Optics communications **140**(4-6), 273–276 (1997).

[106] A. Beržanskis, A. Matijošius, A. Piskarskas, V. Smilgevičius, A. Stabinis, Sum-frequency mixing of optical vortices in nonlinear crystals, Optics communications **150**(1-6), 372–380 (1998).

[107] G. Molina-Terriza, L. Torner, D. V. Petrov, Vortex streets in walking parametric wave mixing, Optics letters **24**(13), 899–901 (1999).

[108] F. Devaux, R. Passier, Phase sensitive parametric amplification of optical vortex beams, The European Physical Journal D **42**, 133–137 (2007).

[109] L. Torner, D. V. Petrov, Splitting of light beams with spiral phase dislocations into solitons in bulk quadratic nonlinear media, JOSA B **14**(8), 2017–2023 (1997).

[110] D. V. Petrov, L. Torner, J. Martorell, R. Vilaseca, J. P. Torres, C. Cojocaru, Observation of azimuthal modulational instability and formation of patterns of optical solitons in a quadratic nonlinear crystal, Optics letters **23**(18), 1444–1446 (1998).

[111] L. T. Vuong, T. D. Grow, A. Ishaaya, A. L. Gaeta, G. W. 't Hooft, E. R. Eliel, G. Fibich, Collapse of optical vortices, Physical review letters **96**(13), 133901 (2006).

[112] D. V. Petrov, G. Molina-Terriza, L. Torner, Vortex evolution in parametric wave mixing, Optics communications **162**(4-6), 357–366 (1999).

[113] G. Molina-Terriza, L. Torner, Multicharged vortex evolution in seeded second-harmonic generation, JOSA B **17**(7), 1197–1204 (2000).

[114] V. Jarutis, A. Matijošius, V. Smilgevičius, A. Stabinis, Second harmonic generation of higher-order bessel beams, Optics communications **185**(1-3), 159–169 (2000).

[115] J. Arlt, K. Dholakia, L. Allen, M. Padgett, Parametric down-conversion for light beams possessing orbital angular momentum, Physical Review A **59**(5), 3950 (1999).

[116] P. Di Trapani, A. Beržanskis, S. Minardi, S. Sapone, W. Chinaglia, Observation of optical vortices and j 0 bessel-like beams in

quantum-noise parametric amplification, Physical review letters **81**(23), 5133 (1998).

[117] K. Staliunas, Three-dimensional turing structures and spatial solitons in optical parametric oscillators, Physical review letters **81**(1), 81 (1998).

[118] K. Staliunas, V. J. Sanchez-Morcillo, *Transverse patterns in nonlinear optical resonators*, volume 183 (Springer Science & Business Media, 2003).

[119] P. Saari, K. Reivelt, Evidence of x-shaped propagation-invariant localized light waves, Physical Review Letters **79**(21), 4135 (1997).

[120] W. Erikson, S. Singh, Polarization properties of maxwell-gaussian laser beams, Physical Review E **49**(6), 5778 (1994).

[121] Optical constants of bk7, https://refractiveindex.info/?shelf=glass&book=BK7&page=SCHOTT, accessed: 2024-02-01.

[122] H. Li, J. Liu, L. Bai, Z. Wu, Deformations of circularly polarized bessel vortex beam reflected and transmitted by a uniaxial anisotropic slab, Applied Optics **57**(25), 7353–7362 (2018).

[123] S. Fu, C. Gao, *Vector Beams and Vectorial Vortex Beams* (Springer Nature Singapore, Singapore, 2023), 277–333.

[124] S. Orlov, K. Regelskis, V. Smilgevičius, A. Stabinis, Propagation of bessel beams carrying optical vortices, Optics communications **209**(1-3), 155–165 (2002).

[125] S. Orlov, C. Huber, P. Marchenko, P. Banzer, G. Leuchs, Toward a corrected knife-edge-based reconstruction of tightly focused higher order beams, Frontiers in Physics **8**, 527734 (2020).

[126] D. N. Nikogosyan, *Properties of optical and laser-related materials: a handbook* (2003).

[127] M. A. Porras, A. Parola, P. Di Trapani, Nonlinear unbalanced o waves: nonsolitary, conical light bullets in nonlinear dissipative media, JOSA B **22**(7), 1406–1413 (2005).

[128] A. P. Stabinis, G. Valiulis, Ultratrumpųjų šviesos impulsų netiesinė optika, Vilniaus universitetas (2008).

[129] K. Laurinavičius, S. Orlov, Localized vector optical nondiffracting subcycle pulses, Applied Sciences **14**(24), 11538 (2024).

[130] R. M. Arkhipov, M. V. Arkhipov, A. V. Pakhomov, P. A. Obraztsov, N. N. Rosanov, Unipolar and subcycle extremely short pulses: recent results and prospects (brief review), JETP Letters **117**(1), 8–23 (2023).

[131] P. Saari, O. Rebane, I. Besieris, Energy-flow velocities of nondiffracting localized waves, Physical Review A **100**(1), 013849 (2019).

[132] H. Liang, P. Krogen, Z. Wang, H. Park, T. Kroh, K. Zawilski, P. Schunemann, J. Moses, L. F. DiMauro, F. X. Kärtner, et al., High-energy mid-infrared sub-cycle pulse synthesis from a parametric amplifier, Nature Communications **8**(1), 141 (2017).

[133] Z. Wu, X. Zeng, Z. Li, Z. Zhang, X. Wang, X. Wang, J. Mu, Y. Zuo, J. Su, H. Peng, et al., Generation of subcycle isolated attosecond pulses by pumping ionizing gating, Physical Review Research **6**(1), 013126 (2024).

[134] T. Fuji, Y. Nomura, Generation of phase-stable sub-cycle mid-infrared pulses from filamentation in nitrogen, Applied Sciences **3**(1), 122–138 (2013).

[135] J. Ouyang, S. Ding, Z.-J. Zhu, Q.-L. Zhang, X. Han, Q.-S. Jia, Transmission metasurface for x-wave generation, in *2024 IEEE International Symposium on Antennas and Propagation and INC/USNC-URSI Radio Science Meeting (AP-S/INC-USNC-URSI)* (IEEE, 2024), 1805–1806.

CURRICULUM VITAE

Name:	Klemensas
Surname:	Laurinavičius
Place of birth:	Klaipėda, Lithuania

Education:

2020 – 2024	Center for Physical Sciences and Technology
	Ph.D. studies.
2018 – 2020	Vilnius University, Faculty of Physics
	Master's degree in Technology.
2014 – 2018	Vilnius University, Faculty of Physics
	Bachelor's degree in Physics.

Work experience:

2024-01 – now	Center for Physical Sciences and Technology
	Junior Research Scientist.
2022-08 – 2024-01	Center for Physical Sciences and Technology
	Senior Engineer.
2020-08 – 2022-08	Center for Physical Sciences and Technology
	Engineer.
2018-08 – 2020-08	Center for Physical Sciences and Technology
	Technician.

TRUMPOS ŽINIOS APIE AUTORIŲ

Vardas:	Klemensas
Pavardė:	Laurinavičius
Gimimo vieta:	Klaipėda, Lietuva

Išsilavinimas:

2020 – 2024	Fizinių ir technologijos mokslų centras
	Doktorantūros studijos.
2018 – 2020	Vilniaus universitetas, Fizikos fakultetas
	Technologijų magistro laipsnis.
2014 – 2018	Vilniaus universitetas, Fizikos fakultetas
	Fizikos bakalauro laipsnis.

Profesinė veikla:

2024-01 – dabar	Fizinių ir technologijos mokslų centras
	Jaunesnysis mokslo darbuotojas.
2022-08 – 2024-01	Fizinių ir technologijos mokslų centras
	Vyresnysis inžinierius.
2020-08 – 2022-08	Fizinių ir technologijos mokslų centras
	Inžinierius.
2018-08 – 2020-08	Fizinių ir technologijos mokslų centras
	Technikas.

NOTES

NOTES

Vilniaus universiteto leidykla
Saulėtekio al. 9, III rūmai, LT-10222 Vilnius
El. p. info@leidykla.vu.lt, www.leidykla.vu.lt
bookshop.vu.lt, journals.vu.lt
Tiražas 20 egz.